The Dissertation Committee for Vimal Singh
certifies that this is the approved version of the following dissertation:

Fast Dynamic Magnetic Resonance Imaging using Sparse Recovery Methods and Novel Signal Encoding Formulations

Committee:

Ahmed H. Tewfik, Supervisor

Alan C. Bovik

David B. Ress

Joydeep Ghosh

Mia K. Markey

Sujay Sanghavi

Fast Dynamic Magnetic Resonance Imaging using Sparse Recovery Methods and Novel Signal Encoding Formulations

by

Vimal Singh, B.Tech; M.S.E.E

DISSERTATION

Presented to the Faculty of the Graduate School of

The University of Texas at Austin

in Partial Fulfillment

of the Requirements

for the Degree of

DOCTOR OF PHILOSOPHY

THE UNIVERSITY OF TEXAS AT AUSTIN

December 2015

Dedicated to my family.

Acknowledgments

This dissertation would not have been possible without the help and support from a large number of people. Though I cant list all of them, I would like to express my thanks to everyone who helped me get to this point I am indebted to you all for the inspiration you have given me.

I am grateful to my adviser, Professor Ahmed H. Tewfik, for his support and guidance throughout my graduate studies, and for providing me with so many opportunities for scientific, professional, and personal growth. I will always be grateful for his never-ending confidence in my abilities to trek through difficult periods in my PhD. Lastly, I shall always strive to develop realizable solutions for current real-world problems, a philosophy he has constantly emphasized on.

I am also grateful to Professor David Ress for inducting me in the practical world of MRI. For taking a chance on an over-excited graduate student who ended up taking longer than expected to learn about MR sequence programming. I thank him for hosting me at Baylor College of Medicine in Houston, and invaluable lessons in MR physics, functional MRI and the field of Neuroscience.

I would also like to thank the other members of my doctoral committee Professors Alan C. Bovik, Joydeep Ghosh, Mia Markey and Sujay Sanghavi

for their time, effort, and help, and for their influence on my training and research.

I am also very appreciative of the various other friends and collaborators I have had the privilege to interact with at the University of Texas at Austin, Baylor College of Medicine and University of Minnesota. I would like to mention my mates from various labs: Dr. Vikhram Gowreesunker, Dr. Nikhil Kundargi, Dr. Dan Wang, Dr. Vijay Aditya Tadipatri, Dr. Yingxi Liu, (soon to be Dr.) Youngchun Kim, Dr. Jung Hwan Kim, Neeraj Gaur, Andrew Floren and, Elizabeth Halfen. I would like to thank them for their valuable time they catered to my research work in form of stimulating discussions, reviewing documents, being subjects in fMRI studies and most importantly for making the long hours in lab seem shorter.

I am grateful to my parents and siblings for their unfailing love, support, and patience, and for all the sacrifices they made so that I could have more. Finally, I would like to thank my wife, Dr. Ashima Singh, for her unconditional love and support during the last leg of my PhD journey. Her motivation, patience and sacrifices gave me strength to finish this PhD.

Fast Dynamic Magnetic Resonance Imaging using Sparse Recovery Methods and Novel Signal Encoding Formulations

Publication No. _____

Vimal Singh, Ph.D.
The University of Texas at Austin, 2015

Supervisor: Ahmed H. Tewfik

Magnetic resonance imaging (MRI) is a non-invasive imaging modality that provides excellent soft tissue contrast without using ionizing radiations. These qualities/properties make MRI the preferred imaging modality for critical organs like heart and brain. Over the past decade, the advancement in hardware and image reconstruction algorithms has led to substantial improvements in MRI in terms of imaging speeds, quality and reliability. However, MRI speeds need to be further improved while retaining/maintaining the image quality given that the emerging medical diagnostic procedures are increasingly relying on detailed characterization of physiological functions that evolve on time scales too fast to be captured using conventional MRI methods.

This dissertation starts with presenting a sparse signal recovery based fast MRI method. This method synergistically combines a data redundancy

scheme for high frequency details with a novel and physically realizable MR signal encoding formulation. The new signal encoding formulation uses clinically deployed tagging radio frequency pulses to mix information in the spatial frequency domain prior to acquisition. Thus, the new formulation leads to a more uniform coverage of spatial frequency information even at high accelerations. The synergistic combination of image-detail redundancy encoding with tagging based signal encoding allows recovery of edges and fine structures with unprecedented quality.

Next, this dissertation evaluates the use of fast spiral trajectories for high spatial resolution functional imaging of human superior colliculus. Gradient efficient and motion-robust spiral trajectories are used to keep fMRI scan durations short. . However, high resolution imaging of human subcortical structures using these trajectories is limited due to the weak functional responses of SC structures and also low signal-to-noise ratio associated with small voxels. To improve the functional sensitivity of spiral trajectories, dual echo variants are used. Combination of two echoes of the dual-echo variants reduces noise and thereby improves the functional sensitivity of high resolution fMRI.

Lastly, this dissertation presents a novel formulation for fast dynamic MRI which combines the generic linear dynamical system model with sparse recovery techniques. Specifically, the formulation uses a known prior spatio-temporal model to predict the underlying image and uses sparse recovery techniques to recover the residual image. The spatio-temporal evolution model

inherently encodes for coupled data redundancies in the spatial- and temporal-dimensions. Also, the generalizability of the formulation in choosing the evolution model allows it to be applicable to various physiological functions.

Table of Contents

List of Tables

List of Figures

Chapter 1

Introduction

1.1 Motivation

The non-ionizing property of Magnetic Resonance Imaging (MRI) makes it the preferred choice of modality for imaging organs such as brain, heart and muscles [135]. MRI offers a variety of contrast mechanisms allowing excellent visualization of both anatomical structures and physiological functions [97]. In addition, the ability of MR imaging to tune the contrast to an underlying tissue of interest makes it a versatile diagnostic and scientific-research tool. However, due to physical and physiological constraints, the data acquisition in MRI is sequential in time which makes MRI a slow imaging modality. Like MRI, Computed tomography (CT) and positron emission tomography (PET) are sequential imaging modalities with limited acquisition speeds. Ultrasound by comparison, is relatively a fast imaging modality. Regardless of speed, however, CT, PET and ultrasound cannot deliver the contrast versatility, high SNRs and spatial resolution as MRI. For MRI, the sequential acquisition process leads to a three-way trade-off between: 1) the acquisition time, 2) the signal-to-noise-ratio (SNR) and, 3) the spatial resolution [84, 99, 135]. This trade-off limits the application of MRI in several diagnostic scenarios, such as: myocardial perfusion for ischemia detection [64, 65], brain perfusion for tumor

detection [5] and, functional brain imaging (fMRI studies) for systemic brain disease or psychiatric disorder detection [121]. Operating within the trade-off triangle for functional imaging leads to either sub-diagnostic quality images or long scan durations. Mitigating these limitations would bring the advantages of MRI to myocardial and cerebral perfusion studies and brain fMRI, and in particular help us improve the sensitivity and specificity of the diagnosis through high temporal and spatial imaging resolutions.

Dynamic MRI applications such as perfusion studies and functional brain MRI (fMRI) require high spatial and temporal resolutions to characterize the underlying physiological process accurately both in space and time. First-pass myocardial perfusion MRI detects and evaluates ischemic heart disease [64, 65]. Fast MR imaging (MRI) during the first pass of an injected contrast agent is required to assess myocardial perfusion to detect any regional impairments of myocardial blood flow that may lead to ischemia [64, 65]. Myocardial perfusion measures the micro-circulation in tissue and requires high spatial and temporal resolutions to perform assessments at the requisite high information rates [65]. Similarly, functional MRI studies aimed at resolving signals within the neocortical laminae require sub-millimeter spatial resolutions to further understand the computational processing of the brain [37, 38, 110]. In another brain region of interest, high spatial resolution is critical to resolve the topographic representations of sensory processing within the laminae of the superior colliculus, a laminar structure with three mm-scale regions in depth. The superficial layers receive direct retinal inputs, intermediate layers

are associated with visual attention and oculomotor responses, and deep layers play a role in multi-sensory integration. In addition, faster acquisitions of neural activation are needed to characterize their faster hemodynamic responses as compared to cortical gray matter [37]. Thus, with emerging medical and research applications, the challenge in MR imaging is to reduce image acquisition times while maintaining high spatial resolutions and good SNRs. This thesis is focused on novel techniques for increasing MR imaging speed in myocardial perfusion studies and brain fMRI, while maintaining fine spatial resolutions and satisfactory SNR . The proposed techniques are generalizable and can be easily extended to other dynamic applications, in process reducing the scan durations and the cost of clinical MRI.

Previously, many techniques have exploited the raw data redundancy in the spatial and/or temporal dimensions to reduce the acquisition time for dynamic MRI [91, 124]. These techniques show limited performance improvements at low accelerations (≤ 2). In recent years, many fast MRI techniques based on the theory of Compressed Sensing (CS) [30, 87, 88] have emerged. CS based MRI methods rely on recovering the sparse representation of the underlying image in a sparsifying basis that exhibits high incoherency with the sensing basis using non-linear algorithms. CS-MRI methods recover images with good SNRs at low acceleration factors (< 4); however, they produce sub-diagnostic quality images at higher acceleration factors (≥ 4). Alternative techniques rely on some form of data sharing. For example, the highly constrained back-projection (HYPR) [42, 94, 95] and the k-t focal under-

determined system solver (k-t FOCUSS) [66, 140] techniques proposed for fast dynamic MR applications rely on under-sampling high frequency components in an image time-series under the assumption that high frequency details do not change over time. Both HYPR and the k-t FOCUSS techniques show limited performance improvements for myocardial perfusion imaging and fMRI acquisitions, respectively.

1.2 Contributions

In this thesis, fast MRI techniques based on sparse recovery techniques and modifications to the underlying MR signal encoding are proposed.

1. For my first contribution, I propose a fast MRI method that uses dictionary learning for sparse representation of image-patches for redundancy encoding and a novel MR signal encoding formulation which uses spatial modulations with radio frequency (RF) pulses for raw data acquisition. The modulation of spatial amplitudes in the proposed signal encoding formulation leads to acquisition of data samples that are mixtures of the standard k-space samples. Thus, the new formulation leads to a more uniform coverage of k-space information even at high accelerations. The true innovation of the proposed fast MRI method is the synergistic combination of image-details based redundancy encoding with the tagging-based MR signal encoding formulation. The power of the method is demonstrated using various experiments on in-vivo MRI data sets for both static and dynamic applications.

2. For my second contribution, I propose to develop, tune and evaluate dual-echo spiral variants for high-resolution functional imaging in human superior colliculus (SC). The magnetic resonance imaging data for subcortical structures (like SC) in human cranium exhibits low SNR and low functional CNR due to their deep location and weak functional response to strong stimuli. To overcome these challenges, I evaluate the use of dual-echo spiral variants that combine outward and inward trajectories. Acquisition of two echoes using dual-echo variants should increase the available contrast as well as reduce noise. Specifically, in-in, in-out, and out-out combinations are evaluated. For completeness, single-echo spiral in and a parallel-receive accelerated EPI sequence are also evaluated. All sequences are compared relative to a single-echo spiral-out trajectory to establish a within-session reference. Sequence evaluation is based on comparison of functional contrast-to-noise ratio within retinotopically predefined regions-of-interest. The sequences were also compared in early visual cortex.

3. For my third contribution, I propose a novel formulation for fast dynamic MRI which combines the generic linear dynamical system model with sparse-recovery methods. Specifically, the formulation uses a known prior time-evolution model for the physiological function implicitly and enforces the model errors (innovations) to be sparse. This time-evolution model inherently encodes for data redundancies in both spatial- and temporal-dimension as opposed to techniques account for them explicitly.

Use of the prior model results in highly compressible innovation signals that are recovered with high fidelity even from strongly under-sampled data. Various experiments for both Cartesian and radial under-sampling experiments on in-vivo myocardial perfusion data demonstrate the improved performance of the proposed formulation over that of k-space data-sharing and sparse-recovery techniques individually.

1.3 Thesis Overview

This dissertation is organized as follows: The following chapter (Chapter 2) presents a short introduction of magnetic resonance imaging, the compressed sensing theory and the linear dynamical system model. Section 2.1 contains a high-level overview of MR physics, signal generation, spatial encoding and image reconstruction for Cartesian and non-Cartesian acquisitions. Section 2.2 reviews the general compressed sensing theory followed by its applications in MRI. Section 2.3 briefly reviews the linear dynamical system and the Kalman filter. In the final section 2.4 a short literature review of methods used for increasing MRI speeds is presented.

Chapter 3 presents the radio-frequency tagging pulses based MR signal encoding formulation. A brief review of tagging pulses followed by the complete mathematical treatment of the proposed signal encoding formulation is presented in section 3.2. Section 3.3 details the redundancy encoding for high-frequency details in MR images through dictionary learning techniques. Finally, section 3.4 presents the validation of the proposed fast MRI technique

through experiments on various static and dynamic in-vivo data sets.

Chapter 4 describes the development and evaluation of dual echo spiral variants for high resolution functional imaging of human superior colliculus and early visual cortex. Section 4.2 is focused on the implementation details of Archimedean spiral trajectories and the dual echo sequence development. Section 4.3 describes the MRI methods used to acquire functional data for different sequence variants on healthy human volunteers. This section also details the methods used to analyze the functional data. Finally, section 4.4 presents the results followed with discussion in section 4.5.

Chapter 5 details the linear dynamical system based fast dynamic MRI formulation. A short literature review of previous techniques used for improving speeds in dynamic MRI is also presented. Section 5.2 presents the mathematical treatment of the proposed LDS formulation, the sparse recovery problem and its solution. Results on an in-vivo myocardial data set using the proposed technique and its comparison with previous techniques is presented in section 5.3

Finally, in Chapter 6 I summarize the contributions of my work for increasing imaging speeds in static and dynamic MRI applications.

Chapter 2

Background

2.1 Magnetic Resonance Imaging

Magnetic resonance imaging is based on the Nuclear Magnetic Resonance (NMR) phenomenon which has a quantum mechanical nature. However, at the macroscopic scale, i.e., at the scale of MR image voxel size (∼mm) the NMR phenomenon can be accurately described using classical physics [14, 84, 99]. A short review of MRI signal generation is presented in sec. 2.1.1. Signal encoding techniques are summarized in sec. 2.1.2. Finally, section 2.1.3 details the reconstruction of images from the MRI signal.

2.1.1 Nuclear Magnetic Resonance

The phenomenon of nuclear magnetic resonance arises in the nuclei of atoms with an odd number of nucleons. These nuclei possess spin angular momentum, which is observed in various biologically-important atomic nuclei (^{1}H, ^{3}1P, ^{2}3Na), however because ^{1}H is the most abundant in the body, most human imaging is based on the proton NMR signal. Atomic nuclei with non-zero spin angular momentum generate a magnetic field that is characterized by a magnetic dipole moment $\mu = \mu_x\hat{i} + \mu_y\hat{j} + \mu_z\hat{k}$, where $\hat{i}$, $\hat{j}$ and $\hat{k}$ are the units vectors in the Cartesian coordinate system.

The total magnetization moment within a volume is the vector sum of all individual magnetic dipole moments. i.e., $M = \sum_{i \in vol} \mu_i$ where, μ_i is the magnetic moment for the i$^{\text{th}}$ nucleus. In absence of an external magnetic field, at thermal equilibrium the dipole moments are randomly oriented resulting in net magnetization $M = 0$. However, under a strong external static magnetic field B_0, a small fraction of the magnetic moments (μ_i) align themselves in the direction of the field to yield a non-zero magnetization moment M. The fraction of nuclei that align with the field is tiny, e.g., 37 ppm at 3T field strength, because the energy of the spin transition is correspondingly small compared to the background thermal energy of the tissue. In NMR, it is this net magnetic moment (or simply magnetization) that is manipulated to produce a measurable signal. The B_0 field direction, which is generally taken to be the z-axis and its perpendicular plane (x, y) are often referred to as the longitudinal direction and the transverse plane.

The interaction of the magnetization M with an external magnetic field B is governed by the **Bloch equation**,

$$\frac{dM}{dt} = M \times \gamma B + \frac{M_0 - M_z}{T_1} + \frac{M_{xy}}{T_2} \tag{2.1}$$

where, M_0 is the equilibrium magnetization corresponding to the static component of the field B, M_z and M_{xy} are the longitudinal and transverse component of M, T_1 and T_2 are constants and are specific to different types of tissues and, γ is the gyromagnetic ratio which is a known constant unique for different nuclear species. For a static magnetic field $[B(t) = B_0]$ the magnetization will

fluctuate around its equilibrium value (M_0). To create a detectable signal, a circularly polarized radio frequency (RF) field $B1(t)$ is applied in addition to the static field resulting in a time-varying magnetic field $B(t) = B_0 + B1(t)$. The RF field tips the net magnetization away from the longitudinal direction producing a transverse magnetization component M_{xy}. The tipped magnetization precesses at a characteristic frequency

$$f_0 = \frac{\gamma}{2\pi} B_0 \tag{2.2}$$

where, f_0 denotes the precession frequency, B_0 the static field strength, and $\frac{\gamma}{2\pi}$ is a constant (42.57 MHz/T). This frequency is an important quantity known as the *Larmor Frequency*. The magnetization is resonant at that well-defined frequency. Siemens 3T clinical MR systems have a frequency of f_0=124 MHz. It is the transverse component of the precessing magnetization that produces a signal detectable by receiver coils.

In MRI, the application of the RF field $B1(t)$ is termed as *excitation*, and is a short lived process. After excitation, the time evolution of the net magnetization is described by the Bloch equation (eqn. (2.1)). The solution to Bloch equation for a magnetization $M(t)$ with initial value $M(0) = M_x(0)\hat{i} + M_y(0)\hat{j} + M_z(0)\hat{k}$ in presence of a field $B = B_z\hat{k}$ is

$$M_{xy}(t) = M_{xy}(0)e^{-i\gamma B_z t}e^{-t/T_2} \tag{2.3a}$$

$$M_z(t) = M_z(0)e^{-t/T_1} + M_0(1 - e^{-t/T_1}) \tag{2.3b}$$

where, we use the complex phasor notation $M_{xy}(t) = M_x(t) + iM_y(t)$, and it is assumed that $B_z = B_0 + \triangle B$, with $\triangle B \ll B_0$ such that at thermal

equilibrium the magnetization M_0 is not significantly perturbed. After excitation the transverse magnetization experiences exponential decay with a time constant T_2^* (eqn. (2.3a)) and the longitudinal component experiences exponential recovery with a time constant T_1 (eqn. (2.3b)). The apparent transverse relaxation time corresponds to the sum of two dephasing processes,

$$T_2^* = \frac{1}{\frac{1}{T_2} + \frac{1}{T_2'}} \tag{2.4}$$

where T_2 is associated with spin-spin dephasing interactions, and T_2' is associated with dephasing relatively static field in homogeneities. The relaxation parameters (T_1, T_2^*, and T_2) are one of the most important image contrast mechanisms as different types of tissues have different relaxation parameters.

The time-varying transverse magnetization $M_{xy}(t)$ results in magnetic flux changes in the receiver coils that generate an electromotive force in the coil. Therefore, the received signal $s_r(t)$ is derived from the contributions of all the precessing transverse magnetization in the volume. Simplistically, the received signal is

$$s_r(t) = \oint_{r \in vol.} M_{xy}(r,t) e^{-t/T_2(r)} e^{(-i\gamma \triangle Bt)} e^{(-i2\pi f_0 t)} dr \tag{2.5}$$

where, $r = (x, y, z)$ corresponds to coordinate tuple inside the volume of interest.

There are several RF coil geometries that are used in current MRI systems. They include solenoidal coils, which are used when the B_0 field is perpendicular to the body axis. Birdcage coils are used when B_0 field axis is

parallel to the body axis. Surface coils are localized coils that are coupled to a limited region of the body. Surface coils are appropriate for imaging superficial structures. Compared to using a head or body birdcage coil as the receiver coil, surface coils achieve a better SNR in superficial regions because of higher image-volume to noise-volume ratio. In contrast, surface coils are associated with highly non-uniform transmit B1 distribution. Conventionally, a single coil is used for both the RF excitation and signal reception. However, separate coils maybe used for transmit and receive portions. A critical requirement for good SNR in MRI is to achieve a uniform RF excitation. Thus, it is desirable to achieve uniform excitation with a head or body coil but to receive signal from a localized region using a surface coil for better SNR. While a single surface coil provides higher SNR in a localized region, surface coil arrays are commonly used because they extend the available field-of-view while retaining the higher advantages. Coil arrays are also useful for scan acceleration.

2.1.2 Spatial Encoding and *k*-Space

The signal $s_r(t)$ in eqn. (2.5) is volume-accumulated and lacks spatial position information for smaller imaging units, i.e., voxels. To encode the spatial information various mechanisms are available [14, 72, 84, 99], the most common forms involve designing $\triangle B$ in eqn. (2.5) to have spatial and temporal variations. In addition to the static field B_0 and the RF field $B_1(t)$, three gradient fields, $G_x(t)$, $G_y(t)$ and $G_z(t)$ are used to create linear variations in the longitudinal magnetic field strength as a function of spatial position. Note,

all these gradient fields are in the longitudinal direction, i.e., $\hat{k}$, however their strength varies and the direction of the variation in field strength is along the designated axis. For example, when G_x is applied, the magnetic field will vary with position

$$B(x, y, z) = (B_0 + G_x x)\hat{k} \tag{2.6}$$

As a result, the precession frequency of the magnetization will vary in proportion to the gradient field, i.e., in eqn. (2.6), for $G_x > 0$, protons will precess slowly at $x < 0$ than at $x > 0$. This variation is used to resolve the spatial distribution.

Spatial encoding through the use of linear gradient fields during data acquisition, as in Lauterbur's original experiment [81], has become the most widely-used spatial encoding mechanism in MRI, and has a very convenient Fourier-domain interpretation [77, 126]. To see this Fourier relation more concretely consider the following: the gradient-induced variation in precession frequency causes a location dependent phase dispersion to develop. The additional frequency contributed by gradient fields can be written as

$$f(r) = \frac{\gamma}{2\pi} \vec{G(t)}.\vec{r} \tag{2.7}$$

where $\vec{G(t)}$ is a vector of the gradient fields amplitudes. The phase of magnetization is the integral of frequency starting from time zero (immediately following the RF excitation):

$$\phi(r, t) = 2\pi \int_0^t \frac{\gamma}{2\pi} \vec{G(\tau)}.\vec{r} d\tau \tag{2.8a}$$

$$= 2\pi r.k(t) \tag{2.8b}$$

where,

$$k(t) = \frac{\gamma}{2\pi} \int_0^t G(\tau) d\tau \tag{2.9}$$

Substituting eqn. (2.9) in eqn. (2.5), the acquired MRI signal can be rewritten as

$$s_r(t) = \oint_r \rho(r) e^{(-i2\pi r.k(t))} dr \tag{2.10}$$

where, $\rho(r) = M_{xy}(r,t) \times e^{-t/T_2^*}$ is the desired relaxation-weighted images and $e^{(-i2\pi f_0 t)}$ has been omitted for the baseband signal demodulation. The eqn. 2.10 matches the Fourier-transform relationship between the desired image $\rho(r)$ and observed signal $s_r(t)$. Alternatively, the received signal $s_r(t)$ at time t is the Fourier transform of the object $\rho(r)$ sampled at the spatial frequency $k(t)$. This spatial-frequency transform domain is commonly known as the k-space in the MRI community [86, 126].

2.1.3 Pulse Sequences and Imaging

The design of an MRI acquisition method centers on developing the gradient waveforms $G(t)$ that drive the MR system. These waveforms, along with the associated RF pulses used to produce the magnetization, are called a *pulse sequence*. The integral of the $G(t)$ waveforms traces out a trajectory $k(t)$ in k-space. In principle, a complete MR image can be reconstructed from a single acquisition by using a k-space trajectory that covers the region of k-space determined by the desired spatial resolution [8]. This is commonly done in applications such as imaging brain activation. However, for most applications this results in inadequate temporal resolution and excessive image artifacts.

Figure 2.1 shows the pulse sequence diagram for the Gradient Recalled Echo (GRE) sequence. The three gradient waveforms, the RF pulse and the ADC output are shown. For demonstration purposes a sample k-space and the corresponding Nyquist sampled image are also shown.

Due to physical and physiological constraints the usable maximum gradient strength and slew rate (rate-of-change) are limited. High gradient amplitudes and rapid switching produces peripheral nerve stimulation in patients [23]. Also from the perspective of signal-to-noise ratio, high gradients require large acquisition bandwidth of the desired signal, leading to increased measurement noise. Thus, k-space trajectories are traversed smoothly and relatively slowly compared to the maximum limits of gradient system. In addition, the exponential magnetization decay limits the number of k-space samples that can be acquired after every excitation. As a result, most MRI imaging methods use multiple repetitions of RF excitation and spatial encoding; each one samples a part of k-space. The data from the multiple repetitions is then used to reconstruct an image. The relatively time-consuming nature of this procedure is one of the primary limitations of MRI.

Although, there are physical and physiological limitations to how fast the k-space can be traversed, there is considerable freedom in designing the path a k-space trajectory traverses for each acquisition. Figure 2.2 shows some of the commonly used 2D and 3D k-space trajectories. Cartesian or 2DFT acquisition uses straight lines from a Cartesian grid and is used widely in both clinical imaging and research application. However, many other trajectories

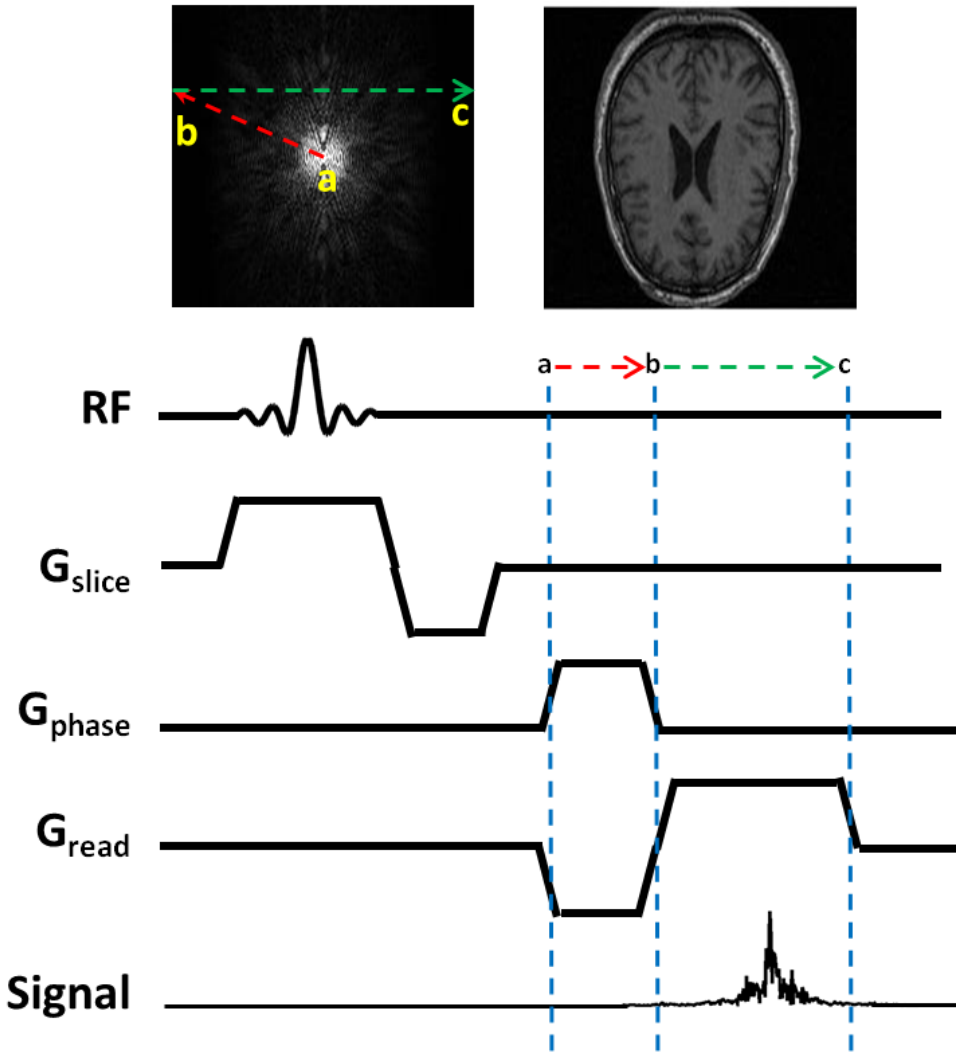

Figure 2.1: A typical two-dimensional gradient-echo pulse sequence. Shown are lines representing activity of the radiofrequency field (RF) and the three spatial gradients. The pulse sequence begins with a combined slice selection gradient G_{slice} and excitation pulse, followed by rephrase lobe to correct spin phase along the slice direction. The G_{phase} gradient is used for selecting one line of k-space following each excitation pulse, while the G_{read} gradient is turned on during signal acquisition. This sequence is known as a gradient-echo sequence, and it acquires each line of k-space following a separate excitation. Following n excitations, all of k-space is filled and image acquisition is complete.

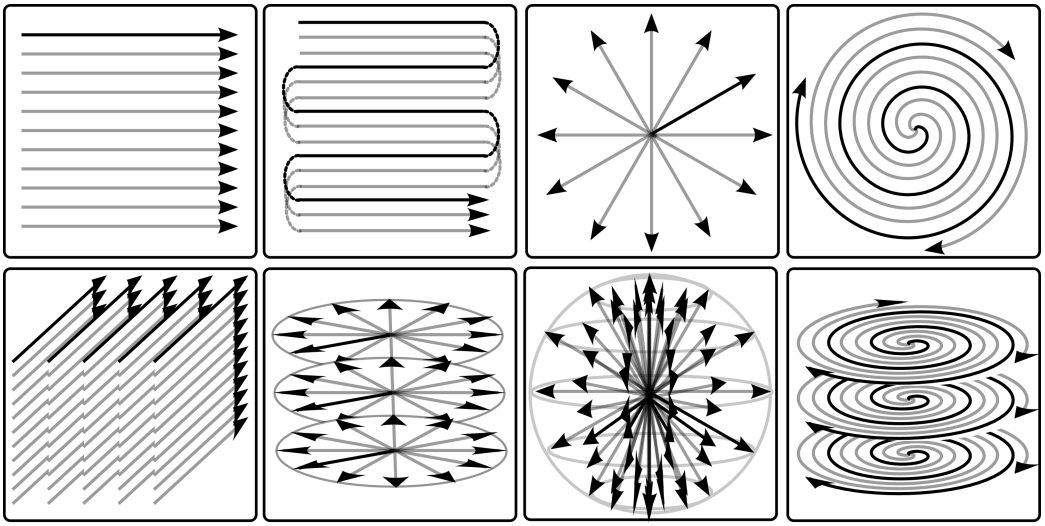

Figure 2.2: Common sampling trajectories. Top, left to right: Cartesian 2D, Cartesian echo-planar, radial, spiral. Bottom left to right: Cartesian 3D, stack of radial, 3D radial, 3D stack of spirals. Figure originally appeared in [89]

such as radial, echo-planar-imaging and spiral are also used. Radial acquisitions are less susceptible to motion artifacts than Cartesian trajectories [49], and can be significantly under-sampled without unsatisfactory artifacts [116], especially for high contrast objects [6, 104]. Spirals make efficient use of the gradient system hardware, are robust to motion artifacts, and are used in real-time and rapid imaging applications [93]. All of these geometries can be used for both 2D and 3D k-space acquisitions.

Cartesian trajectories allow for fast and efficient image reconstruction from the acquired k-space data. The reconstruction can be performed with a simple inverse fast Fourier transform (FFT). In comparison, the reconstruction from non-Cartesian data is more complicated. In general, the reconstruction involves resampling the k-space data to a Cartesian grid followed by the FFT

[62] operation. There are two common approaches to resampling the data. The first approach is based on "grid driven" interpolation, where the value at each grid point is interpolated from the neighboring k-space data. The second is the "data driven" interpolation where the contribution from each sampled data point is added to the adjacent grid points, this approach is commonly known as "gridding reconstruction". Also, for the radial acquisition and specially designed spiral trajectories, the filtered back-projection technique can be used [93].

The size and density for each k-space trajectory is based on the number of samples required to meet the Nyquist criterion. The Nyquist criterion is in turn dependent on the imaging field-of-view and the desired resolution. Image field-of-view determines the density of the k-space samples: the sampling density must increase with the size of the object being imaged. Image resolution is dependent on the highest spatial frequency acquired: the size of acquired k-space region must increase with spatial resolution. A violation of the Nyquist criterion results in under-sampling artifacts. Figure 2.3 shows few examples of under-sampling for the Cartesian acquisitions.

2.2 Compressed Sensing

The field of Compressed Sensing (CS) grew out of the work of Candes, Romberg, and Tao and of Donoho, who showed that a finite-dimensional signal with a sparse or compressible representation can be recovered from a small set of linear, non-adaptive measurements [15–17, 19, 30, 31]. A sparse signal

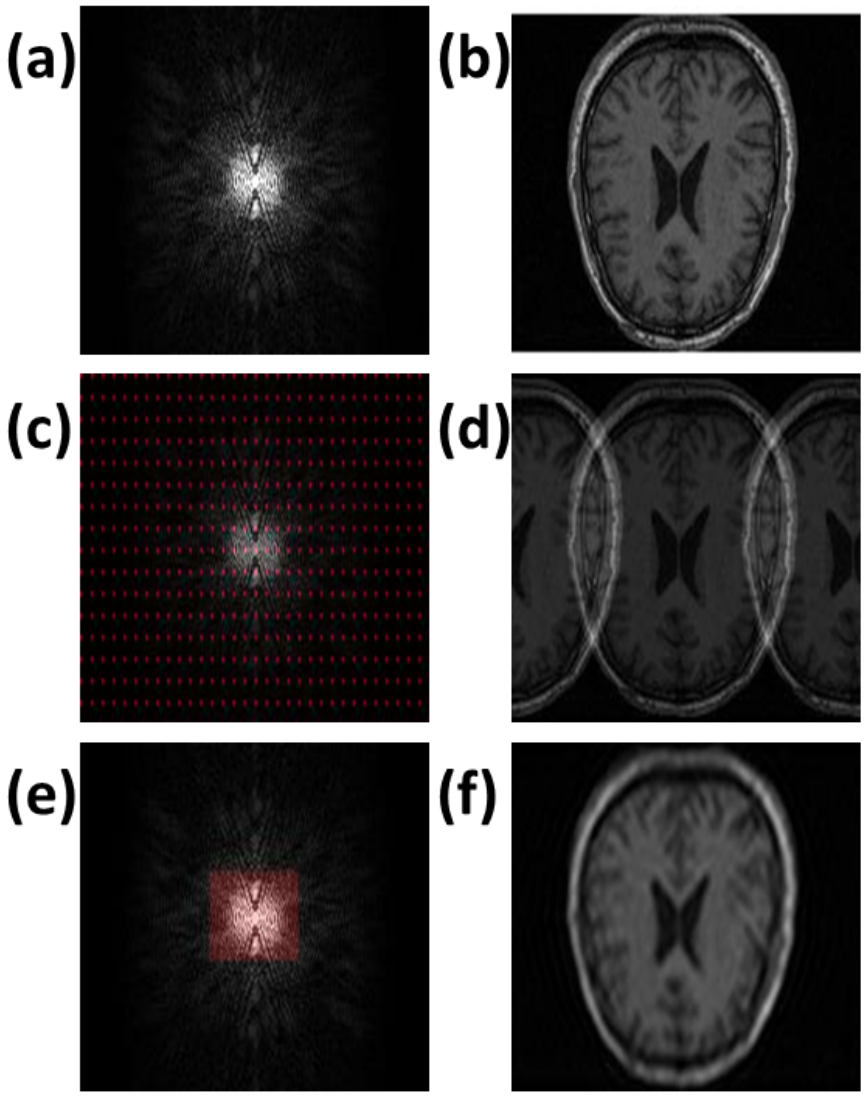

Figure 2.3: Simulation of under-sampling artifacts for Cartesian acquisition. (a) & (b) Nyquist sampled reference k-space and image. (c) & (d) The supported field of view is determined by the sampling density. Coherent folding is produced by insufficient sampling density. (e) & (f) Image resolution is determined by the extent of the k-space that is covered.

can be represented exactly as a linear combination of just a few elements from a known basis or dictionary. Sparse signal models provide a mathematical framework for capturing the fact that in many cases high-dimensional signals contain relatively little information compared to their ambient dimension. An important point in practice is that few real-world signals are truly sparse; rather they are compressible, meaning that they can be well-approximated by a sparse signal. The CS result suggests that it may be possible to sense sparse/compressible signals by taking far fewer measurements, hence the name compressed sensing. Note, however, that CS systems typically acquire measurements in the form of inner products between the signal and more general test functions as opposed to the classic sampling where the signal is acquired at specific points in time.

The compressed sensing approach requires that: (a) the desired signal have a sparse representation in a known sparsifying transform domain, (b) the sampling basis should be incoherent with the sparsifying basis and, (c) a nonlinear reconstruction be used to enforce both sparsity of the signal representation and consistency with the sampled data.

2.2.1 Signal Recovery Formulation

Compressed sensing reconstructs the unknown signal x from its undersampled measurements y, or equivalently solves an under-determined system of linear equations $\mathbf{E}x = y$ by minimizing the l_0 quasi norm (i.e., the number of non-zeros) of the sparse signal $\mathbf{\Psi}x$, where $\mathbf{\Psi}$ represents a global, typically

orthonormal sparsifying transform for the signal and $\mathbf{E}$ is the measurement matrix. CS is formulated as the following problem:

$$\min_{x} \quad \| \mathbf{\Psi} x \|_0 \quad \text{subject to} \quad \mathbf{E}x = y \tag{2.11}$$

This l_0 problem is computationally non-tractable. Alternatively, the l_0 quasi norm is replaced with its convex relaxation, the l_1 norm [29] at which point the problem can be solved via linear programming [18] in the real case, or via second order cone programming in the complex case. In addition to the l_1-norm relaxation, noisy measurements are accommodated by reformulating the problem (2.11) as:

$$\min_{x} \quad \lambda \| \mathbf{\Psi} x \|_1 + \frac{1}{2} \| \mathbf{E}x - y \|_2^2 \tag{2.12}$$

where, λ is a parameter which trades off data fidelity with sparsity This problem is commonly known as the basis pursuit denoising problem [20, 31]. The accuracy of sparse recovery using eqn. (2.12) can be guaranteed if $\mathbf{E}$ and $\mathbf{\Psi}$ satisfy certain mathematical conditions such as: 1) restricted isometry properties (RIPs) [17, 19], 2) incoherence properties [16, 31] and, 3) null-space properties (NSPs) [28].While NSPs provide necessary and sufficient conditions for accurate recovery in absence of noise, in this thesis (chapter 1), the RIPs and the incoherence properties will be used to estimate the efficacy of the various sensing basis employed.

Restricted Isometry Property (RIP)

To define the RIP, first let α_s and β_s denote the largest and smallest coefficients, respectively, such that

$$\alpha_s \parallel \mathrm{x}\parallel_2^2 \ \leq \parallel \mathrm{x}\parallel_2^2 \ \leq \ \beta_s \parallel \mathrm{x}\parallel_2^2 \tag{2.13}$$

is true for all s-sparse N-dimensional vectors x, i.e., x with at most s non-zero entries. A simple generalization of the results in [17] yields that the best possible restricted isometry constant of order s is given by:

$$\delta_s = \frac{\beta_s - \alpha_s}{\beta_s + \alpha_s} \tag{2.14}$$

The recovery performance of (2.12) improves as δ_s gets smaller. It is computationally infeasible to calculate the restricted isometry constant for any order s [55]. However, for the case where $\mathbf{\Psi}$ is a square, invertible matrix, it is relatively straightforward to calculate the δ_1 restricted isometry constant. Lets define $\mathbf{\Phi} = \mathbf{E}\mathbf{\Psi}^{-1}$, then δ_1 can be calculated using (2.14) with

$$\alpha_1 = \min_i \parallel \phi_i\parallel_2 \ , \quad \beta_1 = \max_i \parallel \phi_i\parallel_2 \tag{2.15}$$

where ϕ_i are the column vectors of $\mathbf{\Phi}$.

Incoherency

There are also incoherence conditions on $\mathbf{\Phi}$ that can guarantee good sparse recovery performance [16, 30]. The incoherence-based guarantees are generally weaker than the RIP-based guarantees, but they have been used

previously in the design of sparse MRI encoding schemes [88]. In [88], the authors used the maximum of Transform Point Spread Function (TPSF) as a measure of incoherency between the sensing and the sparsifying basis. The TPSF is defined as:

$$TPSF\{i;j\} = \frac{\phi_i^H \ \phi_j}{\| \ \phi_i \ \|_2 \| \ \phi_j \ \|_2} \tag{2.16}$$

which represents the level of ambiguity between the i^{th} and j^{th} transform coefficients. The maximum of the TPSF is equal to he mutual incoherence μ

$$\mu = \max_{i \neq j} \quad TPSF\{i;j\} \tag{2.17}$$

In [30] or [16], the incoherency is defined as:

$$\mu = \max_{\forall i,j} \frac{e_i^H \ \psi_j}{\| \ e_i \ \|_2 \| \ \psi_j \ \|_2} \tag{2.18}$$

where, e_i and ψ_j are the i^{th} and j^{th} atoms of the sensing matrix $\mathbf{E}$ and the sparsifying basis $\mathbf{\Psi}$, respectively. This description of incoherency simply measures the maximum coherence of the sparsifying basis atoms with that of the sensing basis.

2.2.2 Image Compressiblity in MRI

Signal sparsity or compressibility is a critical requirement for compressed sensing techniques. One way to think about compressible signals is to consider the rate of decay of their coefficients. For many important classes of signals there exist bases such that the coefficients obey a power law decay, in which case the signals are highly compressible. Natural images have a

well-documented susceptibility to compression with little or no visual loss of information. Underlying the most well-known image compression tools such as JPEG, and JPEG-2000 [122] are the Discrete Cosine transform (DCT) and wavelet transform. Medical images are also compressible [75].

The transform sparsity of MR images can also be demonstrated by applying a sparsifying transform to a fully sampled image and reconstructing an approximation to the image from a subset of the largest transform coefficients. To illustrate this, consider Fig. 2.4 in which a typical brain image was compressed with wavelets, and the time series of a cross section of a dynamic heart sequence was compressed by temporal Fourier transform. The important information is captured by 10%, and 5% of the largest transform coefficients, respectively.

2.2.3 Compressed Sensing MRI

The data acquisition model for CS based MRI is given by

$$y = \mathbf{F}_u x + \eta \tag{2.19}$$

where, x is a Nx1 vectorized image, y is the Mx1 sampled data vector in k-space basis, $\mathbf{F}_u$ is the MxN under-sampling spatial Fourier basis with $M \ll N$ and η is the Mx1 noise vector. Figure 2.5 shows the results for CS recovery of a T2-weighted brain image using two different under-sampling methods. The first method acquires samples randomly using a 2D Gaussian distribution with mean at the center of the k-space. The second method uses the Cartesian acquisition scheme and under-samples in the phase encode direction only.

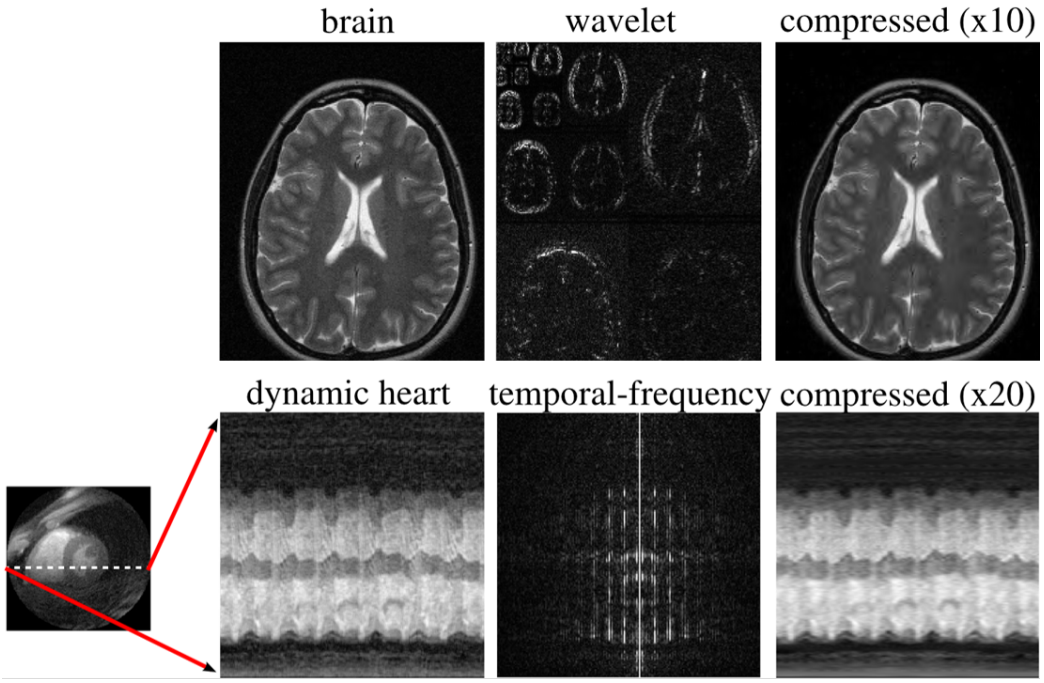

Figure 2.4: Transform sparsity of MR images. Fully sampled images (left) are mapped by a sparsifying transform to a transform domain (middle); the several largest coefficients are preserved while all others are set to zero; the transform is inverted forming a reconstructed image (right). Portions of figure originally appeared in [89]

Clearly, large aliasing artifacts are observed for the Cartesian under-sampling which happens to be the physically realizable under-sampling scheme. For results presented in fig. 2.5, Wavelet basis is chosen as the sparsifying transform (ψ) in eqn. (2.12).

2.3 Linear Dynamical Systems Model

Linear dynamical system (LDS) models are generic and exhibit a wide applicability for modeling physiological functions. They have been previously used to model physiological processes such as: 1) blood flow in MR angiography and perfusion studies and, 2) periodic motion in cardiac and abdominal imaging [103, 141]. Thus, we briefly review the LDS model here. In the classic dynamical systems literature, a model for a changing state vector and measurement process is often described by the following equations:

$$x_k = f_k\left(x_{k-1}\right) + u_k \tag{2.20a}$$

$$y_k = \mathbf{H}_k\, x_k + v_k \tag{2.20b}$$

where, $x_k \in R^N$ represents the signal of interest, $f_k\left(.\right)|R^N \rightarrow R^N$ represents the known evolution of the signal from time $k-1$ to k, $y_k \in R^M$ is a set of linear measurements of x_k, $v_k \in RM$ is the associated measurement noise, and $u_k \in R^N$ is the modeling error for $f_k(.)$ (commonly known as the innovations). The task of estimating the evolving state x_k has become the topic of innumerable studies and algorithms. A special, well studied, case of the system (2.20) is the Kalman Filter [68] which assumes Gaussian statistics on both the measurement

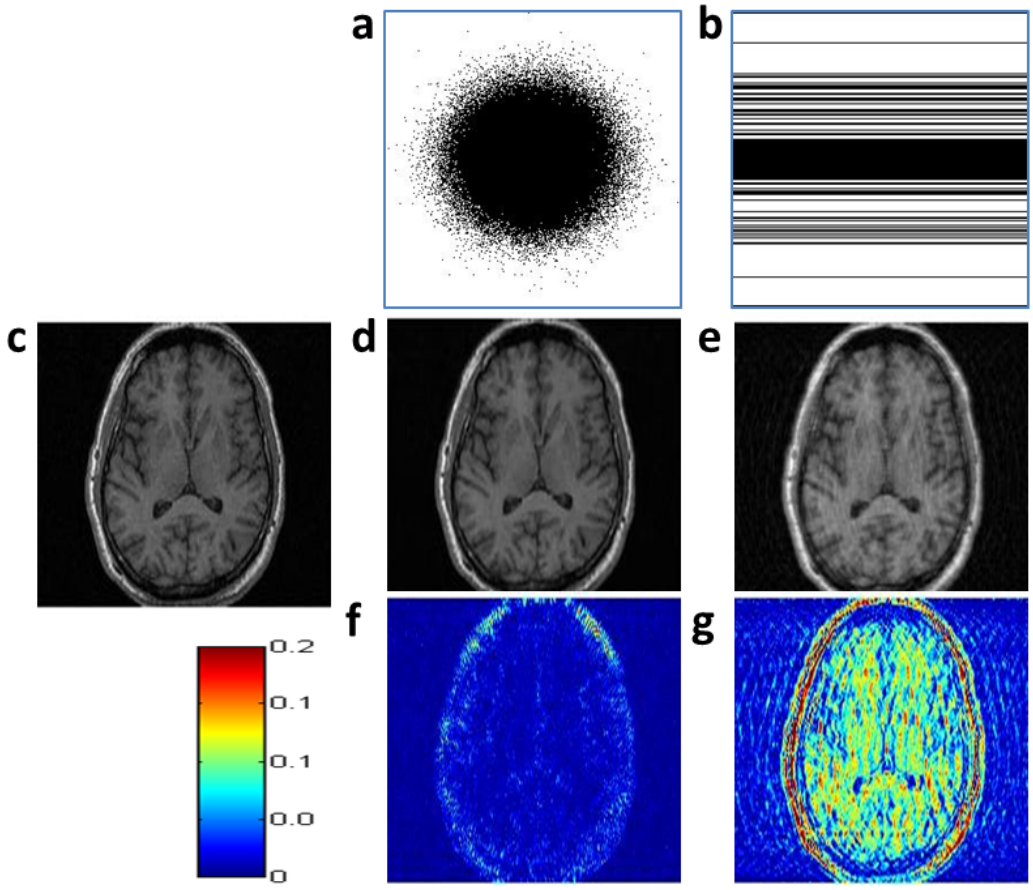

Figure 2.5: Compressed sensing of a T2-weighted brain MR image a) Gaussian distributed sample-points (black dots) in k-space, b) Variable density 2DFT undersampling, sampled phase encode lines are shown as black-lines, c) Reference image, d) CS-MRI recovered image using samples from a, and e) recovered image using samples from b, f) & g) recovery error maps for Gaussian and Cartesian undersampled images.

noise ($v_k \sim \mathcal{N}(0, \mathbf{R}_k)$) and the modeling error ($u_k \sim \mathcal{N}(0, \mathbf{Q}_k)$) , and a linear state evolution function (i.e. $f_k(x_k) = \mathbf{A}_k \; x_k$). The corresponding fixed-interval Kalman filter solves for the following problem

$$\min_{x_1,\ldots,x_k} \sum_{i=1}^{k} \tau_i \parallel x_i - \mathbf{A}_{i-1} x_{i-1} \|_2^2 + \sum_{i=1}^{k} \lambda_i \parallel \mathbf{H}_i x_i - y_i \parallel_2^2 \tag{2.21}$$

where, $\{\tau_i\}_{i=1}^k$ and $\{\lambda_i\}_{i=1}^k$ are the weight factors for the system innovations and measurement noise. The optimal least squares estimate in eqn. (2.21) sought by the Kalman filter essentially requires the inversion of a large matrix with sub-matrices consisting of the measurement matrices $\mathbf{H}_k$, the dynamics matrices $\mathbf{A}_k$, and the identity matrix. The main result of the Kalman filter shows that the full matrix inverse need not be calculated if, at each iteration, we are interested only in the estimate of the current state given previous measurements. Instead each state at time k can be solved for by a temporally local calculation which yields the same solution as performing the calculation intensive inverse, thereby immensely reducing the complexity in terms of the inverse problem that needs to be solved. Additionally, given the least-squares nature of the objective, the problem setup permits an analytic solution. The efficiency given both the analytic and local nature of the solution, coupled with the increasing calculation speed of matrix operations has opened the door for optimal, fast, realizable tracking in a framework common enough to be widely applicable. The underlying assumptions the Kalman filter makes on the system (linearity and Gaussianity), however, can be quite restrictive in broader settings: Any deviation may cause the algorithm to yield erroneous solutions.

Many modifications have been devised to address this shortcoming including the Extended and Unscented Kalman filters [56, 129] to address nonlinear state dynamics and many variations of robust Kalman filters have been designed to address non-Gaussian noise models [35, 43]. Since most system and noise models are difficult to account for analytically and efficiently, most of these extensions attempt to modify the resulting Kalman filter algorithm directly in order to increase the robustness of the estimation. The one main shortcoming of the Kalman filter and its derivatives is that none of the algorithms explicitly take into account any underlying signal structure (such as sparsity in the signal).

2.4 Fast Magnetic Resonance Imaging

Traditional MRI suffers from speed limitation caused by instrumental (gradient amplitude and slew-rate) and physiological (nerve stimulation) constraints. Therefore, in recent years, improvement of MR imaging speed has been a focus of many research groups. In essence, the speed gain is obtained by under-sampling k-space, which violates the Nyquist criterion. Therefore, different approaches have been designed to mitigate the resulting aliasing artifacts. Here I present a short review of the methodologies previously used for improving MRI speeds. In this review, we classify these methodologies in four broad groups. This review provides an overview of the previously used methodologies and the reader is encouraged to refer to the publications for details.

The first group of methods aim to generate artifacts which are incoherent or less observable to human eyes [52, 113, 123] at the cost of reduced apparent Signal to Noise Ratio (SNR). The density weighted phase encoding method in [52] advances the traditional uniform or accumulation-weighting method by combining the improved shape of the spatial response function and the high SNR of acquisition-weighting with an extended field of view.

The second group of methods are based on exploiting the redundancy in k-space, including partial Fourier methods [92], reduced-field-of-view methods [58], parallel imaging [9, 53, 54, 63, 107, 119], and prior-information driven approach [124]. These methods reduce the acquisition time by collecting only a subset of k-space information. The missing data can be recovered by exploiting the correlation hidden in the k-space data and each time frame is handled independently. For example, in parallel imaging methods, spatial information is encoded into the measured data by the spatially-varying sensitivity profiles of each coil, and if the coil sensitivity for each coil can be calibrated accurately and the coils are sufficiently linearly independent, then images can be obtained through the application of suitable signal processing algorithms [26, 80, 106].

The third set of methods are based on utilizing either the temporal redundancy only or in addition to the spatial redundancy [42, 91, 94, 118, 120, 125, 133, 134]. The advantage of these methods is that more relevant correlations are exploited to achieve higher acquisition speed and improve estimation of the missing data. In [39, 118, 120], the dynamic MRI process is modeled as a linear dynamical system and the traditional Kalman filter is used to update

image each frame based on previous estimate and under-sampled data. The k-t FOCUSS technique [66, 67] encodes the redundancy in the temporal dimension using prediction schemes and in a subsequent step, uses the sparsity of the residual time-series to recover images.

The fourth group of methods is based on compressed sensing. In addition to spatial sparsity based techniques [87] mentioned above, there are few other techniques that enforce sparsity in both the spatial- and temporal dimensions. In [41, 90] sparsity in the wavelet transform domain and the temporal Fourier domain is used in the spatial and temporal dimension, respectively. Low-rank matrix completion techniques are a slight variation of CS based techniques. In these methods, for dynamic MRI, the time-frames are stacked as columns of a data matrix and correlations between time-frames are used to recover a matrix with low-rank from its partial observations[143]. These methods only exploit the temporal correlation while recovering the sequence; they do not utilize information about spatial redundancy.

Chapter 3

Fast MRI using Dictionary Learning and Radio-Frequency Tagging Pulses

3.1 Introduction

For dynamic magnetic resonance imaging (MRI) applications, a critical requirement is to reduce acquisition times while maintaining high spatial resolutions to capture the underlying physiological functions with high information rates. However, due to physical and physiological limitations the data acquisition in MRI is sequential in time, which leads to a trade-off between: 1) the temporal resolution, 2) the spatial resolution and, 3) the signal-to-noise ratio of the recovered images [14, 84, 99, 135]. Improvement in MR imaging speeds is achieved by acquiring reduced amount of raw data than that specified by the Nyquist sampling theory [84, 99]. Previously, many image recovery techniques based on exploiting the data redundancy in the spatial and/or the temporal dimensions have been proposed [59, 94, 104, 113, 124, 125]. These techniques have shown limited performance improvement at low acceleration factors. More recently, fast MRI techniques based on the theory of Compressed Sensing [15, 30] have emerged [21, 55, 66, 87, 88, 108, 109, 117]. CS based MRI (CS-MRI) methods rely on recovering the sparse representation of the underlying image in a sparsifying basis which exhibits high incoherency with the

sensing basis [15, 87]. The maximum acceleration achievable by a CS-MRI method depends on two factors, namely: 1) the degree of sparsity of representation of images in the sparsifying basis and, 2) the incoherency between the sensing and the sparsifying basis. Thus, a joint optimization of both the sensing and the sparsifying basis is needed, which is a difficult problem to solve. Consequently, two simpler sub-problems have been derived from the original problem and solved for, in an attempt to improve the performance of the CS-MRI methods. The first problem corresponds to learning of non-standard transforms to allow for highly sparse representation of images while the sensing basis is fixed. The second problem corresponds to modifying the sensing basis in order to improve the incoherency with a fixed sparsifying basis. This chapter presents a technique to improve dynamic MR imaging speeds by synergistically combining a sparsity-enforcing redundancy encoding with a novel physically realizable MR signal encoding formulation.

The seminal paper on CS-MRI used the wavelet basis as the sparsifying basis [87]. Few research studies have proposed on using union of multiple standard frames in order to improve the sparsity of representation by introducing over-completeness in the representation. Furthermore, few studies have proposed on learning a basis from available training data using dictionary learning algorithms [21, 109, 117]. Dictionary learning algorithms learn a basis which allows for highly sparse representation of signals in the training data [1, 50, 112]. In [21, 109, 117], the authors propose to learn a dictionary for sparse representation of image patches using the K-SVD dictionary learning algorithm [1].

The image-patch dictionary encodes for the high frequency information due to its inherent spatial-localization property. However, the under-sampling scheme utilized in [21, 109] acquires the high frequency information at a lower density than it acquires the low frequencies and this ratio gets smaller with increasing acceleration factors. Thus, at high accelerations the non-linear recovery is sub-optimal due to the lack of relevant driving information. Consequently, the approches of [21, 109] show limited performance improvements beyond moderately high acceleration factors (≥ 3). In [117], the authors propose to learn multiple dictionaries in multiple transform domains in order to achieve high redundancy encoding in dynamic MRI while simultaneously enforcing sparsity of signal representations. Dictionaries in the spatial-Fourier space and the image-patch space are proposed to encode the redundancy in both the central and the peripheral regions of the k-space. The spatial-Fourier dictionary allows for stronger under-sampling in the central k-space which allows for relatively denser acquisitions of high frequencies in [117] as compared to the approaches of [21] and [109]. As a result the technique in [117] shows slower recovery performance degradation with increasing accelerations when compared to [21, 109]. However, due to the nature of the 2DFT acquisitions, the under-sampling in the central k-space in [117] translates to "low-energy" additions in the high frequency information. Thus, to further improve the performance of sparsity-enforcing redundancy encoding based CS-MRI methods the underlying MR signal encoding needs to be modified. The modification should acquire the k-space information uniformly across all acceleration factors.

In MRI, spatial localization is encoded using magnetic field gradients which result into a frequency based position encoding [84, 99, 135]. Thus, the standard MR signal encoding is the (multi-dimensional) spatial-Fourier transform which is commonly referred to as the k-space. In recent years, few studies have proposed modification of the underlying signal encoding to improve the incoherency requirements of the CS theory [55, 108]. In [55], a random encoding framework using tailored spatially-selective radio frequency (RF) pulses is presented. Randomized RF excitation pulses are used to spatially vary the sample weights within the field-of-view (FOV) for each MR excitation prior to the gradient encoding. Similar to [55], in [108] authors propose to reduce the coherence between the sensing and the sparsifying basis using spatial modulations but the modulations are realized using a second-order shimming coil instead of RF pulses. In [108] the modified signal encoding corresponds to pre-modulation of the image with a linear chirp before the standard Fourier encoding is applied. A critical difference between [55] and [108] is that the former uses a unique randomized spatial modulation for each excitation whereas the modulation remains constant for all excitations in [108], which translates into a relatively higher coherency reduction for [55]. A limiting factor for the aforementioned encoding formulations is their accurate realization on the physical hardware. Due to the limitations of the current excitation hardware and shimming coils, the physically realizable encoding formulation differs from the theoretical formulation resulting in recovery errors which are further amplified by the ill-conditioning of the encoding formulation [55, 108].

This chapter presents a fast dynamic MRI method using a novel MR signal encoding formulation. The proposed dynamic MRI method like [117] uses dictionary learning for sparse representation of image-patches for redundancy encoding but uses a new MR signal encoding formulation based on spatial modulations using tagging radio frequency (RF) pulses for raw data acquisition. Tagging RF pulses are used clinically in cardiovascular MRI for evaluation of regional myocardial functions [2, 4, 11, 40, 60, 101]. The tagging pulses can be broadly classified into two categories based on the visibility of tags in reconstructed images and the post-processing required for quantification of the myocardial motion [60]. The first category relies on saturation of the longitudinal magnetization to create visible markers in the MR image and requires exhaustive post-processing to track the created markers over time to quantify the myocardial motion [4, 11, 40]. The visible markers can be parallel lines, grid pattern or radial stripes. The second category of techniques is based on the k-space perspective of the tagging [2, 101]. These techniques do not show any visible markers in reconstructed images and motion is quantified using phase tracking methods. The second category of techniques is based on the fact that tag implementation leads to a convolution of the spectrum of the underlying images with that of the tag pattern. i.e., the RF tagging pulses result in mixing of the information in the k-space. More importantly, the RF tagging pulses are physically realizable and versatile with the respect of the tag patterns that can be generated [4, 60].

The novel signal encoding formulation varies the spatial weights for

each MR excitation within the imaging slice using tagging pulses. Specifically, the spatial magnitude modulation (SPAMM) pulse sequences are proposed to be used to generate the spatial weights [4]. Motivated by the hardware limitations of the previously proposed modifications to MR signal encoding [55, 108], the tagging RF pulses based encoding formulation is proposed. Since, the new formulation uses clinically active SPAMM RF pulses its hardware realization will be closer to its theoretical modeling than that for the randomized formulation of [55]. The true innovation of the proposed fast dynamic MRI method is the synergistic combination of image-details based redundancy encoding with the tagging based MR signal encoding formulation. The modulation of spatial amplitudes in the proposed signal encoding formulation leads to acquisition of data samples which are mixtures of the standard k-space samples. Thus, the new formulation leads to a more uniform coverage of k-space information even at high accelerations unlike the variable density under-sampled Fourier encoding previously used in [21, 42, 109, 117]. The preliminary results of dynamic MRI recovery experiments on an in-vivo myocardial perfusion data set show that the proposed tagging based signal encoding preserves the edges and fine structures better than the previously used encoding methods.

The rest of this chapter is organized as follows. Section 3.2 details the tagging RF pulses based signal encoding formulation. Section 3.3 summarizes the image-patch based dictionary learning algorithm and an experiment comparing the compressibility of an image in the dictionary with that in a wavelet frame. Section 3.4 details several experiments and their results which evaluate

the recovery performance of the tagging RF pulses based signal encoding with various sparse recovery models and compares its relative performance with the encoding formulations of [55] and [108]. Finally, section refsec:sa1F concludes the chapter.

3.2 Tagging RF Pulses based MR Signal Encoding

The MR signal acquisition equation for a single excitation is

$$d(k_m) = \int w_m(r)\,\rho(r)\exp(-i2\pi k_m.r)\,dr \tag{3.1}$$

where, k_m is the m^{th} sampling trajectory in the k-space, $d(k_m)$ are the corresponding samples, $\rho(r)$ is the desired image and w_m is a weighting factor. The k-space trajectory $k_m(t) = \frac{\gamma}{2\pi}\int_0^t G(\tau)\,d\tau$ is the time-integral function of the magnetic field gradients $G(\tau)$ employed and γ is the gyromagnetic ratio, a known constant unique for different nuclear species. In clinical MRI, w_m remains constant for all excitations of the image acquisition procedure and can account for spatial modulations either due to the fixed spatial sensitivity of a surface coil or the spatial magnetization modulation obtained using tagging pulses, i.e., in clinical MRI, $w_m(r)$ is not a function of m. In the proposed MR signal encoding formulation the weight vectors $w_m(r)$ will be different for each excitation. For varying the weights $w_m(r)$, the clinically-in-use radio frequency (RF) pulses will be used. Specifically, the SPAtial Magnetization Modulation (SPAMM) pulses are used.

3.2.1 SPAMM Tagging Pulses

The SPAMM tagging pulses rely on perturbing the longitudinal magnetization prior to the imaging stage. The SPAMM pulses wrap the magnetization in a sinusoidal fashion through space by applying two equal-strength non-selective RF pulses separated by a 'wrapping' gradient [4, 60]. Fig. 3.1 shows the sequence diagram of the SPAMM pulses. The first RF pulse tips the longitudinal magnetization in the transverse plane with all spins in phase. The following gradient pulse along the desired tagging direction wraps the transverse magnetization in a sinusoidal direction along the gradient direction through incremental phase shifting of the spins. The magnitude of the gradient pulse controls the period of the sinusoidal modulation in the transverse magnetization. The modulated transverse magnetization is restored back in the longitudinal plane by the second RF pulse. The spatial magnetic modulation for (what appears to be a) parallel line tag pattern can be represented as

$$w_m(r) = \left| \cos \frac{2\pi}{T_m} \, \vec{r}.\vec{v}_m \right| \tag{3.2}$$

where, T_m is the period of the modulation, $\vec{v}_m$ is the vector gradient field applied during the tagging phase, (.) is the dot product operator and, |.| is the absolute value operator. The magnitude of $\vec{v}_m$ controls the period of the sinusoidal modulation and its direction identifies the axis of signal modulation. For obtaining a gridded-tag pattern two SPAMM tagging pulses with perpendicular $\vec{v}_m$ directions are used [60].

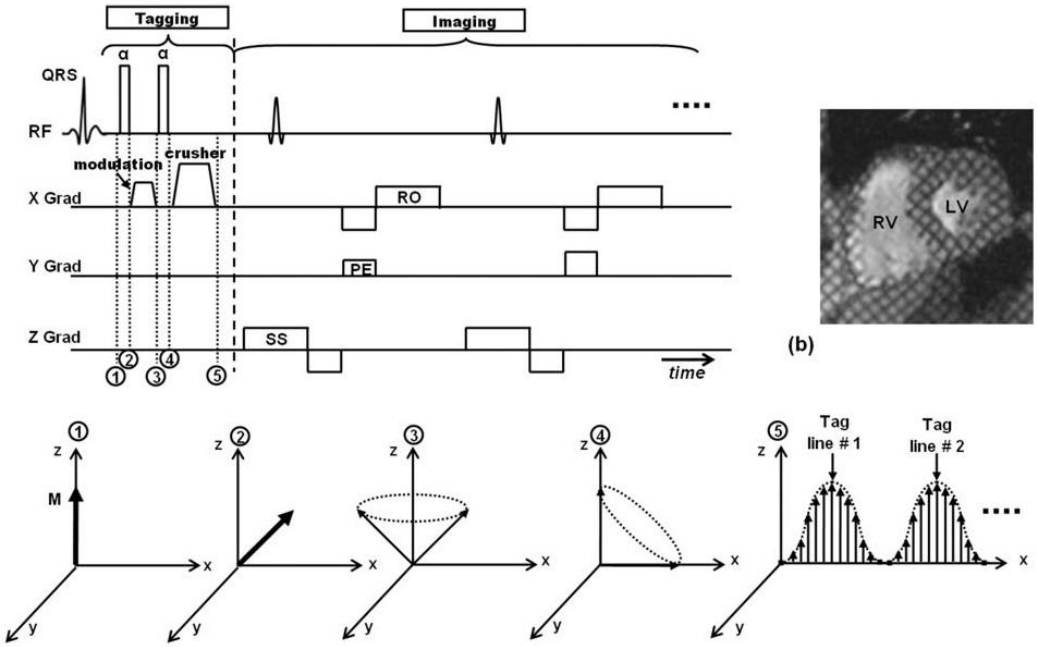

Figure 3.1: **Top-Left**: Pulse sequence diagram for SPAtial Magnitude Modulation (SPAMM) tagging. The tagging part consists of only two non-selective RF pulses (usually, 90°each), separated by the "wrapping" gradient gradient in the tagging direction. The imaging part shows conventional 2DFT (RO = readout, PE = phase encoding, SS = slice selection). **Top-Right**: Example of a SPAMM grid-tagged image showing left ventricle (LV) and right ventricle (RV). Note that this grid pattern needs the application of two tagging stages in the orthogonal directions before imaging takes place. **Bottom**: Evolution of spins during different time points in the tagging stage, as follows: immediately before tagging application (1), the magnetization (M) is at equilibrium state in the longitudinal direction. Immediately after the application of the first RF pulse (2), the magnetization is tipped into the transverse direction by a fixed flip angle (45° RF pulses in the illustration). The "wrapping" gradient then follows, which disperses the spins in the tagging direction (x-direction in this case), such that by the end of the gradient pulse (3), the spins are modulated by incremental phase shifts along the x-axis. The second tagging RF pulse tips the resulting modulated magnetization by another 45° into the transverse direction to result in spins modulated as shown at time point (4). A crusher gradient immediately follows to eliminate transverse magnetization components, leaving only the longitudinal parts, which show a sinusoidal pattern along the x-axis with values ranging from 0 to M (5). Figure originally appeared in [60]

3.2.2 Tagging based Signal Encoding

In the proposed encoding formulation, the weight factor w_m is varied for each excitation using the tagging RF pulses. As stated earlier, the spatial modulation of magnetization leads to convolution in the spatial-Fourier domain (k-space). Thus, in the new formulation, the acquired data is a mixture of samples acquired in standard MRI encoding. This mixing results in dispersion of the energy of k-space samples in their neighborhoods, which is referred to as the spectrum spreading in [108]. But unlike [108], the proposed encoding uses multiple spreading waveforms using the flexibility of the SPAMM sequences. Towards this end, the following MR signal encoding framework is proposed:

$$d(k_m) = \int w_m(r)\,\rho(r)\exp\left(-i2\pi k_{(m,x)}x\right)dx \tag{3.3}$$

Ideally, the spatial modulation $w_m(r)$ in (3.3) can be obtained through concatenation of multiple tagging phases before the imaging phase. However, for practical purposes and for all results presented in this chapter, concatenation of two tagging phases is used. This allows for mixing along multiple dimensions of k-space and time-efficient physical realization of the SPAMM sequences [4]. A discretization of (3.3) can be represented as

$$d_{TE,i} = \mathcal{F}_{1d}\,\mathbf{W}_{TE,i}\,\rho \tag{3.4}$$

where, $d_{TE,i}$ are the tag encoded samples for the i^{th} excitation, $\mathcal{F}_{1d}$ is the 1-dimensional Fourier transform matrix, $\mathbf{W}_{TE,i}$ is the discrete spatial modulation and ρ is the vectorized-image. Extending the equation (3.4) to M excitations,

the complete tagging based MR encoding formulation can be represented as:

$$d_{tag} = \begin{bmatrix} \mathcal{F}_{1d} & \mathbf{0} & \dots & \mathbf{0} \\ \mathbf{0} & \mathcal{F}_{1d} & \dots & \mathbf{0} \\ \vdots & \vdots & \ddots & \vdots \\ \mathbf{0} & \mathbf{0} & \dots & \mathcal{F}_{1d} \end{bmatrix} \begin{bmatrix} \mathbf{W}_{TE,1} \\ \mathbf{W}_{TE,2} \\ \vdots \\ \mathbf{W}_{TE,M} \end{bmatrix} \rho \tag{3.5a}$$

$$= \mathbb{F}_{1d}\, \mathbf{C}_{tag}\, \rho \tag{3.5b}$$

$$= \mathbf{E}_{tag}\, \rho \tag{3.5c}$$

where, d_{tag} are all the acquired tag encoded samples, $\mathbf{E}_{tag}$ represents the encoding matrix and $\{W_{TE,i}\}_{i=1}^{M}$ are the M spatial modulations used.

For all results presented in this chapter, SPAMM sequences capable of creating sinusoidal spatial modulations in two separate-directions are considered. To achieve this each sequence is parameterized using 4 variables, namely: 1) the two sinusoidal periodicities $T_{m,1}$ and $T_{m,2}$, and 2) the two directions of modulation axis, $\vec{v}_{m,1}$ and $\vec{v}_{m,2}$. Specifically, the spatial modulation patterns are realized as:

$$w_m(r) = \left|\cos \frac{2\pi}{T_{m,1}}\, \vec{r}.\vec{v}_{m,1}\right| \left|\cos \frac{2\pi}{T_{m,2}}\, \vec{r}.\vec{v}_{m,2}\right| \tag{3.6}$$

For all experiments, the four parameters are randomly selected from uniform distributions over the following intervals: 1) $T_{m,i=1,2} \in [2\ 28]$, 2) $\angle(\vec{v}_{m,1}, \vec{x}) \in [-\pi/4\ \pi/4]$ and, 3) $\angle(\vec{v}_{m,1}, \vec{v}_{m,2}) \in [\pi/18\ \pi/4]$. Figure 3.2 shows an example of tagging RF pulses based signal encoding. Fig. 3.2a shows the magnitude image of a reference T2-weighted axial brain scan. Figure 3.2b shows an instance of the spatial magnetization modulated image and its zoomed region in Fig. 3.2d. Figure 3.2c shows the magnitude of the tag encoded samples (blue inset)

acquired at an acceleration of 4 along with two zoomed regions (red and green insets) which are scaled individually to show relative magnitudes.

3.3 Redundancy Encoding through Dictionary Learning

As stated earlier, prior to compressed sensing many techniques for fast dynamic MRI were based upon exploiting the data redundancy in the spatial and/or the temporal domain to reduce the data acquired. For example, in [94], under the assumption that in MR angiography the high frequency details change slowly over time, the k-space periphery is heavily under-sampled and is shared between multiple time-frames. Invariably, all the fast MRI techniques, irrespective of the underlying signal encoding under-sample with respect to the Nyquist criteria to reduce acquisition times. In addition, the coarse scale information of an MR image is carried predominantly in the central k-space region and the fine details are spread over the k-space. Consequently, under-sampling irrespective of the underlying signal encoding, results in relatively more information loss for the high-frequency components such as edges and fine structures than that for the low-frequency volumetric content. Thus, a redundancy encoding scheme which allows for sparse recovery of high-frequency content of an image is proposed. Since the high-frequency components are localized in the image domain an over-complete dictionary for sparse representation of image-patches is proposed for encoding redundancy in dynamic MRI applications.

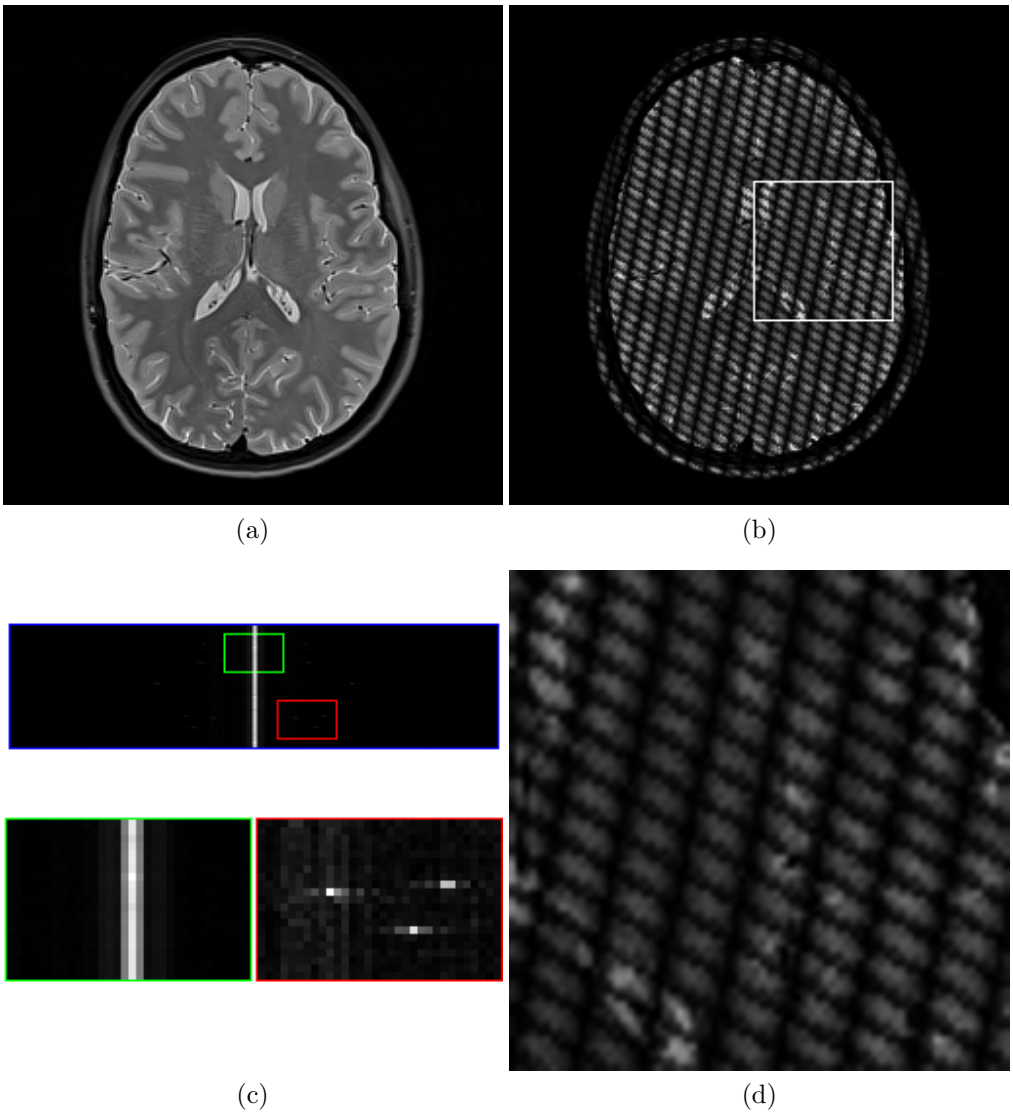

Figure 3.2: Example of under-sampled acquisition (at R= 4) using the proposed tagging radio-frequency pulses based signal encoding. (a) magnitude image acquired using standard Fourier encoding and Nyquist sampling. (b) magnitude image for one excitation of the tagging RF pulses based encoding, a zoomed region of which is shown in (d). (c) magnitude of acquired data (blue inset, 64x256) with zoomed regions shown in reg and green insets.

3.3.1 Dictionary Learning for Image-patches

To learn a patch-based dictionary from a given image u, the following problem is solved:

$$\min_{\mathbf{G},\Gamma} \sum_{j=1}^{J} \| \mathbf{G}\alpha_j - R_j u \|_2^2 \;\; s.t. \;\; \| \alpha_j \|_0 \leq T_0 \;\; \forall\, j \tag{3.7}$$

where, R_j is a patch extraction operator, the l_0 quasi-norm encodes the sparsity of representation and T_0 is the degree of sparsity. Γ is used to denote the set $\{\alpha_j\}_{j=1}^{J}$ of sparse representation of all patches and $\mathbf{G}$ is the patch-based dictionary. The formulation of (3.7), minimizes the total fitting error of all image patches with respect to the dictionary $\mathbf{G}$, subject to sparsity constraints (l_0). The problem (3.7) is non-convex due the non-convexity of the constraint. In addition, for a fixed $\mathbf{G}$ and u, (3.7) reduces to the standard sparse coding problem which is NP-hard [109]. Numerous algorithms have been proposed to solve such a dictionary learning problem [1, 36, 112, 139]. In general, these algorithms alternate between two steps: 1) a dictionary update step and, 2) a sparse coding step. In particular, the k-SVD algorithm [1] has been previously used to learn dictionaries for various image processing applications such as: denoising, inpainting. It has also been used to learn dictionaries for sparse MR recovery techniques [21, 109, 117]. The K-SVD algorithm performs the dictionary update in a sequential manner where each atom of $\mathbf{G}$ is updated jointly with the corresponding representation coefficient for the patches that currently use it. At every dictionary update step, K singular value decompositions are required to update the dictionary $\mathbf{G}$ comprising of K atoms. Thus,

the name K-SVD.

3.3.2 Compressibility in Learned Dictionary

Figure 3.3 compares the compressibility of a T2-weighted axial brain image in a dictionary learned for sparse representation of image-patches with that in the standard Daubechies wavelets. The K-SVD algorithm is used to learn a dictionary **G** with 2048 atoms from randomly selected 10000 image-patches of size 8x8 extracted from the training image shown in Fig. 3.3a. Figure 3.4 shows 256 atoms of the trained dictionary which are maximally used in sparse representation of the test image shown in Fig. 3.2a. The compressed test image in the trained dictionary is shown in Fig. 3.3b, a compression of 6.25% is used which amounts to a sparsity of 4 for 64-dimensional image-patches. Similarly, Fig. 3.3c shows the compressed image in the Daubechies wavelets using 4096 coefficients for a 256x256 image (compression 6.25%). Figures 3.3d-3.3f show the zoomed-in region from the ground truth, the dictionary based compressed image and, the wavelets based compressed image, respectively. Compression quality is measured using signal-to-noise ratio (in dB), structural similarity index (SSIM) [131] and relative error (EOF) and is represented as 3-tuple below the zoomed-region images. Quantitatively, the compression in the trained dictionary is superior than the compression in wavelets. A closer observation of the zoomed-in regions shows that the patch-based dictionary preserves the finer details and thin edges better than the wavelet based compression.

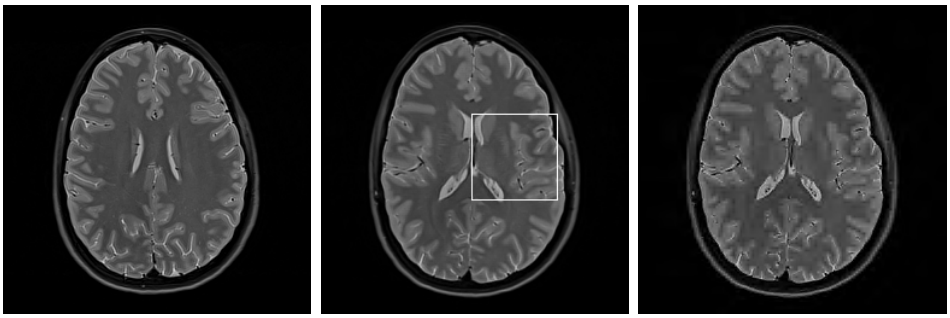

(a) Train (b) K-SVD Dict. (c) Daubechies Wav.

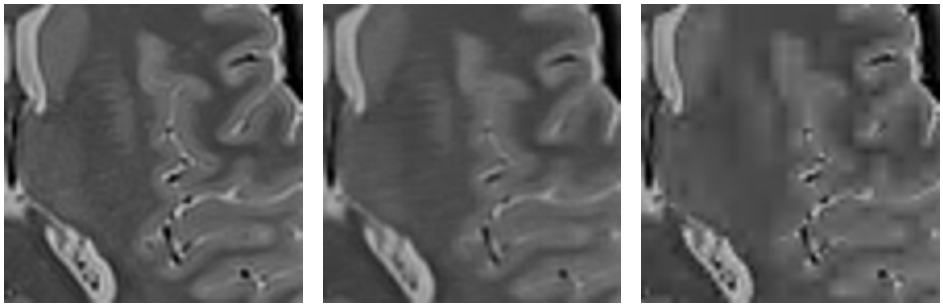

(d) Zoomed Reference (e) (23.8, 0.97) (f) (20.8, 0.89)

Figure 3.3: Comparison of MR image at 6.25% compressibility of a T2-weighted brain axial slice in wavelets and in a dictionary learned for sparse representation of 8x8 image-patches. Quality of the compressed image is presented as (SNR (dB), SSIM, EOF) triple. (a) Training image used for learning a patch-based dictionary with 2048-atoms. Compressed image using: (b) the sparse representation of image-patches and, (c) Daubechies wavelet decomposition. Zoomed-region marked in (b) from (d) ground truth, (e) patch-dictionary based compressed image (f) Daubechies wavelets based compressed image.

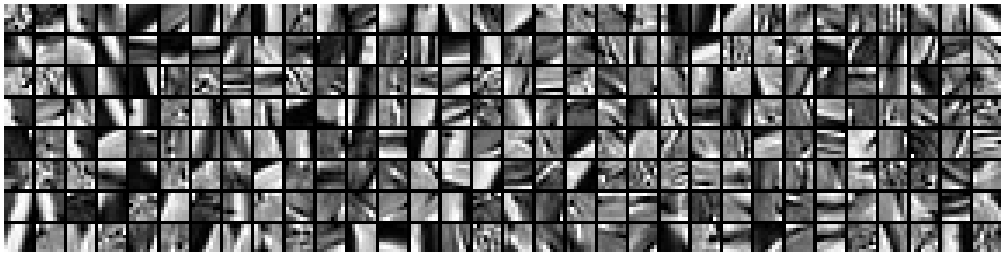

Figure 3.4: First 256 atoms each of size 8x8 from the trained K-SVD dictionary using the train image of Fig. 3.3a. These atoms are the maximal used in sparse representation of image-patches of the test image Fig. 3.3b.

3.4 Experiments and Results

To recover an MR image (ρ) from under-sampled data, the following problem is solved:

$$\min_{\rho} \; f(\rho) \;\; s.t. \; \frac{1}{2} \| \; d - \mathbf{E}_{tag}\rho \; \|_2 \leq \epsilon \tag{3.8}$$

where, ϵ^2 is the estimated upper bound on the noise power and $f(\rho) = \| \; \Gamma \; \|_1$, Γ is the composite representation of all patches of image ρ in the redundancy encoding dictionary $\mathbf{G}$ as described in (3.7). Note, in this section, experiments are also performed with replacing the redundancy encoding by wavelet transform, for which $f(\rho) = \| \; \Psi^*\rho \; \|_1$, where Ψ is a wavelet basis. The solution to (3.8) for all experimental results presented in this chapter are obtained using the the NESTA toolbox which implements the Nesterov's algorithm [7]. Few modifications are made to handle complex images. To quantitatively evaluate the quality of the recovered images following metrics are used: (1) EOF : relative error, (2) SSIM: structural similarity index and, (3) SNR: signal-to-noise ratio. The relative error (EOF) is calculated as $\frac{\|\rho - \rho^*\|_2}{\|\rho\|_2}$, where ρ is the

reference image-vector and ρ^* is the recovered image-vector. SSIM provides a measure to assess the degradation of structural information, it compares local pixel-intensity patterns that are normalized for luminance and contrast [131]. SNR (in dB) is defined as $10\log_{10}\frac{\frac{1}{N}\sum_{i=1}^{N}\left(\rho_i-\rho_i^*\right)^2}{\frac{1}{N}\sum_{i=1}^{N}\rho_i^2}$.

3.4.1 Structural Imaging

A T2-weighted brain data was acquired on a Siemens Skyra (3T) scanner with a turbo spin echo (TSE) sequence with repetition time (TR)= 4s, echo time (TE)= 20ms, field-of-view (FOV): 224mm and a matrix size of 256x256x32 with a slice thickness of 0.8mm, which required a total scan time of 4.26 minutes. This data set has an inplane resolution of 0.875mm at which the fine details are captured with high fidelity. The high resolution details allow to critically evaluate fast MRI techniques based on signal encoding formulations modifications to increase k-space coverage. Figure 3.5 shows the sparse recovery of slice# 16 (same as the reference in Fig. 3.2a) using sparse-representation of image-patches in a learned K-SVD dictionary and under-sampled data at an acceleration factor of R= 4 using the proposed tagging RF pulses based encoding. All images are displayed using the colormap of the reference image. Figure 3.5a represents the minimal energy based minimum $l2$-norm error solution for the acquired TAG samples (d_{tag}) obtained using the Moore-Penrose pseudo-inverse $\mathbf{E}'_{tag}\left(\mathbf{E}_{tag}\mathbf{E}'_{tag}\right)^{-1}\ d_{tag}$, where ($'$) represents the Hermitian operator. Figure 3.5b shows the sparse recovered image at: SNR-20.9dB, SSIM-0.93 and, EOF-0.09. The convergence of the Nesterov's

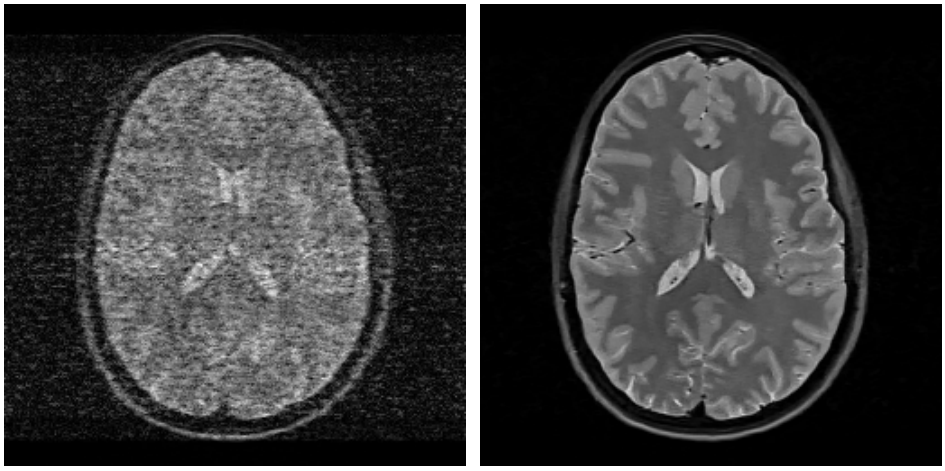

(a) Min. $l2$-norm recovery

(b) Recovered

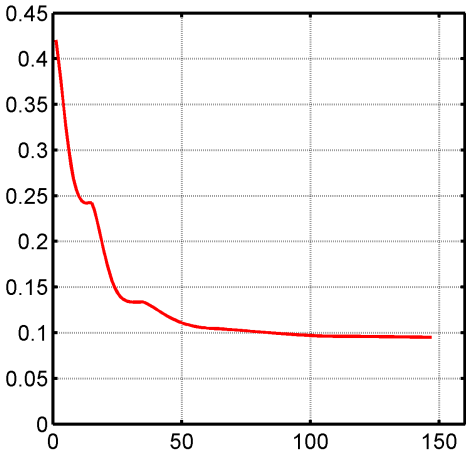

(c) EOF vs. Iteration#

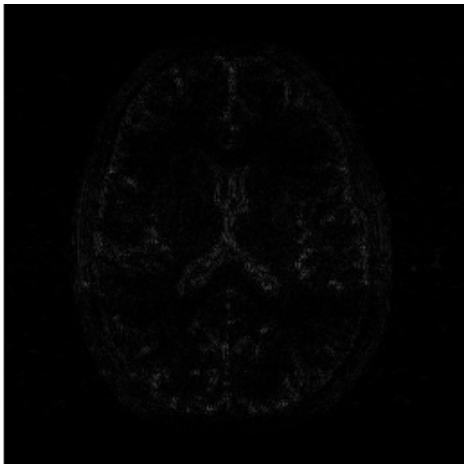

(d) Error

Figure 3.5: Recovery of a T2-weighted brain image using sparsity of image-patches in a K-SVD trained dictionary and the tagging radio-frequency based signal MR encoding at an acceleration of R= 4. (a) Minimum energy recovery using acquired TAG samples (b) Final recovered image (c) Relative error vs. iteration curve (d) Magnitude error image

algorithm [7] for the image-patch dictionary based sparse formulation (3.8) is shown by plotting the relative error vs. iteration number in Fig. 3.5c. Figure 3.5d shows the magnitude error image which has non-negligible errors only in the vicinity of strong transitions and is free of aliasing artifacts.

To separate the benefits of the tagging RF pulses based encoding from those of redundancy encoding using learned dictionaries, multiple experiments are run and reported for. These experiments are simply permutations of two signal encoding schemes (sensing basis) and two sparsifying bases. The tagging based MR signal encoding is compared with the variable density undersampled Fourier encoding scheme and for convenience, hereafter these are identified by the *TAG* and the *VDF* abbreviations, respectively. Similarly, the wavelet basis is selected for comparison with the patch-dictionary based sprasification model and these will be identified by the *Wav.* and *Dict.* abbreviations, respectively. Thus, a permutation of the sensing and sparsifying basis leads to four different experiments, namely: 1) *Wav. VDF*, 2) *Wav. TAG*, 3) *Dict. VDF* and, 4) *Dict. TAG*. *Wav. VDF* corresponds to the seminal compressed sensing approach of [88], *Dict. VDF* is similar to the approaches of [21, 109] and, *Wav./Dict. TAG* correspond to the approaches introduced in this chapter.

Figure. 3.6 shows the recovery of a T2-weighted brain image using the four different recovery schemes at an acceleration factor of R= 4. Fig. 3.6k shows the relative convergence of the four schemes using the relative error vs. iteration number curves. Figure 3.6a shows the zero-filled recovery of *VDF*

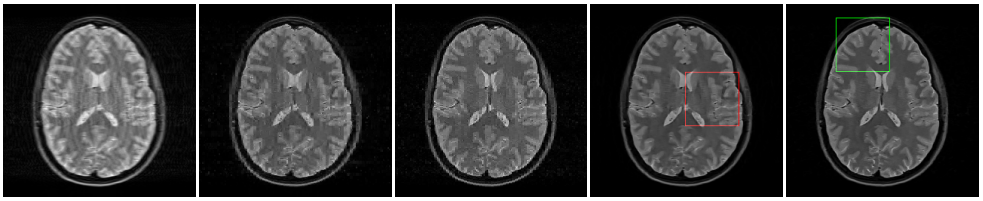

(a) z.f. VDF (b) (15.0, 0.72) (c) (15.93, 0.73) (d) (18.8, 0.91) (e) (20.9, 0.93)

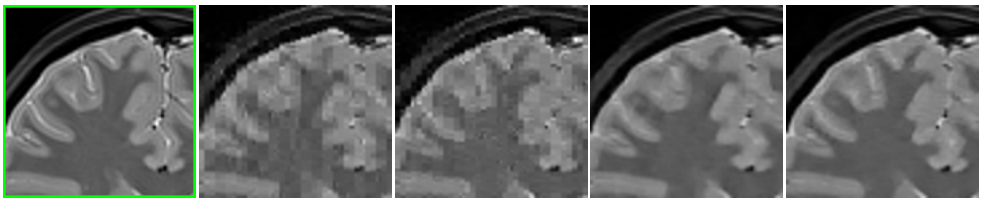

(f) Reference (g) *Wav. VDF* (h) *Wav. TAG* (i) *Dict. VDF* (j) *Dict. TAG*

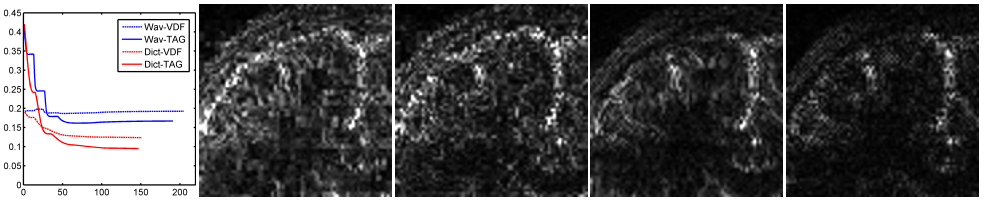

(k) eof vs. iter (l) (17.2, 0.68) (m) (17.8, 0.69) (n) (20.9, 0.84) (o) (22.8, 0.87)

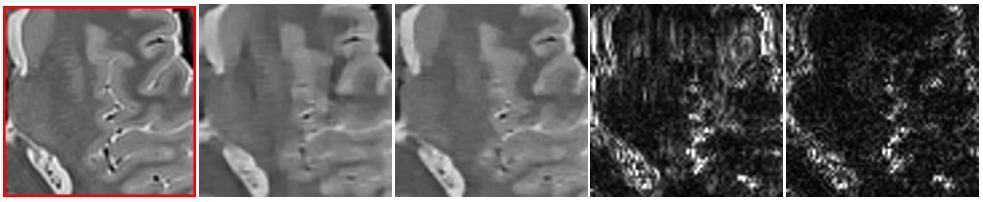

(p) Reference (q) *Dict. VDF* (r) *Dict. TAG* (s) (18.0, 0.76) (t) (20.1, 0.78)

Figure 3.6: Comparison of the proposed tagging RF pulses based signal encoding (*TAG*) and patch-dictionary based redundancy encoding (*Dict.*) with wavelet sparsity (*Wav.*) and the variable density Fourier under-sampling scheme (*VDF*). All images are recovered at an acceleration factor of $R = 4$. Recovered images with the performance metrics are shown in: (b) *Wav. VDF*, (c) *Wav. TAG*, (d) *Dict. VDF* and, (e) *Dict. TAG*. (f) shows a zoomed region from reference image 3.2a, region is marked in (e). (g)-(j) show the recovered images which are identified individually and their corresponding error images with region-based metrics are shown in (l)-(o), respectively. (p) shows a second region as marked in (e), which shows high recovery errors using the *Dict. TAG* method. (q) and (r) show the recovered regions from the *Dict.* based techniques with their corresponding errors images shown in (s) and (t), respectively.

under-sampling where the aliasing artifacts are clearly visible. Figures 3.6b-3.6e show the recovered images using *Wav. VDF*, *Wav. TAG*, *Dict. VDF* and, *Dict. TAG* methods, respectively. The recovery metrics are reported as a 3-tuple (SNR (dB), SSIM, EOF) underneath the recovered images. Based on comparison of the metrics following conclusions can be made: 1) for a fixed sensing basis, the *Dict.* based recoveries have a higher fidelity than *Wav.* frame as the underlying image-patches show a higher degree of sparsity of representation in the learned over-complete basis ($\mathbf{G}$) and, 2) for a fixed sparsifying basis, the *TAG* based encoding preserves the underlying image structure better than the *VDF* sampling scheme as it captures more information corresponding to edges and finer details. A zoomed region from the reference image (green outline in 3.6e) and the recovered images are shown in Figs. 3.6f-3.6j and the corresponding error images with their recovery metrics are shown in Figs. 3.6l-3.6o. All error images are displayed using a grayscale colormap mapped to $0 - 20\%$ of maximum reference image intensity, i.e., all errors greater than 20% of the maximum reference intensity have been mapped to the white color. The *Dict.* based sparse recoveries outperform the *Wav.* based recoveries as the performance metrics for the green region are substantially higher for the former sparsification basis. A second region (red outline in Fig. 3.6e) from the reference and the recovered images using the *Dict. VDF* and *Dict. TAG* are shown in Figs. 3.6p-3.6r, respectively. This region encloses the highest errors in the minimum energy solution of the *TAG* sampling method as seen in Fig. 3.5a. The *Dict. TAG* recovery in this region is prone to be erroneous and com-

paring its performance with the *Dict. VDF* technique in this region will allow for making stronger conclusions on relative benefits of *TAG* encoding method over the *VDF* encoding. In the red region, the stronger boundaries (of ventricles and the brain-boundary in top-right) are captured with higher fidelity in the *TAG* encoding than in the *VDF* encoding (Fig. 3.6q). In addition, there is strong aliasing residual from CSF-based signal from ventricles for the *VDF* encoding which reduces the homogeneity and the underlying structure of gray- and white-matter tissue. The aliasing artifacts are visible as vertical streaks in the error image in Fig. 3.6s. To summarize, the *TAG* encoding avoids deblurring and aliasing caused by the *VDF* encoding scheme which is seen as: 1) better preservation of homogeneity of gray- and white-matter regions: a) in Fig. 3.6h than in Fig. 3.6g and b) in Fig. 3.6r than in Fig. 3.6q and, 2) improved recovery of edges and fine details (easier to qualitatively evaluate in error images) : a) in Fig. 3.6o than in Fig. 3.6n and b) in Fig. 3.6t than in Fig. 3.6s.

3.4.2 Comparison

As stated earlier, few research studies have previously proposed the modification of the underlying MR signal encoding in order to improve the incoherency requirements of the underlying CS-MRI techniques. To further quantify the relative performance of the proposed tagging based encoding formulation with respect to the previously proposed techniques, its performance is compared with the formulations of [55] and [108].

Random Encoding

In [55], the authors use tailored spatially-selective RF pulses to randomize the excitation flip-angles along an encoding direction which results in randomized excitations. This method uses the MR signal encoding formulation of (3.3) and the weight factors w_m are unique for each excitation. Specifically, the weight factor for the m^{th} excitation is modeled as:

$$w_m(x,y) = \sum_{q=Y_{min}}^{Y_{max}} \gamma_{qm}\ \Pi(y-q) \tag{3.9}$$

where, γ_{qm} is a Gaussian random variable parametrized in the a gradient encoding direction (y-axis in above formulation). Now, a discretization of (3.3) yields:

$$d_{(rand,i)} = \mathcal{F}_{1d}\ \mathbf{C}_{(rand,i)}\ \rho \tag{3.10a}$$

$$= \mathcal{F}_{1d}\ \mathbf{C}_{(rand,i)}\ \mathcal{F}_{2d}^{H}\ \mathcal{F}_{2d}\ \rho \tag{3.10b}$$

$$= \mathcal{M}_{(rand,i)}\ d_{2dft} \tag{3.10c}$$

where, ρ is the image-vector, $\mathbf{C}_{(rand,i)}$ is the random encoding based spatial modulation for i^{th} excitation, $\mathcal{F}_{nd}$ is the $n-$dimensional Fourier transform matrix and $\mathcal{M}_{(rand,i)}$ is the corresponding mixing in the k-space. The spatial modulation $\mathbf{C}_{(rand,i)}$ exhibits circular symmetry in a segmented manner (non-overlapping blocks). Now, for the multiple excitations the random encoding

model is:

$$d_{rand} = \mathbb{F}_{1d}\ \mathbf{C}_{rand}\ \rho \tag{3.11a}$$

$$= \mathbb{F}_{1d}\ \mathbf{C}_{rand}\ \mathcal{F}_{2d}^{H}\ d_{2dft} \tag{3.11b}$$

$$= \mathcal{M}_{(rand,mix)}\ d_{2dft} \tag{3.11c}$$

where, $\mathbb{F}_{1d}$ is the block-wise concatenated matrix of $\mathcal{F}_{1d}$ as in (3.5a), $\mathbf{C}_{rand}$ is the spatial modulation matrix for all excitations and $\mathcal{M}_{(rand,mix)}$ is the "mixing matrix" in the k-space. The Encoding matrix $\mathbf{E}_{rand} = \mathbb{F}_{1d}\ \mathbf{C}_{rand}$ is ill-conditioned due to the rank-deficiency of the $\mathbf{C}_{rand}$ matrix. Empirically, the condition number of the $\mathbf{E}_{rand}$ has been observed in the range $(4-5)$. However, the inverse recovery simulations result in images with acceptable accuracy levels. A major limitation is the hardware realization of the spatial modulations using randomized spatially-selective RF pulses.

Spread Spectrum Encoding

In the approach of [108], the weight modulation is achieved using a second-order shimming coil. It is used to modulate the underlying image using a linear chirp signal before the 2DFT excitations and acquisitions are performed. Specifically, the weight modulation is:

$$w_m(x,y) = exp\left(i\pi\left(c_x x^2 + c_y y^2\right)\right) \tag{3.12}$$

where, c_x and c_y are chirp rates in the x- and y-encode directions, respectively. Note that in (3.12) the weight w_m is constant for all excitations, i.e., it is not

a function of $m = (k_x(t), k_y(t))$ and depends only on the physical location $r = (x, y)$. Thus, a single encoding acquisition for i^{th} excitation in [108] can be formulated as:

$$d_{chirp,i} = \mathbf{R}_i \, \mathcal{F}_{2d} \, \mathbf{C}_{chirp} \, \rho \tag{3.13}$$

where, ρ is the image-vector, $\mathcal{F}_{2d}$ is the 2-dimensional Fourier transform matrix, $\mathbf{C}_{chirp}$ is a diagonal matrix which accounts for the linear chirp modulation of the underlying image as in (3.12). Now, for the multiple excitations the spread-spectrum encoding model is:

$$d_{chirp} = \mathbf{R} \, \mathcal{F}_{2d} \, \mathbf{C}_{chirp} \, \rho \tag{3.14a}$$

$$= \mathbf{R} \, \mathcal{F}_{2d} \, \mathbf{C}_{chirp} \, \mathcal{F}_{2d}^H \mathcal{F}_{2d} \;\; \rho \tag{3.14b}$$

$$= \mathbf{R} \, \mathcal{M}_{(chirp,mix)} \, d_{2dft} \tag{3.14c}$$

where, R is the variable density under-sampling operator which selects the spread spectrum encoded samples for the modulated image $\mathbf{C}_{chirp} * \rho$ and $\mathcal{F}_{2d}^H$ is the adjoint 2-dimensional Fourier transform matrix. (3.14c) builds the "mixing in k-space" perspective for the approach of [108]. Since $\mathbf{C}_{chirp}$ is a diagonal matrix, $\mathcal{F}_{2d}\mathbf{C}_{chirp}\mathcal{F}_{2d}^H$ is a circulant matrix but dense as the $\mathbf{C}_{chirp}$ has no inherent periodicity. The Encoding matrix $\mathbf{E}_{chirp} = \mathbf{R}\mathcal{F}_{2d}\mathbf{C}_{chirp}$ is full-rank (row rank) and thus well-conditioned.

Hereafter the approaches of [55] and [108] will be referred to as the *RAND* and *CHIRP*, respectively. Both the *RAND* and *CHIRP* techniques have used the *total-variation* (TV) norm minimization as the sparsifying model

for their recovery formulations. TV-norm minimizes the l_1-norm of the magnitude of the image gradient which is a non-linear operation and cannot be represented as a matrix operation. For all the results presented in this subsection the following problem is solved:

$$\min_{\rho} \quad TV(\rho) \quad s.t. \ \| \mathbf{E}_{encd} \, \rho - d_{encd} \|_2^2 \leq \epsilon^2 \tag{3.15}$$

where, ϵ is an estimate of the noise, ρ is the image-vector and $\mathbf{E}_{encd}$ and d_{encd} are the encoding matrix and under-sampled acquired data, respectively. In addition to the *RAND* and *CHIRP* techniques, the proposed *TAG* formulation will also be compared with the variable density Fourier under-sampling approach which will be referred to as *VDF*. Hence, the signal encoding in equation (3.15) can correspond to any of the following four choices: 1) *VDF*, 2) *CHIRP*, 3) *RAND* and, 4) *TAG*. For fair comparison, all the four techniques are implemented using the Nesterov's algorithm [7] which allows for utilizing identical relative-weighting parameters (ϵ).

Figure 3.7 shows the comparison results for sparse recovery of a T2-weighted brain image at an acceleration of R= 4 from the data set previously described in section 3.4.1. The selected brain slice is the same slice from the results of Fig. 3.6. However, the complex-image-data is processed to allow for linear chirp pre-modulation simulation for the *CHIRP* technique. The complex-data is up-sampled by 2 and is used to simulate the measured raw data (d_{CHIRP}). However, for fair comparison of all encoding schemes, the up-sampled data is down-sampled and used as ground truth to retrospectively generate measured raw data for the remaining techniques, i.e, (d_{VDF}),

(d_{RAND}), and (d_{TAG}). The up- and down-sampling operation results in loss of image details and thus the zoomed reference image of Fig. 3.7k is not as sharp as that of Fig. 3.6p. Consequently, the recovery performance metrics should not be compared between the results of Figs. 3.6 and 3.7. However, a separate comparison of the TV-norm minimization with the *Dict.*-based sparsification approach with TAG signal encoding scheme is presented in section 3.4.3. Figures 3.7b-3.7e show the final recovered images for all the four techniques: *VDF*, *CHIRP*, *RAND*, and *TAG*, respectively. It is difficult to visibly qualify the performance differences from the recovered images, however, the corresponding error images in Figs. 3.7g-3.7j which have been scaled identically, show that the TAG outperforms all other encoding formulations. This is also supported by the performance metrics shown below the error images as the 3-tuple of (SNR (dB), SSIM, EOF). In Fig. 3.7g, the aliasing artifacts are visible near the skull and the brain-boundary for the *VDF* encoding, however, these artifacts are suppressed in the *CHIRP* method although the under-sampling remains unchanged. A comparison of the zoomed error images of Figs. 3.7q and 3.7r shows that the *CHIRP* recovery has relatively lower aliasing artifacts. This effect registers as better recovery of the underlying homogeneous structure in Fig. 3.7m as compared to that in Fig. 3.7l. The *RAND* approach performs superior (although marginally) to the *CHIRP* method for the selected image as it improves upon the fidelity of edges and finer details. The boundaries of the ventricles and the blood vessels in the brain periphery (anterior-posterior direction) show less error in Fig. 3.7i than

in Fig. 3.7h. The proposed *TAG* based encoding improves on the *RAND* approach by better preserving the homogeneity of underlying tissues as can be observed by comparing Fig. 3.7j with Fig. 3.7i. However, it is difficult to comment on relative recovery of fine edges and details between the *RAND* and the *TAG* approaches. For both the approaches, for the given slice, certain edges are better preserved in one approach than in the other. In Fig. 3.7t the boundary of ventricles shows higher error than in Fig. 3.7s whereas the CSF at the brain boundary in the right-top shows higher error in Fig. 3.7s than in Fig. 3.7t. However, based on the performance metrics for the complete image, the *TAG* approach outperforms the *RAND* by almost 2.8 dB. For stronger statistically relevant comparison of the four schemes, figures 3.7f and 3.7p show the ($mean \pm standard\ deviation$) curves for relative error (EOF) and structural similarity index (SSIM) metrics versus acceleration factor (R) for all the 32 slices of the T2-weighted brain data set. From these curves it is easy to conclude that the proposed *TAG* encoding scheme outperforms the other three encoding schemes for the TV-norm minimization based sparse recovery at acceleration factors $R \in [3\ 8]$. The relative trend between the four encoding schemes for wavelet sparse model remains same, however the results are poorer than TV-minimization based recovery. For patch-dictionary based sparse recovery the *RAND* scheme fails to converge and its analysis is out of the scope of this chapter.

To further analyze the relative performances of the four encoding schemes, theoretical measures which represent the performance guarantees of CS recov-

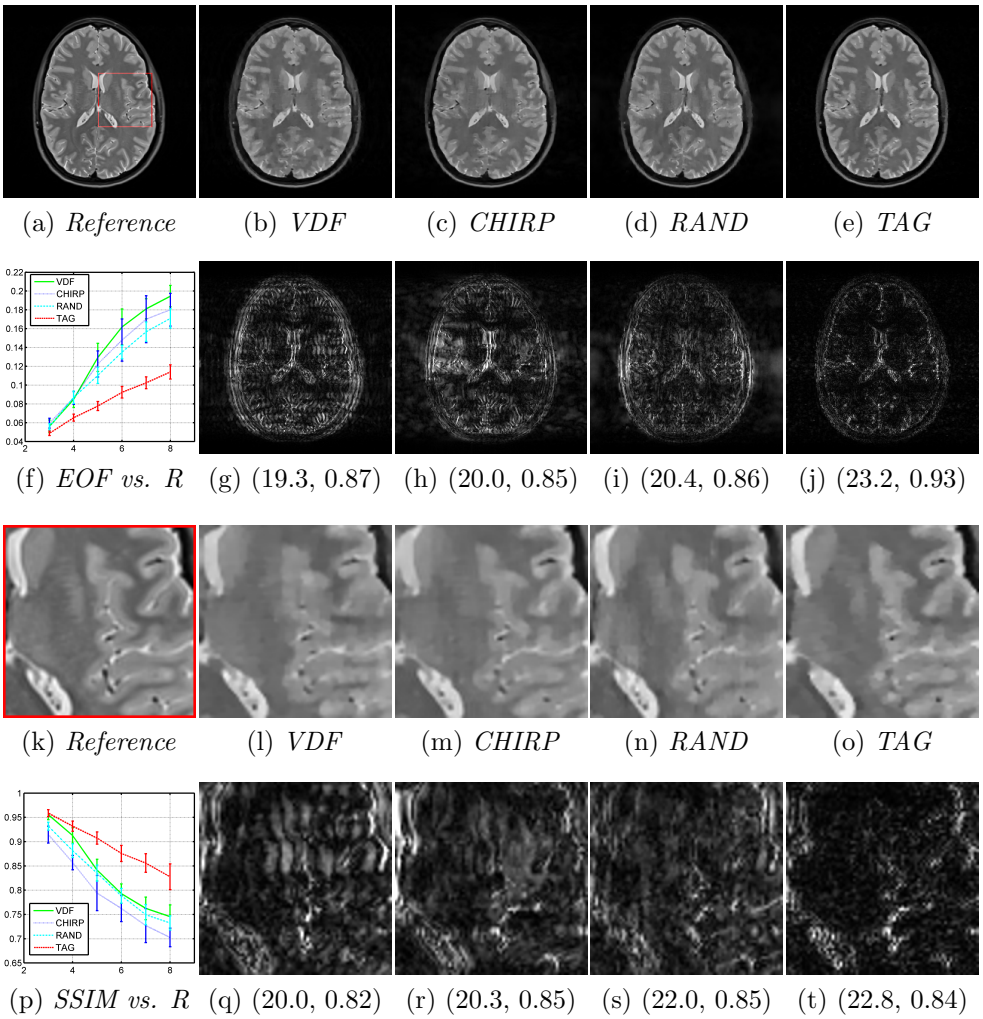

(a) *Reference* (b) *VDF* (c) *CHIRP* (d) *RAND* (e) *TAG*

(f) *EOF vs. R* (g) (19.3, 0.87) (h) (20.0, 0.85) (i) (20.4, 0.86) (j) (23.2, 0.93)

(k) *Reference* (l) *VDF* (m) *CHIRP* (n) *RAND* (o) *TAG*

(p) *SSIM vs. R* (q) (20.0, 0.82) (r) (20.3, 0.85) (s) (22.0, 0.85) (t) (22.8, 0.84)

Figure 3.7: Comparison of the proposed tagging (*TAG*) based signal encoding scheme with: 1) the variable-density Fourier (*VDF*) under-sampling, 2) the spectrum spreading scheme using chirp (*CHIRP*) modulations with second-order shimming coils [108] and, 3) the random-encoding (*RAND*) scheme using tailored spatially-selective radio-frequency pulses [55].

Table 3.1: Restricted Isometry Constants (δ_1) values for different encoding schemes, varying image sizes and varying accelerations. Daubechies wavelet basis is used as the sparsifying basis.

Image size	Signal Encoding	δ_1	
		32 Excitations	64 Excitations
256 x 256	LFF	0.9998	0.9982
	VDF	0.9400	0.8410
	CHIRP	0.9425	0.8542
	RAND	0.5201	0.3567
	TAG	0.6111	0.4458
128 x 128	LFF	0.9165	0.7580
	VDF	0.8460	0.6196
	CHIRP	0.9132	0.8438
	RAND	0.4504	0.3021
	TAG	0.6924	0.5872

Table 3.2: Mutual Coherence (μ) values for different encoding schemes, varying image sizes and varying accelerations. Daubechies wavelet basis is used as the sparsifying basis.

Image size	Signal Encoding	μ	
		32 Excitations	64 Excitations
256 x 256	LFF	0.9005	0.7833
	VDF	0.7147	0.6665
	CHIRP	0.6958	0.6544
	RAND	0.5594	0.4179
	TAG	0.6152	0.4822
128 x 128	LFF	0.9938	0.9855
	VDF	0.6624	0.4133
	CHIRP	0.7003	0.6334
	RAND	0.5086	0.3957
	TAG	0.6360	0.5102

ery are calculated and summarized in Table 3.1 and Table 3.2. Specifically, the restricted isometry constant for 1-sparse vectors from (2.15) and the mutual coherence from (2.17) are calculated for all the four encoding scheme with the Daubechies-4 wavelets used as the sparsifying basis. The measures are the mean values for 10 calculation runs where the encoding $\mathbf{E}$ is randomly generated for each run.

3.4.3 TV-norm versus Patch-Dictionary

Figure 3.8 compares the performance recovery of patch-dictionary based sparsifying basis (*Dict.*) with the *total-variational* norm minimization with the poposed tagging RF pulses based MR signal encoding. Quantitatively, the *Dict. TAG* outperforms the *TV TAG* approach, although marginally. However, a qualitatively comparison of the zoomed-in recovered images of Figs. 3.8b and 3.8c show the relatively poor performance of the TV-minimization in recovery of fine details and preservation of the true tissue structures.

3.4.4 Myocardial Perfusion Imaging

The proposed fast dynamic MRI technique is experimentally validated using an in-vivo myocardial perfusion dataset. The perfusion data was acquired on a 3T Siemens scanner with a saturation-recovery sequence (TR\TE = 2.5/1ms, saturation recovery time= 100 ms) and comprises of an image matrix of size 90x190x70 (phase-encodes x frequency encodes x temporal slices) [85]. For all *Dict.* experiments, a patch-based dictionary $\mathbf{G}$ with 256 atoms

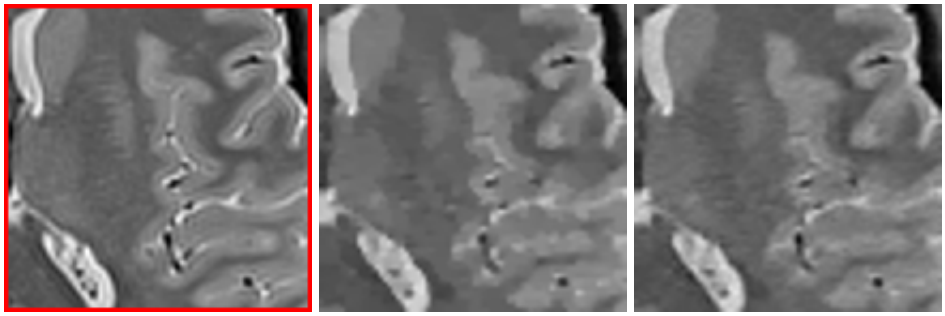

(a) Zoomed ref. (b) *TV TAG* (c) *Dict. TAG*

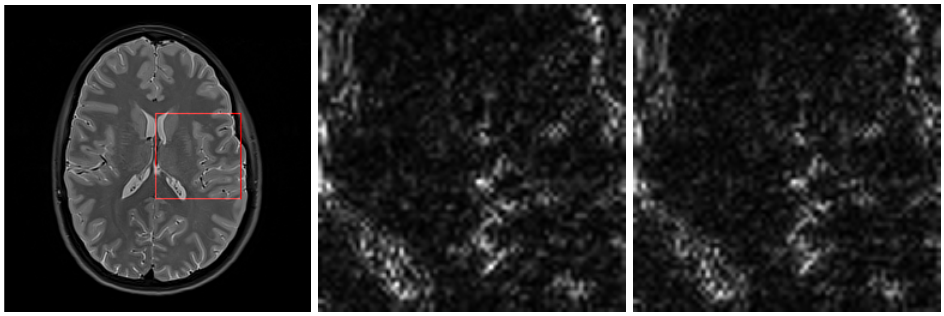

(d) Reference (e) (20.1, 0.89) (f) (21.0, 0.91)

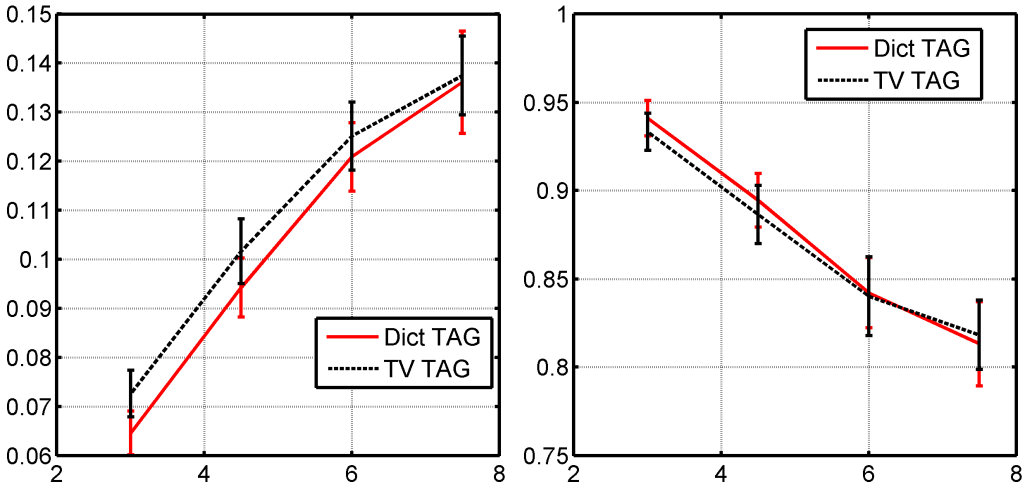

(g) EOF vs R (h) SSIM vs R

Figure 3.8: Comparison of the patch-dictionary based sparse recovery with *total-variation* norm (TV) minimization with the proposed tagging RF pulses based signal encoding formulation at an acceleration factor of $R = 4$.

is trained for 4x4 patches with a sparsity of $T_0 = 5$. To train the dictionary $\mathbf{G}$, 2 fully referenced images are randomly selected from the temporal slices and removed from the test data. Figure 3.9 shows the recovered and the corresponding error images for a temporal slice at an acceleration factor of $R = 4$ for all the four experiments described previously in section 3.4.1. For better visualization of recovered characteristics, only zoomed regions of the recovered and the error images are shown. The error images have been scaled identically. The relative trend between the four techniques for the myocardial perfusion data set is similar to the trand observed in Fig. 3.6 for the T2-weighted brain data set in section 3.4.1. From Fig. 3.9, the following conclusions are made. Firstly, the redundancy encoding using the patch-based dictionary outperforms the wavelet sparsifying basis for both the signal encoding formulations. Secondly, for a fixed sparsifying basis, the TAG encoding outperforms the variable density Fourier sampling method (VDF) at all accelerations $R \geq 4$. Similar trends were reported in section 3.4.1.

Figure 3.10 characterizes the performance of all the four techniques over the complete data set as a function of acceleration (R) in terms of the relative error (EOF) and structural similarity index (SSIM). The marginally lower performance of the TAG compared to the VDF at $R = 3$ can be attributed to the following two reasons: 1) for the data set, most of its k-space energy resides in the central region, thus a Gaussian profile based variable density sampling suffices to capture most of it and, 2) the TAG encoding matrix $\mathbf{E}_{tag}$ is ill-conditioned, this is due to the limitation in the number of discretized tagging

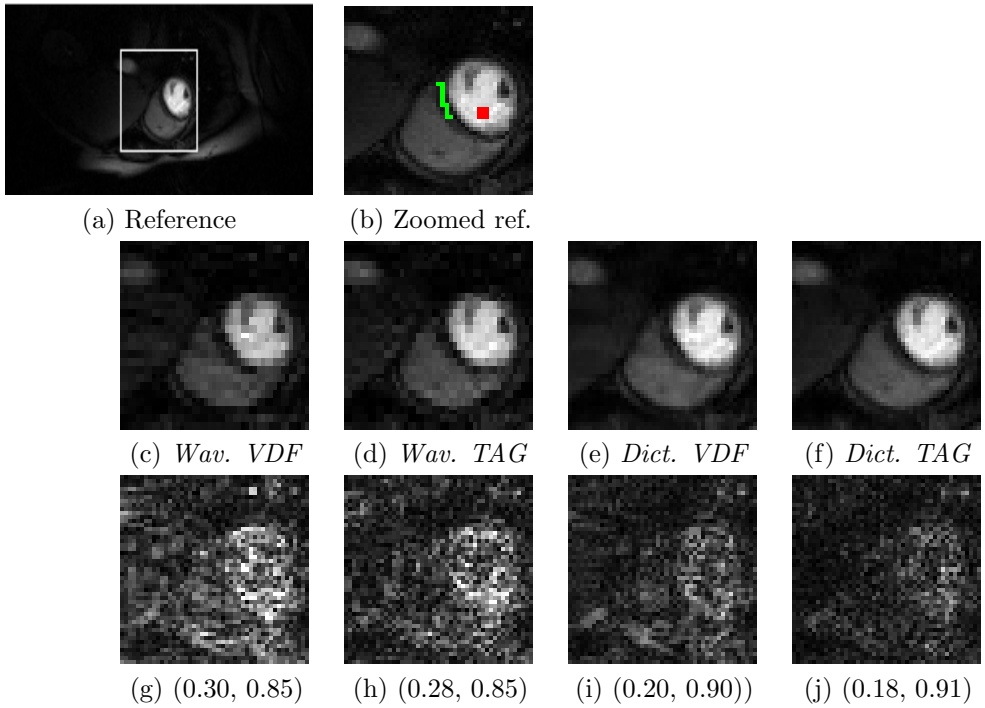

(a) Reference (b) Zoomed ref.

(c) *Wav. VDF* (d) *Wav. TAG* (e) *Dict. VDF* (f) *Dict. TAG*

(g) (0.30, 0.85) (h) (0.28, 0.85) (i) (0.20, 0.90)) (j) (0.18, 0.91)

Figure 3.9: Comparison of image recovery for four different MR image recovery techniques as described in section 3.4.1 at an acceleration factor of $R = 4$. (b) shows a zoomed-in region from the reference image (a). For all other columns, each column shows the zoomed-in recovered and error images for different techniques. Each technique is identified by the text below the recovered images and its performance is reported as pairs (EOF, SSIM) below the corresponding error image.

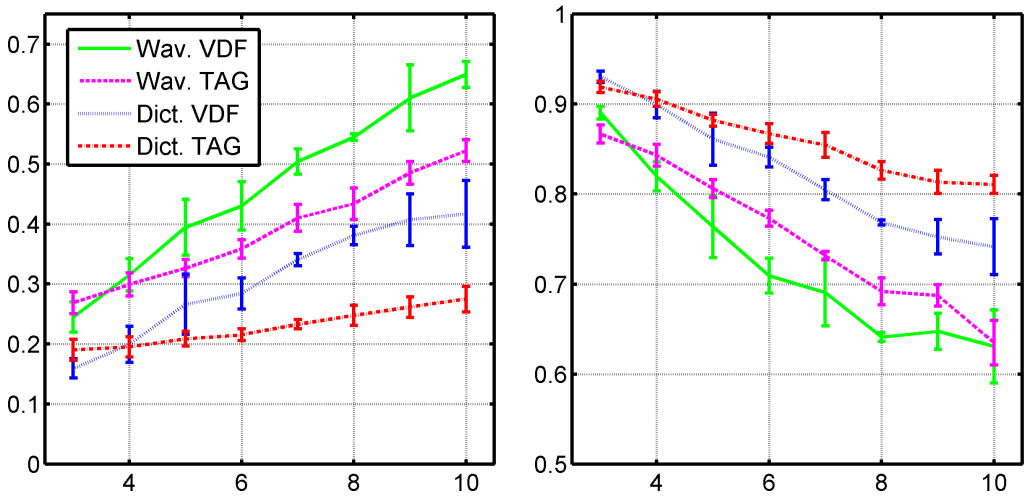

(a) *EOF vs. R* (b) *SSIM vs. R*

Figure 3.10: ($\mu \pm \sigma$) Relative error (EOF) vs. accelerations (R) curve for different MR image recovery methods on the in-vivo myocardial perfusion dataset.

profiles that can be generated. Consequently, the conditioning of the matrix $\mathbf{E}_{tag}$ improves with increasing acceleration factors. Thirdly, the proposed *Dict. TAG* technique outperforms all other techniques at high accelerations. This is due to the fact that each acquired sample in the *TAG* encoding formulation is a mixture of the standard k-space samples, which leads to a more uniform coverage of the k-space information than the *VDF* encoding scheme. Thus, the *TAG* sampling recovers the edges and fine-structures with higher accuracy than the *VDF* sampling at high accelerations. This observation is further emphasized in Fig. 3.11 which shows the recovered zoomed-regions (same from Fig. 3.9a) and the complete magnitude errors for images recovered using the *Dict. VDF* and the *Dict. TAG* methods at the high acceleration factor of $R = 8$. Figure. 3.11d shows the error image for the *Dict. TAG* method which

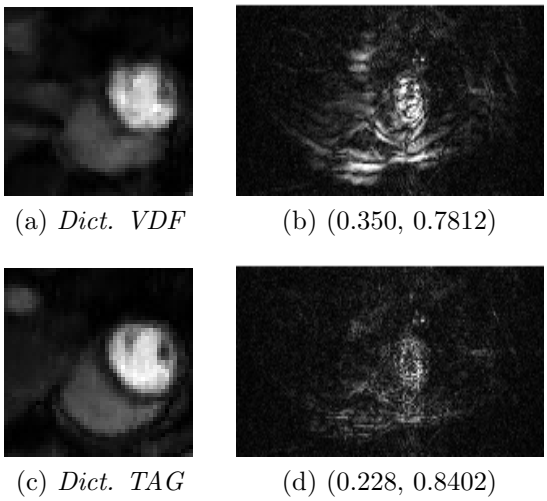

(a) *Dict. VDF* (b) (0.350, 0.7812)

(c) *Dict. TAG* (d) (0.228, 0.8402)

Figure 3.11: Zoomed-in recovered and complete error images for the *Dict. VDF* & *Dict. TAG* techniques at an acceleration factor of $R = 8$.

shows no aliasing artifacts as seen in *Dict. VDF* error image of Fig. 3.11b. In addition, the former shows non-negligible errors only in the vicinity of strong signal transitions.

First-pass myocardial perfusion MRI is used to detect and evaluate ischemic heart disease [42]. Regional perfusion defects can be detected by analyzing the signal variability in an image time-series. A high temporal and spatial resolution is required to accurately localize the defected tissue [42]. Thus, to assess the applicability of a fast technique for myocardial perfusion imaging, time series plots of averaged signal intensity in selected blood pool and myocardium regions are critically evaluated. Figures 3.12a and 3.12b compare the time-series plots of averaged signal intensity in selected blood pool and myocardium regions in reference images with that of the recovered

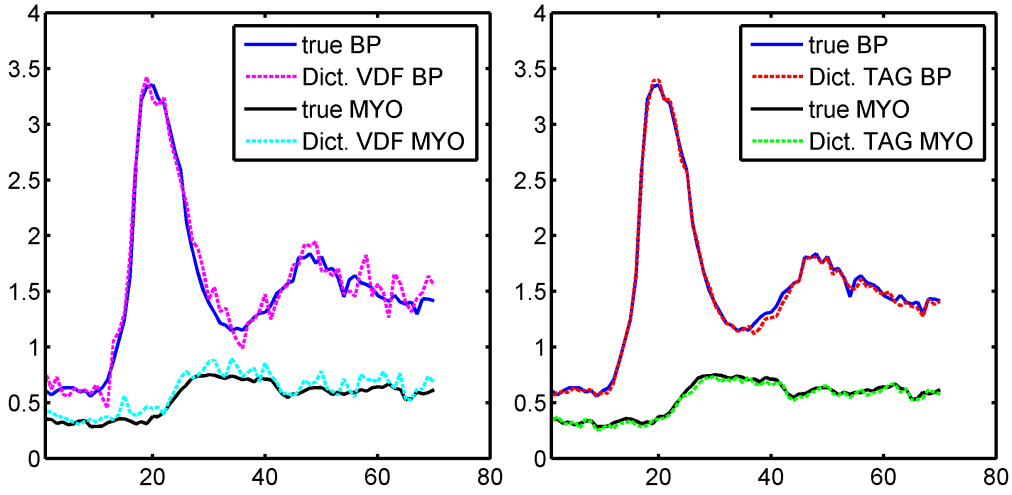

(a) *Dict. VDF* (b) *Dict. TAG*

Figure 3.12: Time-series plot of averaged signal intensity for recovered (at R = 6) and reference images for the in-vivo myocardial perfusion data.

images at acceleration $R = 6$ using the *Dict. VDF* and the *Dict. TAG* techniques, respectively. The selected blood pool (in red) and myocardium (in green) regions are shown in Figs. 3.9b. As expected, the time series curve for recovered images using the *Dict. TAG* scheme follows the reference curve more closely than the curve for the *Dict. VDF* sampling scheme.

3.4.5 Tumor Resection

Figure 3.13 shows the performance of the proposed tagging based signal encoding in real applications such as T1-weighted imaging for brain tumor resections. Figure. 3.13a shows a T1-weighted brain slice (real valued) from a brain tumor affected patient data set. The image is retrospectively under-sampled using the *VDF* and *TAG* sampling schemes and the error images for

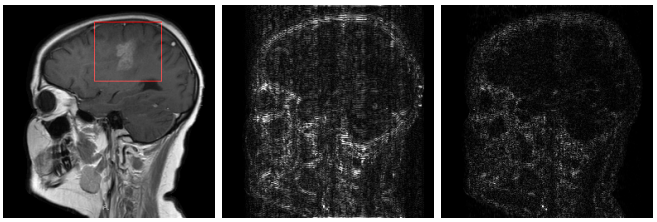

(a) Reference (b) *Dict. VDF* (c) *Dict. TAG*

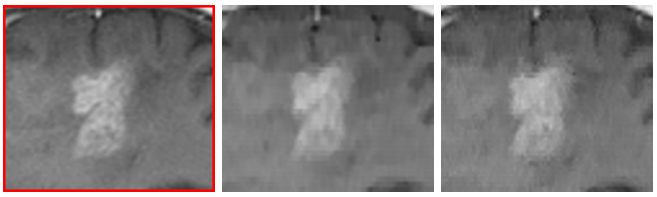

(d) zoomed (e) (19.6, 0.79, 0.11) (f) (23.6, 0.91, 0.07)

Figure 3.13: Comparison of the proposed tagging RF pulses based signal encoding formulation (TAG) with variable density Fourier undersampling (VDF) for the image-patch dictionary based sparse model at an acceleration $R = 3$.

the recovered images are shown in Figs. 3.13b and 3.13c, respectively. The *Dict. TAG* technique preserves the boundaries with higher fidelity than *Dict. VDF* allowing for resection margins closer to the real tumor boundary. Figs. 3.13d, 3.13e and 3.13f show the zoomed tumor region from the reference image, the *Dict. VDF* and the *Dict. TAG* recovered images, respectively.

3.5 Conclusions

In this chapter a novel MR signal encoding formulation using tagging radio frequency pulses is presented. The proposed formulation results in samples which are mixtures of k-space data, therefore even at high under-sampling the k-space is acquired more uniformly when compared with other variable

density schemes. The new encoding formulation is further combined with a dictionary learned for sparse representations of image-patches for MR images recovery from under-sampled data. A dictionary for image-patches is used to encode the redundancy in high-frequency content of the underlying dynamic images. The results of MR image recovery experiments using tagging based MR signal acquisition method on an in-vivo myocardial perfusion data set outperforms the equivalent dynamic MRI method implemented with variable density k-space under-sampling.

Chapter 4

Development, Tuning and Comparison of Spiral Variants for High Resolution FMRI

4.1 Introduction

Functional magnetic resonance imaging (fMRI) with high spatial resolution ($\leq$ 1.5-mm voxels) is useful and desirable for a variety of applications. For example, fine-scale functional features such as ocular-dominance columns can be resolved on the surface of cerebral cortex [22, 138], while other aspects of neural function can be resolved in the depth of cortex [100, 111]. In particular, high-resolution imaging is critical to quantify brainstem function because its various nuclei have small dimensions. Of particular interest is superior colliculus (SC), a laminar structure, with three millimeter-scale subdivisions: superficial layers that receive direct retinal inputs, intermediate layers associated with visual attention and oculomotor responses, and deep layers that play a role in multi-sensory integration [136]. The superficial visual layers are organized retinotopically [27, 70, 71, 114], and thus are an ideal subject to study high-resolution brainstem imaging because their organization permits delineation of small ($\sim$3 mm) retinotopically specific regions-of-interest (ROIs).

Functional imaging in brainstem is challenging compared to cerebral

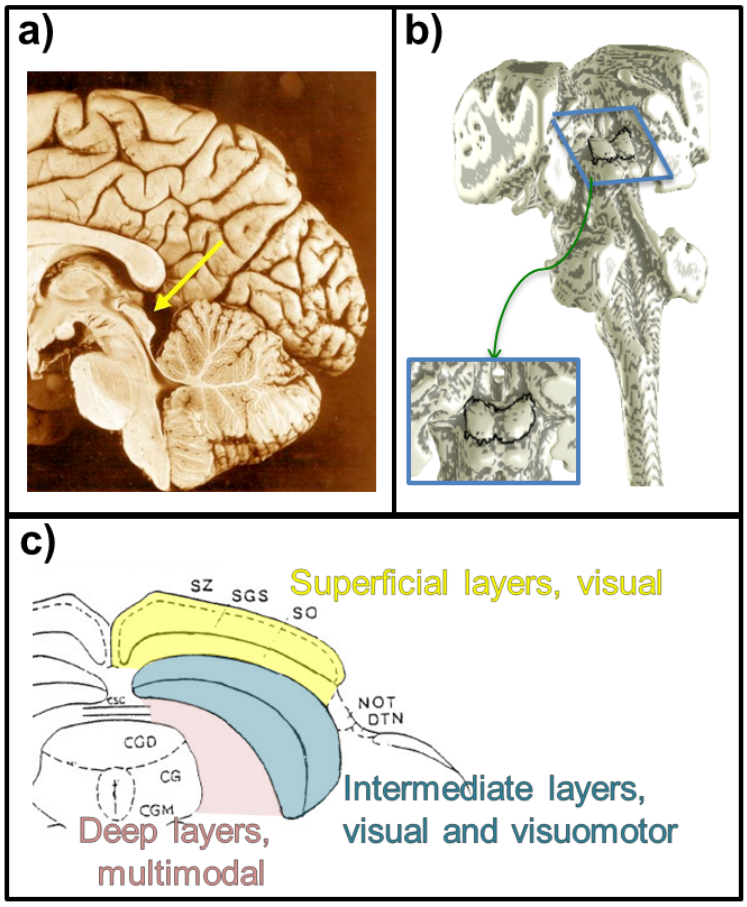

Figure 4.1: Anatomy of the superiror colliculus (SC). a) SC is located on the dorsal surface of the brainstem (pointed by the yellow-arrow), b) A 3D surface of brainstem with SC marked in black-ouline, c) Laminar structure of SC in primates.

cortex because signal levels are low while noise levels are high. Signals are reduced in brainstem mostly because of its deep location. Functional contrast levels are also relatively low, even for the strongest visual stimuli. At the same time, noise levels can be higher in brainstem, because it is adjacent to large vascular structures that supply and drain blood from the brain. Therefore, physiological nuisance artifacts are particularly pronounced in superficial brainstem structures such as SC. Thus, SC offers the challenge of obtaining high spatial resolution despite particularly low contrast-to-noise ratio (CNR).

Echo Planar Imaging (EPI) and spiral are the two most commonly used trajectories for fMRI acquisitions. An EPI trajectory covers k-space in a raster fashion, and in doing so it uses the underlying gradient systems inefficiently. The need for continual polarity reversals in gradient amplitude generally do not permit operation at full power; instead the trajectories are slew-rate limited [45]. Spiral trajectories use the gradient system more efficiently through equal energy deposition in two gradient directions and by avoiding the corners of k-space [10, 25, 45]. Spiral trajectories therefore have relatively shorter readout durations than EPI trajectories. However, independent of the trajectory, to obtain satisfactory SNR high-resolution fMRI requires long readout durations compared to the T_2^* signal decay in gray matter. For this reason, multi-shot acquisitions are necessary; however they are susceptible to motion based inter-shot off-resonance errors. Multi-shot spiral acquisition is amenable to self-navigation schemes, reducing some of the shot-to-shot errors. Also, the trajectory oversamples low spatial frequencies, which renders head motion as

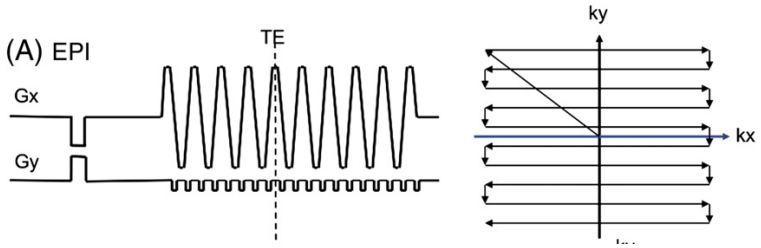

(a) Echo planar imaging (EPI)

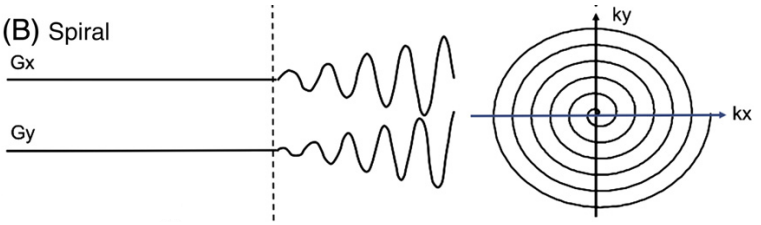

(b) Spiral

Figure 4.2: Gradient waveforms and k-space trajectory for (a) Echo planar imaging (EPI) and, (b) Spiral.

blurring in recovered images as opposed to ghosting in EPI, thereby making spiral acquisitions relatively more robust to motion than EPI [25, 45].

The spiral trajectory is asymmetric with respect to the echo time, and the most commonly used variant starts at the origin and moves outwards, which we will term spiral *out*. The alternative variant that starts from k-space periphery and moves inwards will be termed spiral *in*. The spiral-in variant improves upon the acquisition (TR) efficiency of spiral out, while acquiring a comparably similar T_2^* weighted image [13]. In addition, spiral in exhibits lower signal dropout than spiral out for regions compromised by macroscopic susceptibility field gradients (SFGs) near air-tissue interfaces [47, 105]. However, in homogeneous regions, spiral in shows lower sensitivity to the Blood

Oxygen Level Dependent (BOLD) signal than the out-variant [48, 105]. The reduced BOLD sensitivity of spiral-in was attributed to the different contrast weighting obtained in the region-of-interest due to T_2^* relaxation [105]. Spiral variants also include dual-echo trajectories that traverse k-space twice after each excitation. Combination of single-echo out- and in-variants results in four dual-echo variants. Among them the in-out variant is the most widely studied and previously shown to: 1) reduce the signal dropouts in regions compromised by SFGs and, 2) increase image signal-to-noise ratio (SNR) in homogeneous regions resulting in increased BOLD activation volumes [47, 48, 105]. More recently, the in-in variant was found to be superior to in-out variant in terms of recovering BOLD activation in regions affected by SFGs. However, in this study, the in-out images were created by combining individual echo images from in-in and out-out variants [82]. In the same study the out-out variant was shown to yield images with the highest image SNR among all spiral variants [82].

In this chapter, I evaluate the use of dual-echo spiral variants for high-resolution functional imaging. High-resolution imaging is affected by various noise sources such as increased thermal noise due to small voxels and higher off-resonance errors due to multi-shot acquisitions and longer readout durations. The noise is more pronounced for smaller functional units such as SC which are close to large blood vessels and cerebral spinal fluid (CSF) and show more T_2^* inhomogeneity than cortex. The increased noise in high-resolution imaging reduces BOLD sensitivity of fMRI acquisitions. Acquisition of two echoes using

dual-echo variants should reduce noise, make the acquisition more robust to T_2^* heterogeneity, and thereby improve the BOLD sensitivity of high-resolution fMRI. Due to an inadequate knowledge of fMRI noise processes, particularly at high resolutions, it is difficult to extrapolate the results of previous low-resolution studies to the high-resolution regime. Moreover, previous studies focused on signal recovery in regions affected by SFGs, and therefore measured BOLD sensitivity using activation volumes. This measure is not satisfactory to assess the performance of high-resolution imaging applications.

The chapter compares BOLD sensitivity in human superior colliculus obtained at high resolution using various spiral variants (single- and dual-echo) and the commonly used EPI trajectory. Similar to previous studies, image SNR values are calculated and reported. This extends the results of previous studies from low-resolution to high-resolution regime. Moreover, unlike previous studies, the BOLD sensitivity is characterized through activation signal and noise amplitudes within functionally and anatomically defined ROIs. For reference BOLD sensitivity is also evaluated in early visual cortex (EVC), which has been extensively studied and well characterized in the past. It is relatively large is size and does not require high spatial resolution when evaluated on the scale of visual areas (e.g., V1, V2).

This chapter is further organized as follows. Section 4.2 details the development efforts for the dual echo spiral sequences and the off-resonance correction schemes used. Section 4.3 presents the acquisition protocols and stimulus used for acquiring the functional data on healthy volunteers. This

section also summarizes the fMRI analysis methods used to convert acquire raw data into BOLD CNR values. Section 4.4 presents the results of our high resolution study. In section 4.5 we present a detailed characterization of results and compare with those of previous studies. Finally, section 4.6 concludes the chapter.

4.2 Pulse Sequence Development

Spiral imaging sequences mostly rely on Archimedean spirals, i.e., spiral trajectories with equidistant revolutions. An Archimedean spiral (single-shot) can be parametrized by $k(t) = \lambda\ \theta(t)\ e^{i\theta(t)}$, where, $\theta(t)$ represents a monotonically increasing function, $k(t) = k_x(t) + i\ k_y(t)$ is the k-space trajectory, and $\lambda = \mathrm{FOV}^{-1}$ is the distance chosen between the neighboring revolutions to satisfy the Nyquist sampling theorem. The trajectory $k(t)$ is given by the time integral of the gradient waveform $\mathbf{G}(t)$. Therefore, the required gradients for a spiral trajectory can be calculated by $\mathbf{G}(t) = \frac{\lambda}{\gamma}\ \dot{\theta}(t)\ [1 + i\theta(t)]\ e^{i\theta(t)}$, where, $\dot{\theta} \equiv d\theta/dt$ and γ is the gyromagnetic ratio. The function $\theta(t)$ represents the sampling points on the spiral trajectory. Finding an exact $\theta(t)$ requires formulating the above problem as a differential equation with suitable boundary conditions on maximum gradient amplitude and slew-rate [44, 74]. An analytical solution for determining $\theta(t)$ has not been found [10, 44]. However, a simple analytical approximation to the differential equation has been presented by Glover [44] and shown to adequately reproduce the exact solution. The approach first operates the gradients at their maximum rate of change

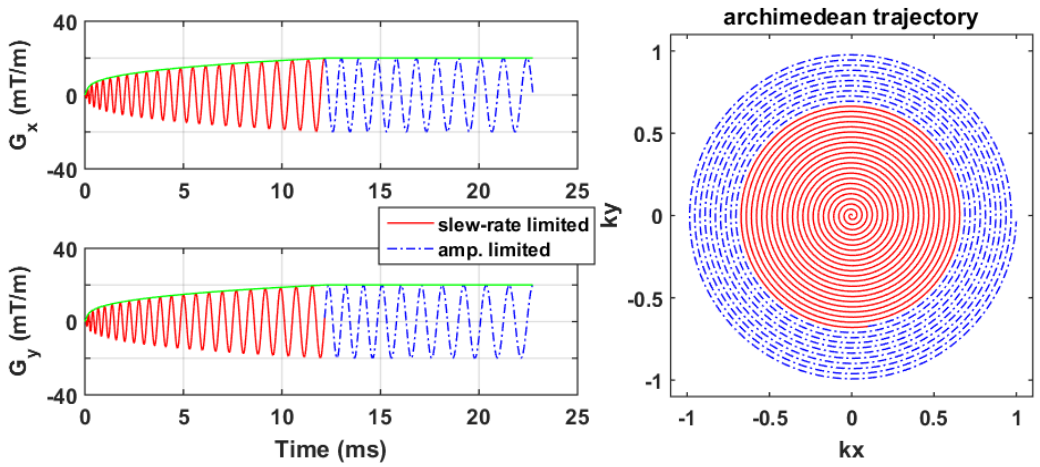

(a) Gradients (b) k-Space trajectory

Figure 4.3: Gradient waveforms and k-space trajectory for an Archimedean spiral out trajectory.

(slew-rate limited), until maximum gradient amplitude is reached as shown in fig. 4.3. The trajectory is completed by a brief gradient lobe that returns to the k-space origin.

4.2.1 Dual Echo Spiral Variants

Dual echo spiral variants are obtained by concatenating the gradient waveform of single-echo out-trajectory either with itself (out-out variant) or its reversed waveform (for in-out and in-in variants). Figure 4.4 shows the designed dual-echo gradient waveforms for the variants: in-in, in-out and out-out. Reconstructed images for individual echoes are also shown. Image reconstruction was done by gridding with a Kaiser-Bessel kernel using 2:1 oversampling. In figs 4.4d, 4.4e and 4.4g there is relatively less signal drop-out near the sinus

cavities as opposed to that in figs. 4.4f, 4.4h and 4.4i. This demonstrates the higher sensitivity of inward echoes over that of outward echoes in acquiring signal in regions affected susceptibility induced field gradients. This observation is consistent with various studies [47, 48, 82, 105]. Also, the T_2^* contrast for the individual in and out echoes for the in-out variant differs despite having the same echo time ($\approx$ 42ms). This is due to the fact that in the two echoes their higher k-space frequencies have a different T_2^* relaxation weighting [105].

4.2.2 Self-Navigation Correction

For multi-shot spiral acquisitions, motion leads to inter-shot phase inconsistencies that result in off-resonance distortions and thus reduce the advantages of multi-shot acquisitions. Motion results in phase variation between shots at the k-space origin which is partially compensated using a zeroth-order correction [46]. Figure 4.5 shows the effect of self navigation correction on a brain image acquired using a 3-shot spiral-out trajectory on a healthy volunteer.

4.2.3 Field Inhomogeneity Correction

Field map inhomogeneity arises due to: 1) the main-B0 field inhomogeneity and, 2) the susceptibility induced field gradients. To correct for field inhomogeneity based off-resonance effects a local field map was calculated using two images that are acquired at slightly offset echo times. The phase

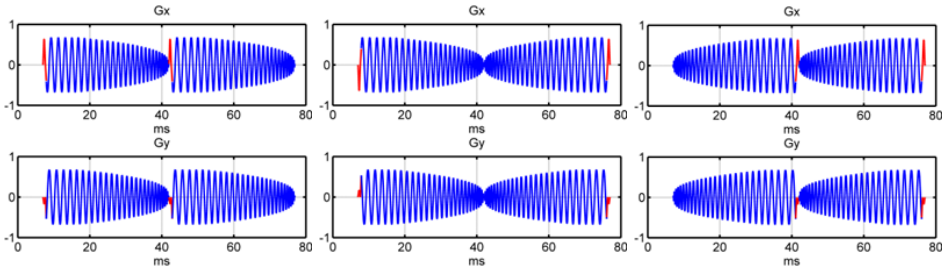

(a) In-in (b) In-out (c) Out-out

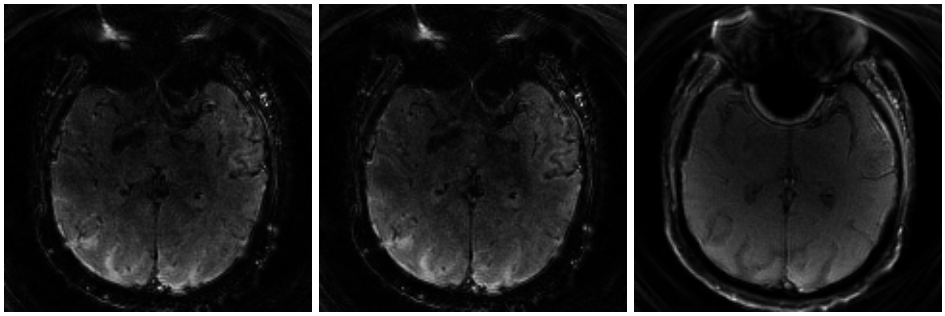

(d) In (42ms) (e) In (42ms) (f) Out (7ms)

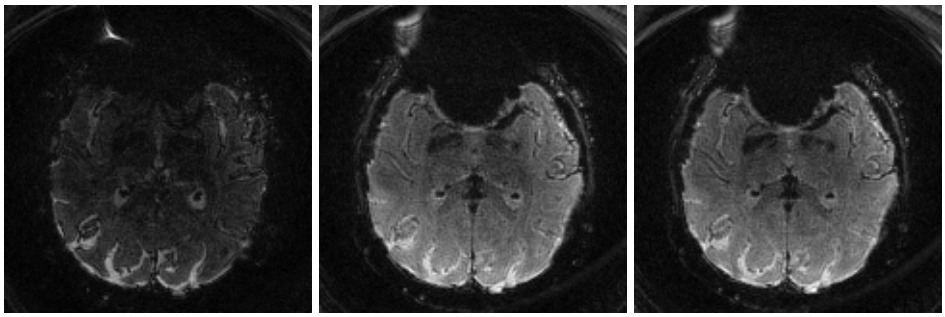

(g) In (77ms) (h) Out (42ms) (i) Out (42ms)

Figure 4.4: Gradient waveforms and images for individual echoes for the dual echo spiral variants: in-in, in-out and out-out. Echo time for each echo is specified in the caption below each image.

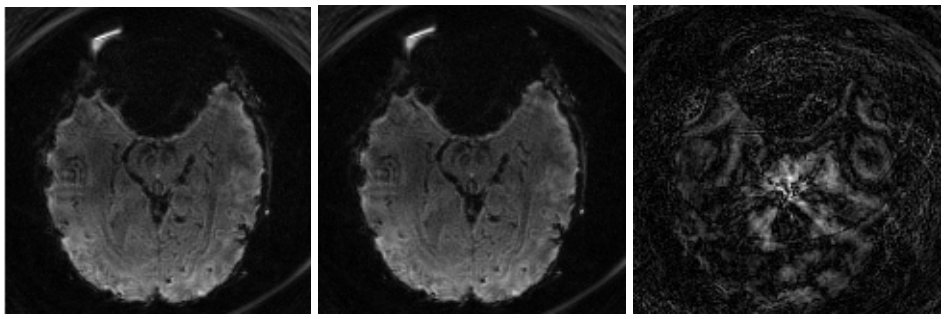

(a) Reference (b) SNC corrected (c) Correction

Figure 4.5: Self navigation correction on a brain image acquired using a 3-shot spiral out trajectory with a field-of-view=192mm at an isometric resolution of 1.2mm. In (c) the grayscale colormap is mapped from zero to 6.1% of the highest intensity in (a).

difference accrued between the two images is assumed to be a direct effect of underlying field inhomogeneity. The echo offset, the ΔTE, is kept small to avoid 2π phase wraps between the two images. The acquired field map is then approximated using a first-order model estimated using a maximum-likelihood formulation [57, 61]. The estimation problem is a weighted least-squares minimization problem, where weights are simply the magnitude of the image voxels. Voxel magnitude based weights ensure that weaker field map data does not heavily influence the estimation of the linear parameters. Once the acquired field map has been approximated, the corresponding linear correction is applied in the gridding image reconstruction.

Figure 4.6 shows the complete process of field map correction on a phantom image. Figure 4.6b shows the acquired field map which when approximated by a linear map shows a variation of 0.6772 Hz/cm and 0.8496 Hz/cm in the x- and y-axis, respectively. Figure 4.6c shows the original and

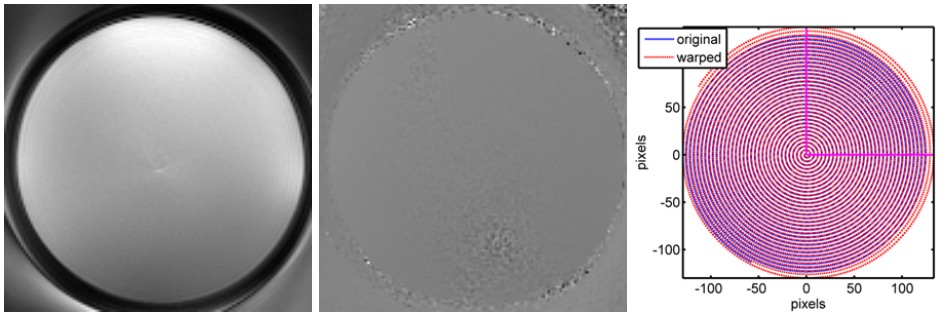

(a) Reference (b) Estimated Field (c) Warped Trajectories

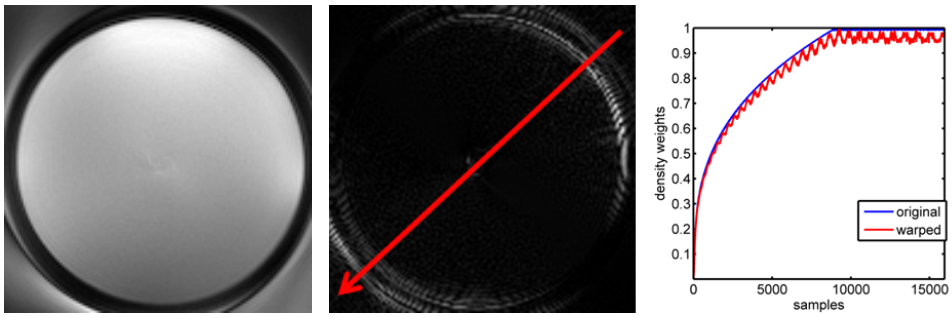

(d) Corrected (e) Correction (f) Density Curves

Figure 4.6: B0 field inhomogeneity estimation and distortion correction on a phantom. (a) Reference, (b) Estimated B0 field inhomogeneity, (c) Designed and warped k-space trajectory for a linear field map approximation, corresponding density curves are shown in (f), (d) Distortion corrected image and, (e) Estimated field map distortion.

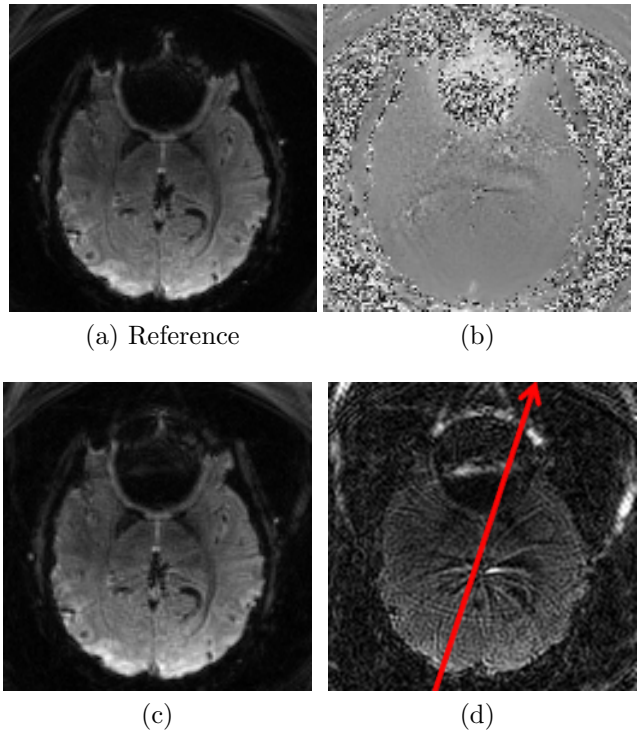

(a) Reference (b)

(c) (d)

Figure 4.7: B0 field inhomogeneity estimation and distortion correction on a brain image. (a) Reference, (b) Estimated B0 field inhomogeneity, (c) Distortion corrected image and, (d) Estimated field map distortion.

the warped trajectory corresponding to a rotation of $\approx 51^{\circ}$ in the spiral trajectory. Figure 4.6d shows the distortion corrected image obtained by gridding the trajectory data for the warped trajectory using adjusted density compensation shown in fig. 4.6f. The correction is shown in fig. 4.6e which shows strong improvement in edges as the blurring is reduced. Results for field map correction for a brain image are shown in fig. 4.7.

4.3 Functional Imaging

Imaging was performed on 3T scanners (Siemens Skyra and Trios) using the product 32-channel head coil. Figure 4.8a shows an example prescription and a functional image from a single-echo spiral-out acquisition. In this prescription, twelve 1.2-mm-thick quasi-axial slices were oriented roughly perpendicular to the local neuraxis to cover the entire SC with a 192-mm field-of-view (FOV). This prescription also samples a portion of early visual cortex. For the spiral sequence variants (single-echo: out, in; dual-echo: in-in, in-out and out-out), we chose TR = 1 sec, so with three shots, a volume was acquired every 3 seconds. Maximum gradient of 24 mT/m and maximum slew rate of 150 T/m/s resulted in T_{acq} = 35ms at acquisition bandwidth 200 kHz/pixel. In analogy; we used 3x GRAPPA acceleration to obtain the same resolution using the EPI sequence [37, 79, 96] with a somewhat smaller FOV of 154mm. An echo spacing of 1.30 milliseconds was used, which resulted in T_{acq} = 49 ms. To avoid fold-over effects due to small FOV, a saturation band was prescribed over the anterior portion of the head. The resulting set of images was then temporally rebinned to 3-sec sampling to improve SNR and allow direct comparison with the spiral data. A set of T1-weighted structural images was obtained on a prescription co-aligned with the above structural images at the end of each scan session using a 3D FLASH sequence (15° flip angle, 0.78-mm pixels, minimum TE and TR). These images were used to align the functional data to the segmented structural reference volume (see below).

For spiral dual-echo variants, a single image is obtained by combin-

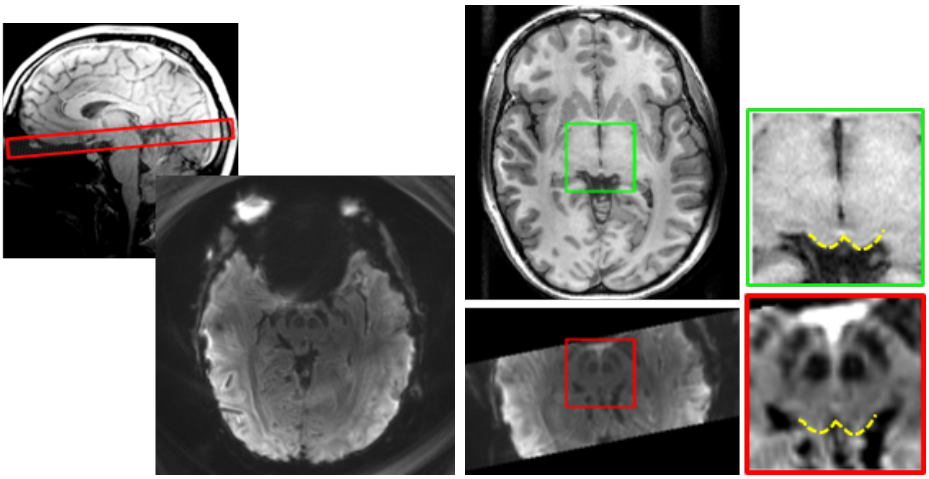

(a) (b)

Figure 4.8: (a) Typical prescription and acquired functional image. (b) Axial slice from structural reference volume (left-top), corresponding transformed functional data (left-bottom). Enlargements on right show SC superficial surface (yellow) obtained from structural volume (green inset), and its close correspondence to contrast boundaries in the functional image (red inset).

ing the individual echo images using three combination schemes: 1) signal-weighted (Sig-wt), 2) contrast-to-temporal-noise-ratio-weighted (CTNR-wt) and, 3) contrast-sum (C-sum). For Sig-wt and CTNR-wt schemes, for each voxel a combined time-series is calculated as a weighted-average of individual echo time-series. In the Sig-wt, scheme the weights are linearly proportional to the time-series mean signal of each echo. In CTNR-wt scheme, the weights are calculated using the BOLD amplitude (see 4.3.1) and calculated time-series noise; Sig-wt and CTNR-wt schemes have been used in previous studies [82, 105]. The C-sum scheme simply adds the time-series of both echoes after each time-series has been corrected for second-order temporal trends and mean-subtracted. (Note: the CTNR-wt scheme was originally identified in [82, 105] as CNR-wt, however in this chapter CNR is specifically loosely to refer to BOLD CNR. For greater precision, we use the more detailed abbreviation CTNR-wt.) Image SNR was evaluated voxel-wise using the method described in [78], in which the noise was estimated from the difference image between two consecutive time frames. Noise measured this way includes image-to-image fluctuations, and can also eliminate the effect of potential aliasing artifacts outside the brain [78]. The SNR values reported in this chapter are average values over multiple subjects and over voxels within selected ROIs inside the brain; our methods are consistent with previous study [82].

Structural imaging

In a separate session for each subject, we acquired a structural reference volume with good gray-white contrast using a MP-RAGE sequence (TI = 950 ms, 9° flip angle, isometric voxel size of 0.7 mm, two averages, $\sim$ 25-min duration). The anatomical images collected in each functional scan session were used to align the functional data to this structural 3D reference volume. Figure 4.8b (right-top) shows a structural axial-plane and the corresponding transformed functional data (right-bottom) acquired using a spiral-out trajectory. The insets (in fig. 4.8b) show enlargements from the structural and functional data; yellow dashed lines show boundaries of SC tissue evident in the T1-weighted image and at corresponding locations contrast boundaries are visible in the functional images. The results confirm the effective spatial localization of the spiral imaging for both outward and inward trajectories, with similar results for EPI.

From structural volume we segmented the tissue of the midbrain, brainstem, and portions of the thalamus using a combination of automatic and manual methods provided by the ITK-SNAP application [142]. The CSF-tissue interface of the brainstem was interpolated from the segmentation using isodensity surface tesselation, and this initial surface was refined to reduce aliasing artifacts using a volume-preserving deformable-surface algorithm (Fig. 4.10b) [137]. In cortex, the FreeSurfer software suite was used to initially segment the white matter and gray matter at 1-mm sampling [24]. These segmentations were then upsampled to 0.7-mm and adjusted manually to correct errors

and obtain full resolution. At the adjusted gray-white interface, a smooth surface was obtained using the same methods used for brainstem. These 3D-surfaces provide a means to visualize the functional data and allow for its depth-averaging to increase SNR (see below).

Stimulus

Stimuli were generated using Matlab (MathWorks Inc., Natick, Massachusetts) running PsychToolbox-3 [12] on a Macintosh Pro computer. Figure 4.9 shows an alternating lateralized hemifield stimulation and attention protocol used to maximize the functional response in the SC and the visual cortex. A 144° wedge of moving dots (mean speed 4°/s) alternated 9.5 times between the left and right visual fields with a 24-s period. The wedge on each side was divided into 2×4 virtual sectors and task of the subjects was to discriminate if the dots in one of the sectors were moving faster or slower than dots in other sectors. During fMRI scanning sessions, subjects maintained fixation and performed the speed-discrimination task over the course of many 228-second-duration runs.

4.3.1 FMRI analysis

Analysis of the fMRI data was done using the mrVista software package (available for download at white.stanford.edu) as well as tools developed upon the mrVista framework in our lab. We estimated in-scan motion using a robust scheme [98] applied to a temporally smoothed (5-frame boxcar) version of the

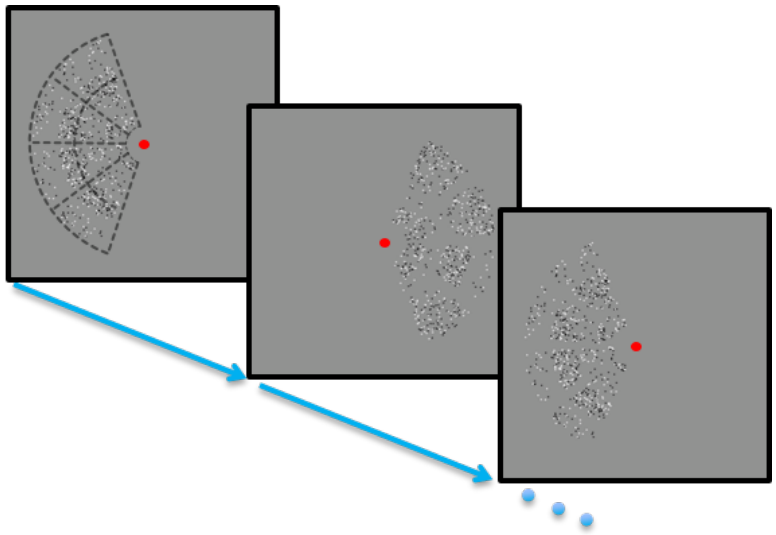

Figure 4.9: Lateralized hemifield moving dot stimulus. Subjects performed a speed-discrimination task among virtual sectors shown as dotted outlines in first image. Stimulus alternated from left to right hemifield with a 24-s period.

fMRI time-series data. Between-run motion was corrected using the same intensity-based scheme, this time applied to the temporally averaged intensity of the entire run. The last run of the session was used as the reference. After motion correction, the many runs recorded during each session were averaged together to improve SNR. The intensity of the averaged data were spatially normalized to reduce the effects of coil inhomogeneity. The normalization used a homomorphic method, that is, dividing by a low-pass filtered version of the temporally averaged volume image intensities with an additive robust correction for estimated noise.

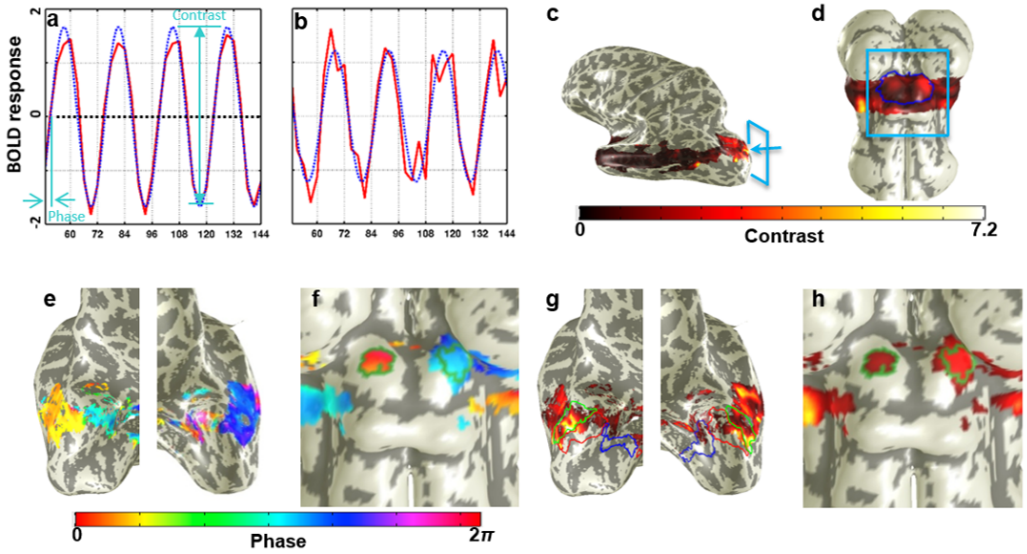

Figure 4.10: Examples of sinusoidal fits to time series in a) visual cortex, and b) SC. Contrast is defined as the peak-to-peak amplitude of the fit, while phase measures the time delay between the onset of the response in the right visual hemifield with the hemodynamic response. BOLD contrast maps on (c) partially inflated left-hemisphere, and (d) brainstem with SC outlined (dark-blue). Thresholded (coherence >0.4) phase maps on (e) cortex, and (f) brainstem. Thresholded contrast maps on (g) left and right hemispheres with visual areas outlined (V1 green; V2 red; V3 blue), and (h) brainstem (ROI marked in green).

Depth averaging

In SC, a Euclidean nearest-neighbor distance map was calculated between tissue voxels and the vertices of the SC surface. In cortex, we used a morphing scheme to calculate a self-consistent depth coordinate system normalized to local gray-matter thickness [73]. Functional data were then aligned and re-sampled to the reference volume ([98]. Thus, each volume voxel was now associated with a functional time-series and a depth coordinate. We used the coordinates to average the data through particular depth ranges of the SC or cortex. In SC, averaging was performed on the range of $0.6 - 1.8$ mm to avoid contamination with superficial vascular tissue and CSF. In cortex, averaging was limited to the central half of the gray-matter thickness to avoid contamination with both white matter and the superficial highly vascular tissue above the pial surface.

BOLD contrast

A sinusoid at the stimulus repetition frequency was then fit to the normalized time series at each voxel, and from this fit we derived volume maps of response amplitude, coherence, and phase. The amplitude quantifies the functional contrast, contrast $= 2 \times$ amplitude, while the phase measures the time lag between stimulus onset in the left hemifield and the hemodynamic response (Fig. 4.10a and b). The coherence value is equivalent to the correlation coefficient of the time-series data with its best-fit sinusoid. Figure 4.10 shows BOLD contrast and phase maps for a spiral-out reference session. The maps

are transformed onto 3D surfaces, with Figs. 4.10c, e, and g corresponding to cortex, figs. 4.10, and Figs. 4.10d, f, and h corresponding to brainstem. Maps in 4.10e-h are thresholded at coherence > 0.4.

BOLD Noise

FMRI noise has a non-Gaussian distribution. To estimate fMRI noise, bootstrapping, a non-parametric statistical analysis method [32–34], was used to estimate confidence intervals on the functional contrast obtained in each session. Each experimental condition in our measurements included at least seven runs. This set of runs were resampled with replacement, and the resampled set was then averaged and analyzed as above to obtain the functional contrast. This process was repeated 10000 times to generate an estimate of the statistical distribution of the contrast. The 68% confidence intervals were calculated from this distribution, and BOLD noise amplitude was defined as half the difference between the upper and lower interval. For a normal noise distribution, this calculation would precisely correspond to the standard-error-of-the-mean.

4.3.2 Region-of-interest generation

In SC, ROIs were obtained in each subject using our standard functional imaging protocol, single-echo spiral out with TE = 40 ms, which was shown to be very effective in generating retinotopic maps of the visual field [69, 71]. These "reference sessions" consisted of 12 runs of the lateralized moving-dot

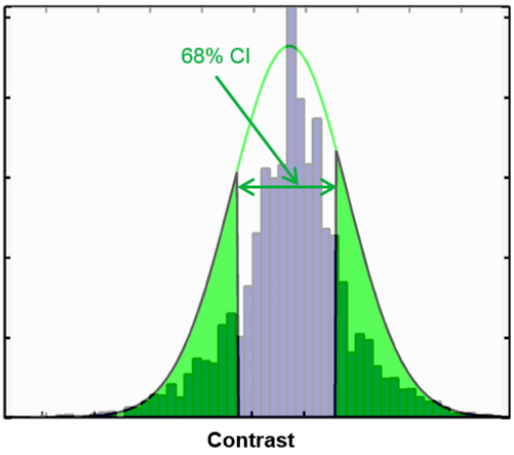

Figure 4.11: Computation of BOLD noise within an ROI. Bootstrapping (blue-bars) is used to estimate a distribution (green-curve) for BOLD amplitudes within the ROI. BOLD noise is defined as the 68% confidence interval length.

stimulus protocol described above. The sinusoidal fitting procedure was then applied to depth-averaged mean data to obtain a map of coherence upon each SC. We manually chose the point of maximum coherence upon rostral SC, which contains the retinotopic representation of the stimulus aperture, and expanded this region in a fashion that maximized the mean coherence of a contiguous region of SC with area $6 - 8$ mm^2 around this point; this area was chosen based on the expected retinotopic distribution of the stimulus representation. SC ROIs delineated using this process for a subject are overlaid atop the coherence amplitude and phase maps in Figs. 4.10f & 4.10h, respectively. In visual cortex, we defined ROIs from the baseline session by choosing the top 50% of coherence for depth-averaged data within visual areas V1–3. Visual areas were defined for each subject in separate fMRI sessions using a tomographic PRF method [51]. Figure 4.10c-d shows visual areas V1–3 in the

left and right hemispheres, respectively.

4.3.3 Data Acquisition

Tuning Data

We tuned each trajectory to find the optimal echo time at which it yielded the highest BOLD CNR. To tune each variant, functional data was acquired on a single subject over a broad range of echo times. Data was analyzed and CNR is calculated in a selected ROI. A parabola was fitted to the CNR for various echo times and the peak of the parabola was used to estimate the optimal TE for the selected trajectory. For each variant a subject was selected from a pool of 3 healthy volunteers. For each echo time, 6 functional runs of ~ 4 min. duration each were acquired. Data acquisition for all echo times for a variant are distributed over two acquisition sessions with $2-3$ different echo times per session. This resulted in tuning sessions of $12-18$ functional runs of duration $70-90$ minutes.

Comparison Data

Functional data was acquired on five healthy volunteers (age $25-55$ years, mean 35 ± 12 years; one female) for spiral variants: in, in-in, in-out and out-out, and for EPI. Single-echo spiral-out was used as a reference trajectory. In each comparison session, seven runs each were acquired for spiral-out and for one of the five aforementioned trajectories. To account for day-to-day variability 2 comparison session were acquired per subject per trajectory. Thus, a

total of 10 comparison sessions were acquired per trajectory.

4.4 Results

4.4.1 Image Signal-to-Noise Ratio

Previous studies used image SNR as a metric for comparing the performance of the sequence variants. To establish a point of comparison of our results to these studies, we measured SNR for each of our dual-echo trajectories. Figure 4.12 compares SNR values obtained in EVC and SC in our studies to those obtained by a previous study [82]. In [82] 12 healthy volunteers performed a complex finger tapping task and whole-brain fMRI scans were acquired on a 1.5 T scanner using 3.8-mm isometric voxels for a ROI defined in motor cortex, and imaging data was acquired for in-in and out-out spiral variants. The in-out data was then constructed using the first and second echoes from in-in and out-out variants, respectively. In comparison, our results are acquired using 1.2-mm isometric voxels on a 3T scanner by direct acquisition of all three variants.

A comparison of relative trends extends the results of the previous study into a high-resolution regime. The challenge of high resolution is clearly evident. For the single echoes, SNR is about two-fold lower in cortex at high resolution, and drops by another factor of two in SC. When the two echo images are simply averaged, for both low and high resolution, SNR increases in the order: in-in, in-out and out-out in cortex. However, there is no longer a significant difference between the in-in and in-out pairs. In SC, there is again

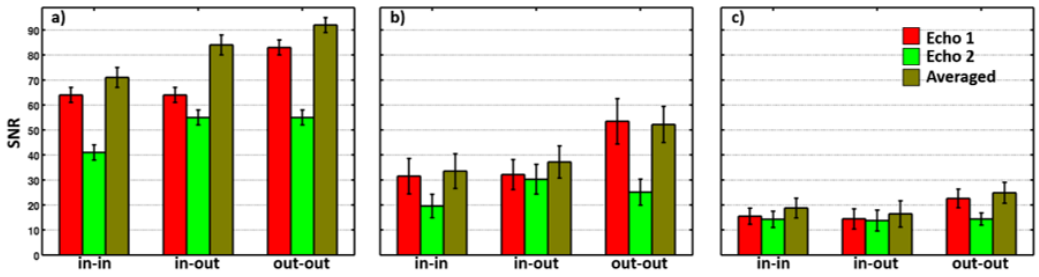

Figure 4.12: Comparison of mean image SNR values for low and high resolution fMRI acquisitions. a) From a previous low resolution study (3.8 mm isometric voxels) [82]: within an ROI defined in motor cortex for a finger tapping task. From our high resolution study (1.2 mm isometric voxels) which uses a moving dot speed discrimination task: b) visual cortex and, c) superior colliculus. Data in [82] is averaged over 12 sessions and in our study its averaged over 10 sessions.

no difference in SNR between in-in and in-out, but out-out is clearly stronger.

Temporal SNR values for EPI and the single-echo spiral reference were obtained across the many sessions. In EVC, we observed mean SNRs of 27.3±5.3 for EPI as compared to 36.9±5.3 for the reference. In SC, we observed 11.3±1.4 for EPI as compared to 19.1±2.5 for the reference. Thus, EPI appears to provide a significantly lower temporal SNR than the single-echo spiral reference trajectory ($p < 0.0004$).

4.4.2 Echo Time Tuning

As expected, CNR varied with echo time in EVC (Fig. 4.13). Because T_2^* was similar in both SC and EVC ROIs, we chose to perform our echo-time tuning using the EVC data because of its much higher CNR. Parabolic fits to the data provided estimates of optimal echo time for each trajectory (Table 4.1). The fitting process was effective for most of the variants, but spiral

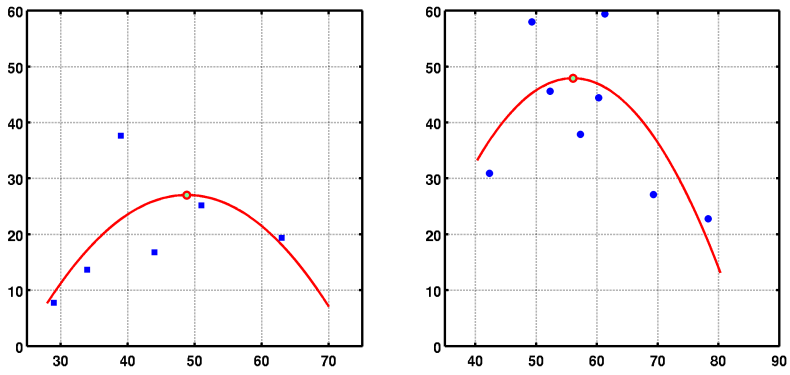

(a) EPI

(b) In

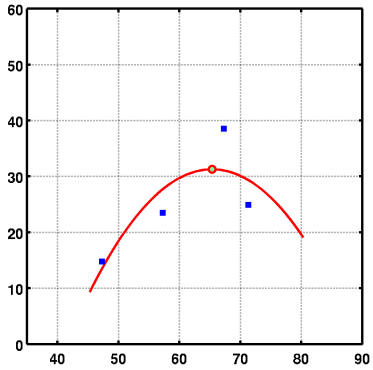

(c) In-in

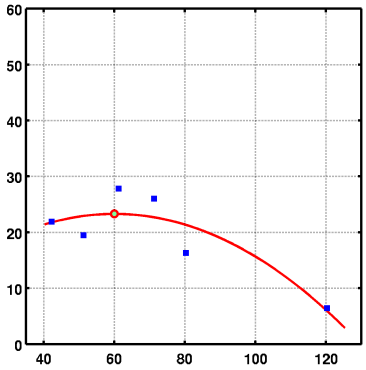

(d) In-out

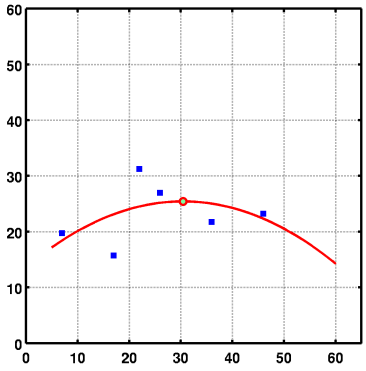

(e) Out-out

Figure 4.13: Echo time (TE) tuning for various trajectories in cortex for high-resolution fMRI. The peak of parabolic fits to BOLD CNR values over multiple echo times is selected as the optimal TE.

Table 4.1: Tuned echo times (TE) for various trajectories based on data analysis presented in fig. 4.13

Trajectory	Optimal TE (in ms)	R^2
EPI2d	48	0.39
In	56	0.54
In-In	65	0.67
In-Out	60	0.77
Out-Out	30	0.22

out-out did not exhibit a clear maximum.

4.4.3 Dual Echo Combination Schemes

Figures 4.14a & b show mean contrast and noise for dual-echo spiral variants in EVC and SC, respectively. Data is shown for the individual echoes, the combined echoes and the single-echo spiral-out reference acquisition for comparison. In EVC, BOLD contrast is strong, $\sim 4\times$ stronger than in SC. In EVC, all dual-echo variants show higher contrast for the second echo than the first. In SC, the same pattern is evident for spiral out-out, but the first echo is stronger than the second echo for both in-in and in-out. For all variants, the second echo is consistently noisier than the first echo.

Contrast and noise are affected differently when the individual echoes are combined by the three methods. For the signal-weighted (Sig-wt) combination, contrast and noise roughly follow the echo that exhibits the higher mean image intensity. This is clearest for the in-in and out-out variants for

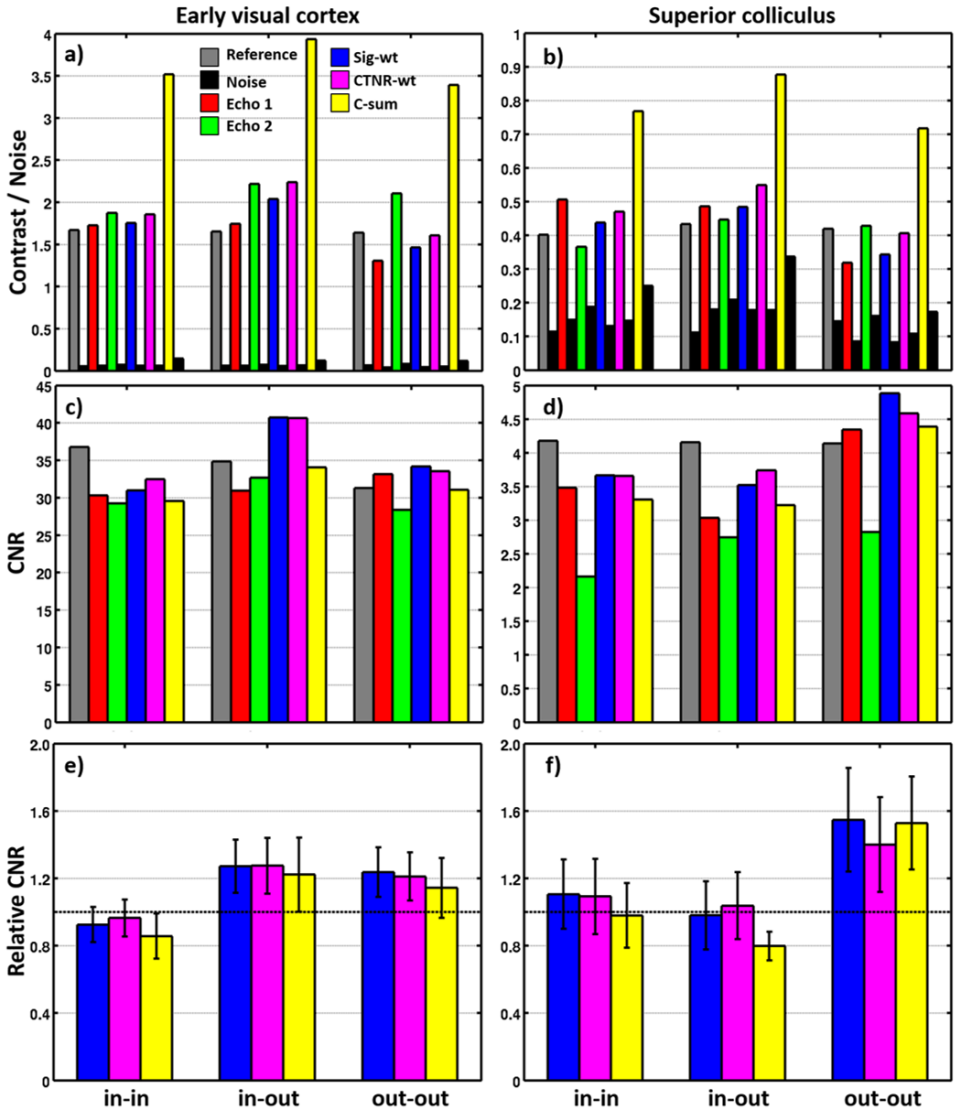

Figure 4.14: Comparison of various dual-echo combination schemes for the in-in, in-out and out-out spiral variants. a) & b) Mean BOLD contrast and noise for individual echoes and three combination schemes of Sig-wt, CTNR-wt and C-sum for cortex and superior colliculus, respectively. Data for the reference acquisition are also shown. c) & d) Corresponding mean BOLD CNR. e) & f) Mean relative CNR (w.r.t reference) for the combination schemes with the SEM plotted as error bars.

which the first echo has a mean intensity that is stronger than the second echo by a factor of $e^{\frac{T_{acq}}{T_2^*}}$. For the contrast-weighted (CTNR-wt) combination, it is difficult to interpret its effect because of its more complex combination-weight calculation. For the contrast-sum (C-sum) approach, the contrast sum results in a large increase in contrast, but also substantial increase in noise.

Figures 4.14c & d show the CNR corresponding to panels a & b. The CNR difference between EVC and SC is dramatic: CNR in EVC is 9.2× larger than in SC. The combination schemes offer differing performance improvements over the individual echoes. The Sig-wt and CTNR-wt schemes consistently perform better than the C-sum scheme. Comparatively, for both Sig-wt and CTNR-wt schemes, a reduction in BOLD noise is observed that leads to an increase in CNR over the individual echoes.

Figures 4.14e & f show CNR normalized to the reference acquisition. Error bars reflect the standard-error-of-the-mean (SEM) across sessions. The Sig-wt and CTNR-wt combination schemes generally succeed in increasing CNR over the individual echoes, but performance is mixed for the C-sum scheme. Overall, there are no significant differences between the combination schemes. There are weak trends for the Sig-wt and CTNR-wt schemes to outperform the C-sum scheme ($p \sim 0.3$). Generally the Sig-wt and CTNR-wt schemes perform about the same. We therefore chose to use the Sig-wt scheme in further analysis because it is not dependent upon the experiment design.

4.4.4 Sequence Comparison

Figure 4.15a shows contrast and noise normalized to the reference trajectory for each of the five trajectory variants in EVC. EPI performance is similar to the reference spiral out. Interestingly, spiral in offers a trend toward contrast improvement ($p = 0.11$), while noise remains largely unchanged. When two spiral-in echoes are combined, however, the contrast improvement is smaller, but noise increases substantially. The spiral in-out combination produces significantly greater contrast ($p < 0.002$), with a variable increase in noise ($p \sim 0.26$). Finally the out-out combination produces lower contrast ($p \sim 0$), but even lower noise ($p < 0.01$).

Figure 4.15b shows normalized contrast and noise for the five trajectory variants in SC. For most of the trajectory variants, the large errors are indicative of the small CNR observed in SC. All trajectories except the out-out show improvement in contrast, however there is also an increase in noise. The increase in contrast does not reach significance: EPI ($p \sim 0.12$), spiral in ($p \sim 0.19$), in-in ($p \sim 0.11$) and, in-out ($p \sim 0.14$). In comparison, the increase in noise is significant: EPI ($p < 0.006$), spiral in ($p < 0.008$), in-in ($p < 0.02$) and, in-out ($p < 0.03$). The out-out variant shows a trend for lower contrast ($p \sim 0.21$), but produces significantly less noise ($p < 0.005$).

Figure 4.15c shows the mean relative CNR for the five trajectories in EVC. There are trends for improved CNR for three of the variants. Single echo spiral-in is marginally superior to the reference (mean improvement 13%, $p = 0.11$). Greater improvements are seen for spiral in-out (mean 27%, $p =$

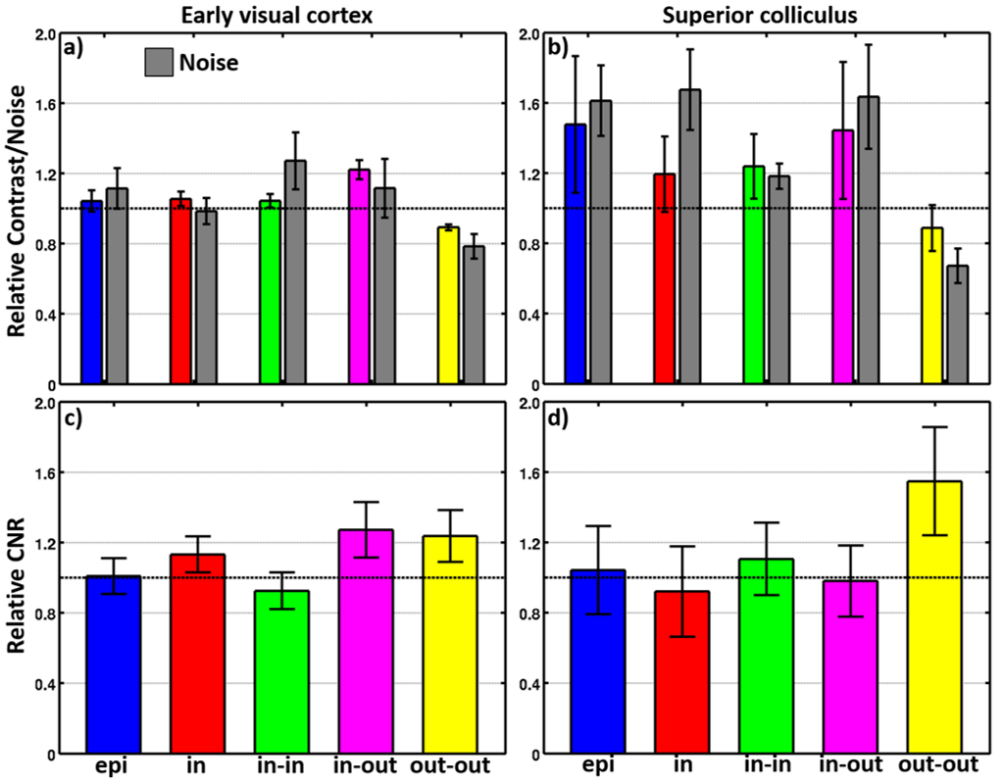

Figure 4.15: Comparison of BOLD contrast, noise and CNR for EPI and spiral variants: in, in-in, in-out and out-out with the single-echo spiral-out trajectory. a) & b) Mean relative contrast and noise for cortex and superior colliculus, respectively. c) & d) Mean relative CNR for cortex and superior colliculus, respectively. Error bars reflect the standard-error-of-the-mean (SEM).

0.06), and spiral out-out (mean 24%, $p = 0.07$). EPI performance is similar to the reference acquisition, and spiral in-in is slightly worse. In SC (Fig. 4.15d), only the dual-echo spiral out-out shows better performance than the reference acquisition (mean 55%, $p = 0.05$). Performance of the other variants is statistically indistinguishable from the reference.

4.5 Discussion

Our results quantify signal, contrast, and noise for high-resolution fMRI in both early visual cortex (EVC) and superior colliculus (SC). Results dramatically illustrate the challenges of subcortical imaging because of its lower SNR and much lower CNR. The low-resolution data in Fig. 4.12 cannot be directly compared to the current high-resolution data because of differences in field strength, scanner vendor, etc., but we can make detailed comparison between the high-resolution data in EVC and SC. Overall, the drop in SNR is only a factor of two between the two areas, and this mostly reflects reduced signal because SC is located farther from the coil elements. The 9.2× CNR drop of SC is mostly the consequence of reduced contrast ($\sim$ 4.2×), with a milder noise increase ($\sim$ 2.2×). Thus, midbrain imaging is predominantly difficult because BOLD contrast here is much lower than that in cortex, but increased noise also plays a role. Combining dual echoes is one strategy for dealing with the challenge of low CNR.

We used functional CNR as a metric to compare the performance of various multi-shot spiral variants for high-resolution imaging in human SC.

A similar performance analysis was also applied to GRAPPA-accelerated EPI acquisition. All acquisition trajectories were first evaluated to obtain optimal echo times. For each trajectory, optimal TE was chosen as the peak of parabola fitted to CNR values at multiple echo times for a subject. In SC, most spiral variants, and EPI, had similar performance. However, we observed significantly superior performance for the dual-echo spiral out-out variant. For comparison, we also evaluated CNR performance in EVC. Here we again found similar performance for both spiral out and EPI acquisitions. Notably, both spiral in-out and out-out offered the best performance, about $\sim$25% better than the reference. Single-echo spiral in also offered a small performance boost of $\sim$13%.

Although EPI performed similarly to single-echo spiral out, it is notable that the acquisition time for the EPI trajectory was 49 ms as compared to 35 ms for the spiral. This longer acquisition time should increase raw SNR by 18%. There was, however, no evidence for this improvement in either SNR or CNR; SNR was significantly lower, while CNR was similar to the single-echo spiral-out reference trajectory. Thus, the efficient use of gradient systems by the spiral trajectory appears to provide a small improvement in performance over EPI. However, this improvement is offset by the reduced acquisition efficiency of the asymmetric spiral out trajectory.

Our sequence performance evaluation strategy focused specifically on CNR, which is a critical requirement for high-resolution fMRI studies. Previous studies [82, 105] focused on evaluating spiral variants for signal recovery

in regions affected by susceptibility field gradients and evaluated performance using volume of activation above an arbitrary statistical threshold. Here, we used very small, $\sim$10 μL, retinotopically specified ROIs in the superficial layers of SC, putting a premium on accurate spatial localization both within and across imaging sessions. Subcortical imaging experiments must focus on small functional units that deliver comparatively weak signals and contrast [27, 69, 71, 114] in the presence of strong physiological nuisance effects [76]. Our results thus provide useful guidance in the selection of imaging schemes for such work.

The dual-echo spiral-out trajectory provided best performance in SC. The first echo delivers relatively less contrast, but with much lower noise than either the reference acquisition or the second echo. The second echo delivers much higher contrast, but the noise level is similarly increased. When the two echoes are then combined, the overall contrast is actually lower than the reference, but the noise is reduced still more. Apparently, this variant performs well because of noise suppression in the signal-weighted averaging process.

Both spiral out-out and in-out performed well in EVC. Spiral out-out again obtains its performance boost from noise suppression. Spiral in-out operates differently, offering a substantial increment in contrast with a relatively smaller increment in noise.

The performance of sequences using an inward spiral trajectory in SC was somewhat disappointing. It is possible that these trajectories were sensitive to small gradient errors during the initial pre-phase lobe. However, we

observed similar fidelity between contrast boundaries for both spiral in and spiral out images (Fig. 4.8). We therefore conclude that the trajectory fidelity was satisfactory. Also, sequences containing the spiral-in trajectory did show improvements in EVC. Certainly, the smaller ROIs in SC require finer spatial resolution than those in EVC. Each dual-echo combination provides different weightings of the spatial-frequency content within the BOLD contrast. Thus, it would appear that the dual-echo spiral out provides a better weighting for high spatial resolution. However, the SC data is considerably noisier than that in EVC, so it may be that finer details of trajectory performance will require more experimentation to improve statistical power.

We evaluated three schemes for combining the two echoes: signal-weighted, contrast-to-temporal-noise-ratio -weighted, and contrast-sum. There were no statistically significant differences between these schemes, but the contrast-sum scheme had a trend toward lower performance, while the other two schemes offered statistically similar performance. The signal-weighted scheme was therefore chosen for use in SC because it is independent of the experiment design. This choice is also consistent with previous results [47, 105].

Although the dual-echo variants performed better than the other schemes, the performance boost requires substantially higher total acquisition time. This increase in acquisition time can be compensated by reducing the volumetric coverage. For example, in our imaging protocols the spiral dual-echo out-out at TE = 30 ms can only acquire 9 slices in comparison to 12 slices for the reference single-echo out trajectory with TE = 40 ms. This (25%) reduc-

tion in volumetric coverage is acceptable for studies focused on imaging small functional units such as the superior colliculus, however it is not satisfactory for imaging larger regions such as the whole of early visual cortex. Otherwise, improving slice coverage would require increasing the repetition time, or reducing acquisition time through fewer interleaves or higher-speed trajectories at the cost of lower SNR. Altogether, the performance boost of multi-echo acquisition comes at a price of reduced volumetric coverage.

4.6 Conclusions

High-resolution functional magnetic resonance imaging of human subcortical brain structures is challenging due to their deep anatomical location within the cranium and their comparatively weak BOLD responses even to strong stimuli. Accordingly, functional data for SC exhibit both low SNR and BOLD CNR. In this chapter, we evaluated the use of dual-echo spiral variants to improve the quality of the BOLD signal acquired from SC. Dual echo variants: in-in, in-out and out-out were evaluated. For completeness we also evaluated single-echo spiral in and a GRAPPA accelerated EPI sequence. Evaluation of the sequences was based on comparison of BOLD contrast-to-noise ratio within retinotopically predefined regions-of-interest. All sequences were compared relative to a single-echo spiral-out trajectory to establish a within-session reference. In SC, the dual echo out-out outperformed the reference trajectory, while all other trajectories performed comparably to the reference trajectory. In EVC, both dual-echo spiral out-out and in-out outperformed

the reference.

Chapter 5

Fast Dynamic Magnetic Resonance Imaging using Linear Dynamical System Model

5.1 Introduction

Magnetic resonance imaging is a slow imaging modality and many research studies over the past two decades have focused on improving its imaging speed. Many of the these studies are motivated by the emerging medical diagnostic procedures which rely on detailed characterization of physiological functions of critical organs such as cardiac and brain [130, 132]. The early studies (late 90s and early 2000s) were based on exploiting the redundancy in the raw data space (spatial Fourier a.k.a k-space) in either the spatial dimension or the temporal dimension or both [42, 59, 66, 67, 94, 104, 123, 125]. For example, k-t BLAST [125], HYPR [94] and k-t FOCUSS [66, 67]: all formulate the problem as recovering a residual image for each time-point with respect to a reference image. The reference image encodes the data redundancy in image time-series and is usually recovered by combing data from multiple time-points. More recent studies (after 2006) are based on the theory of compressed sensing (CS) which relies on recovering a transform of the underlying image in a basis where its representation is sparse and which exhibits high incoherency with the k-space sampling basis [15, 41, 83, 85, 87, 117]. CS-based techniques for dynamic

MR applications enforce sparsity in the spatial dimension and/or in the temporal dimension. For example, in [41, 83], the wavelet and one-dimensional Fourier transforms are used to sparsify the images in the spatial and temporal dimension. Clearly, CS techniques based on using sparsity priors in a single dimension are sub-optimal as the inherent redundancy in the complimentary dimension is unaccounted for. For other techniques, the sparsity priors in multiple dimensions are weakly coupled by the Lagrange constants used in the selected solution of the non-linear optimization problem. On the contrary, all physiological functions can be modeled using linear or non-linear evolution models. In these models the spatial and temporal redundancy is inherently coupled. Therefore, a sparse recovery formulation based on time evolution models of physiological functions should allow to recover images with higher fidelity than previous techniques. In this paper, a linear dynamical system based evolution model is combined with sparse recovery techniques to increase imaging speeds in dynamic MRI.

Linear dynamical systems (LDS) have been previously used to model various physiological processes such as: 1) blood flow in MR angiography and perfusion studies and, 2) periodic motion in cardiac and abdominal imaging [103, 141]. Thus, LDS models are generic and exhibit a wide applicability for modeling various physiological functions. In recent past, LDS model has been used for dynamic MRI formulations [3, 39, 118, 120, 127, 128]. In the classic dynamical systems literature, a model for a changing state vector and mea-

surement process is described by the following equations:

$$x_{k+1} = f_k(x_k) + u_k \tag{5.1a}$$

$$y_k = \mathbf{H}_k\, x_k + v_k \tag{5.1b}$$

where, $x_k \in R^N$ represents the signal of interest, $f_k(.)\,|R^N \rightarrow R^N$ represents the known evolution of the signal from time k to $k+1$, $y_k \in R^M$ is a set of linear measurements of x_k, $v_k \in R^M$ is the associated measurement noise, and $u_k \in R^N$ is the modeling error for $f_k(.)$ (commonly termed as the innovations). For a linear system the evolution function can be summarized as a $N \times N$ matrix, i.e., $f_k(.) = A_k$. In the case where $\mathbf{H}_k$ is invertible ($N = M$ and the matrix has full rank), state estimation at each iteration reduces to a least squares problem.

In LDS based fast dynamic MRI formulations, the underlying images are modeled as the hidden states x_k and the under-sampled k-space data (i.e., $M \ll N$) as the observations y_k. To accurately estimate the hidden states from their highly under-sampled measurements solutions capable of leveraging the additional knowledge of state dynamics and signal structure are required. The techniques in [3, 127, 128] use signal sparsity to counter the under-determinedness of the LDS MRI problem. In [127], the states of the dynamical system are assumed to be sparse and the state estimation problem is separated into two sub-problems of support and value estimation. Authors in [127] propose a CS-based ad-hoc Kalman filtering solution, where CS is used to estimate the support and the Kalman filter is run on the estimated support to track the

states. Similarly, in [3] authors assume sparse states along with a zero-mean additive white Gaussian distribution for the state modeling noise. Their solution is based on adding a group-sparsity constraint to the established Kalman smoothing formulation. The added constraint (group-LASSO) forces groups of coefficients along the temporal dimension to zero. The approach of [128] extends that of [127], it enforces sparsity on state-differences as opposed to that of state themselves. The aforementioned techniques assume the following: 1) the states are sparse and, 2) the state transition matrix for changing support of state vectors are always known. These two requirements are not necessarily true for dynamic MR applications where the underlying images represent the unknown states.

This chapter presents a novel formulation for fast dynamic MRI based on linear dynamical system (LDS) model and sparse approximation methods. In the proposed formulation, unlike previous techniques [3, 127, 128] the system innovations are assumed to be sparse instead of the states themselves, i.e., it is the error in state evolution model which is assumed to be sparse. The proposed formulation makes no assumptions about the underlying images like previous techniques, however it requires the knowledge of a time-evolution model for the underlying function. This time-evolution model inherently encodes for data redundancies in both spatial- and temporal-space as opposed to techniques which explicitly account for therm [41, 42, 66, 67, 83, 94, 125]. For example, the highly constrained back projection (HYPR) method of [94] enforces spatio-temporal redundancy by explicitly sharing high-frequency details

between neighboring time-frames and oversampling the low-frequency information for each frame to capture the contrast information. The HYPR technique has been shown to recover sparse angiographic images at high acceleration factors $\sim$ 25 [94], however for not-so-sparse images gains of $\sim$4 only, have been reported [42]. The preliminary results of dynamic MRI recovery experiments on an in-vivo myocardial perfusion dataset show that the proposed LDS based technique preserves details like edges and fine structures in recovered images better than many of the previous techniques for static and dynamic MRI [41, 66, 87, 94, 118, 120].

The rest of this chapter is organized as follows. Section 5.2 presents the mathematical treatment of the proposed linear dynamical system based fast dynamic MRI technique. Section 5.3 summarizes various experimental results on an in-vivo myocardial perfusion and Cardiac CINE data sets. Finally, section 5.3 concludes the chapter.

5.2 Linear Dynamical System based Dynamic MRI model

This section presents the mathematical formulation of the proposed linear dynamical system based dynamic MRI model. Let x_k represent the Nx1 MR image acquired at k^{th} time-point for a physiological function. The dynamic MR imaging process in terms of the linear dynamical system is

$$x_{k+1} = \mathbf{A}_k \, x_k + u_k \tag{5.2a}$$

$$y_k = \mathbf{H}_k \, x_k + v_k \tag{5.2b}$$

where, $\mathbf{A}_k$ is the NxN state transition matrix, u_k is the innovation, y_k is the acquired k-space data, $\mathbf{H}_k$ is the MxN under-sampling matrix ($M \ll N$) and v_k is the sampling noise. In this work, following assumptions are made: 1) the state transition matrices $\mathbf{A}_k$'s are known and, 2) the noise u_k is sparse. These assumptions are true for various physiological functions. For example, in MR angiography and perfusion, within the imaged Field-of-View (FOV) the anatomical boundaries do not change over time but only the image-contrast varies over time. Thus, for angiography and perfusion studies, $\mathbf{A}_k$ is the identity transform and the sparse innovations u_k models the contrast changes between time-points if any. For cardiac CINE studies, the state transition equation (5.2a) can be replaced with a 2^{nd} order auto-regressive model while still modeling the system innovations u_k as sparse. Sampling noise v_k is in the complex space and is assumed to be $\mathcal{N}(0, \mathbf{R}_k)$, where $\mathbf{R}_k$ is the covariance matrix.

Similar to the solution of Kalman filter in Eq. (2.21), the fixed-interval solution for problem (5.2) with sparse u_k is

$$\min_{x_1,\ldots,x_k} \sum_{i=1}^{k} \tau_i \parallel x_i - \mathbf{A}_{i-1} x_{i-1} \|_1 + \sum_{i=1}^{k} \lambda_i \parallel \mathbf{H}_i x_i - y_i \parallel_2^2 \tag{5.3}$$

where, l_1-norm reflects the sparsity.

To solve (5.3), we can solve for $\{\widehat{u}_i\}_{i=1}^k$ and then use them to estimate for $\{\widehat{x}_i\}_{i=1}^k$ explicitly using (5.2a). Now, the sparse innovations $\{\widehat{u}_i\}_{i=1}^k$ can be

vectorized and rearranged as

$$\begin{bmatrix} u_1 \\ u_2 \\ \vdots \\ u_{k-1} \end{bmatrix} = \begin{bmatrix} \mathbf{I} & \mathbf{0} & \dots & \mathbf{0} \\ -\mathbf{A}_1 & \mathbf{I} & \dots & \mathbf{0} \\ \vdots & \vdots & \ddots & \vdots \\ \mathbf{0} & \dots & -\mathbf{A}_k & \mathbf{I} \end{bmatrix} \begin{bmatrix} x_1 \\ x_2 \\ \vdots \\ x_{k-1} \end{bmatrix} - \begin{bmatrix} \mathbf{A}_0\widehat{x}_0 \\ 0 \\ \vdots \\ 0 \end{bmatrix}$$

$$\mathbf{u} = \mathcal{A}\mathbf{x} - \mathbf{z} \tag{5.4a}$$

where, $\widehat{x}_0$ is the initial estimate. Now, using (5.4) we can rearrange the second term in (5.3) as

$$\sum_{i=1}^{k} \| \mathbf{H}_i x_i - y_i \|_2^2 = \| \mathcal{H}\mathbf{x} - \mathbf{y} \|_2^2 \tag{5.5a}$$

$$= \| \mathcal{H}\mathcal{A}^{-1}\mathbf{u} - \left(\mathbf{y} - \mathcal{H}\mathcal{A}^{-1}\mathbf{z}\right) \|_2^2$$

$$= \| \mathcal{H}\mathcal{A}^{-1}\mathbf{u} - \widetilde{\mathbf{y}} \|_2^2 \tag{5.5b}$$

where, $\mathbf{y}$ is the vector obtained by stacking $\{y_i\}_{i=1}^{k}$ sampled vectors, $\widetilde{\mathbf{y}} = \mathbf{y} - \mathcal{H}\mathcal{A}^{-1}\mathbf{u}$ and $\mathcal{H}$ is

$$\mathcal{H} = \begin{bmatrix} \mathbf{H}_1 & \mathbf{0} & \dots & \mathbf{0} \\ \mathbf{0} & \mathbf{H}_2 & \dots & \mathbf{0} \\ \vdots & \vdots & \ddots & \vdots \\ \mathbf{0} & \mathbf{0} & \dots & \mathbf{H}_k \end{bmatrix} \tag{5.6}$$

Note, in (5.5b), $\mathcal{A}^{-1}$ is simple to calculate due to the lower-triangle property of matrix $\mathcal{A}$. Using (5.2a) and (5.5b) in equation (5.3), the new fixed-interval optimal smoother is:

$$\min_{u_1,\dots,u_k} \sum_{i=1}^{k} \| \mathbf{u} \|_1 + \frac{1}{2} \| \mathcal{H}\mathcal{A}^{-1}\mathbf{u} - \widetilde{\mathbf{y}} \|_2^2 \tag{5.7}$$

where, $\tau_i = 1, \lambda_i = 1 \forall i$ is assumed to yield the recognizable basis-pursuit denoising problem of Eq. (2.12). In (5.7), the dimensionality of the problem

increases with k. For tractable problems, a sliding window based approach can be used. Problem (5.7) can be solved for using any of the previously established methods [7, 20, 87]. The solution to (5.7) for all results presented in this paper are obtained using the the NESTA toolbox which implements the Nesterov's algorithm [7].

5.3 Experiments and Results

The proposed linear dynamical system (LDS) based fast dynamic MRI technique is validated through retrospective under-sampling experiments on in-vivo myocardial perfusion and cardiac CINE data set (complex raw images). Following metrics are used to quantify the fidelity of recovered images in retrospective experiments : (1) SNR : signal-to-noise ratio and, (2) SSIM: structural similarity index. SNR in decibels (dB) is computed as the ratio of the mean reference intensity to the root mean square of the reconstruction error. SSIM provides a measure to assess the degradation of structural information, it compares local pixel-intensity patterns that are normalized for luminance and contrast [131]. In this paper, experimental results are presented for both 2DFT and radial under-sampled acquisitions. For radial under-sampling inverse-gridding is used to generate k-space data from complex raw images.

5.3.1 Myocardial Perfusion Imaging

The myocardial perfusion data was acquired on a Siemens 3T scanner with a saturation-recovery sequence (TR\TE= 2.5/1ms, saturation recovery

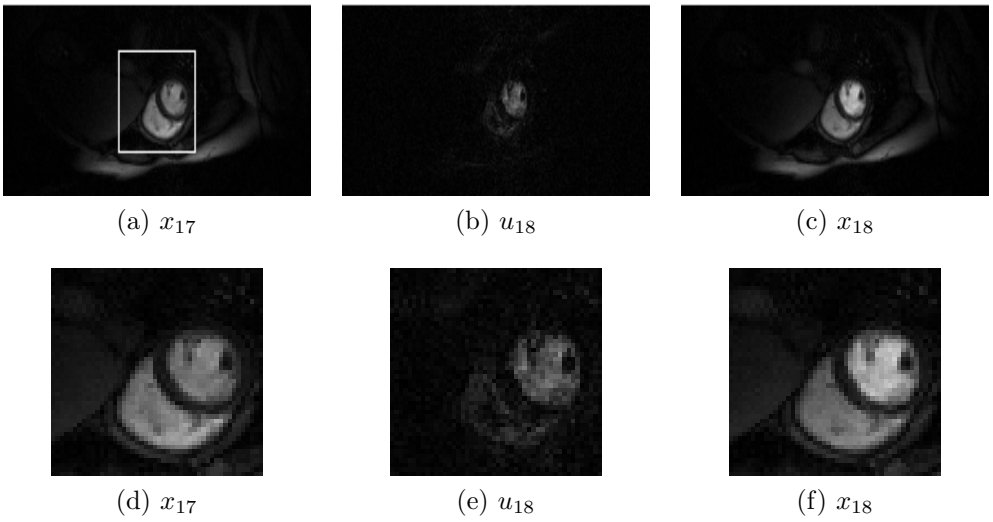

(a) x_{17} (b) u_{18} (c) x_{18}

(d) x_{17} (e) u_{18} (f) x_{18}

Figure 5.1: Myocardial perfusion imaging data set. (a) & (c) Reference time-points #17 and #18. (b) Reference innovation (u_k) for time-point #18 which for this data set is the difference image between (a) & (c). (d), (e) & (f) show zoomed regions from the reference images for the region marked in (a).

time= 100ms) and comprises of an image matrix of size 90x190x70 (phase-encodes x frequency encodes x temporal slices) [85]. For perfusion imaging the evolution function is assumed for the temporal difference, i.e., the A_k's in eqn. (5.2a) are identity matrices. Alternatively, it is assumed that the temporal difference between consecutive time-points are sparse in the spatial dimension. Figure 5.1 shows magnitude of time-frames #17 and #18 from the data set and the magnitude of difference between them. These time frames are specifically chosen as they show the inflow of the contrast-enhanced blood into the left-atrium as seen in the innovation signal in fig. 5.1b. To qualify the sparsity of the innovation signal, power-law decay curves are plotted for the voxel values of temporal-difference images. Figure 5.2 plots the power-

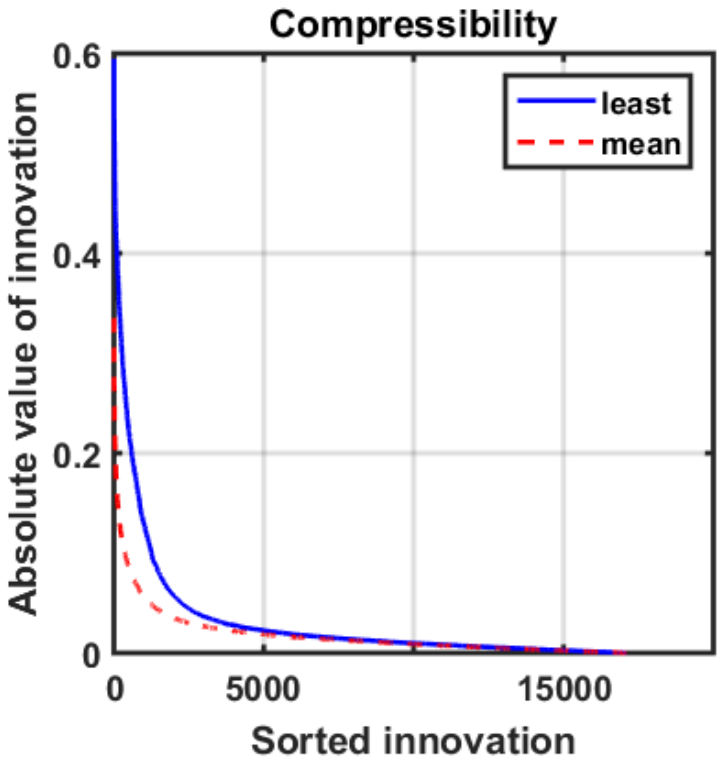

Figure 5.2: Sparsity of innovation signal for myocardial perfusion data set.

law decay curves for two innovation images: 1) with least sparsity and, 2) with sparsity close to the mean sparsity, where sparsity is measured as ratio of number of voxels with intensity greater than 1% of maximum temporal-difference intensity to the dimension of the image.

5.3.1.1 Linear Dynamical System based Recovery

Figure 5.3 shows the results for an image recovery using the proposed linear dynamical system based fast MRI method for retrospective radial under-sampling at an acceleration factor of $R = 4$. A sliding window of 4-samples

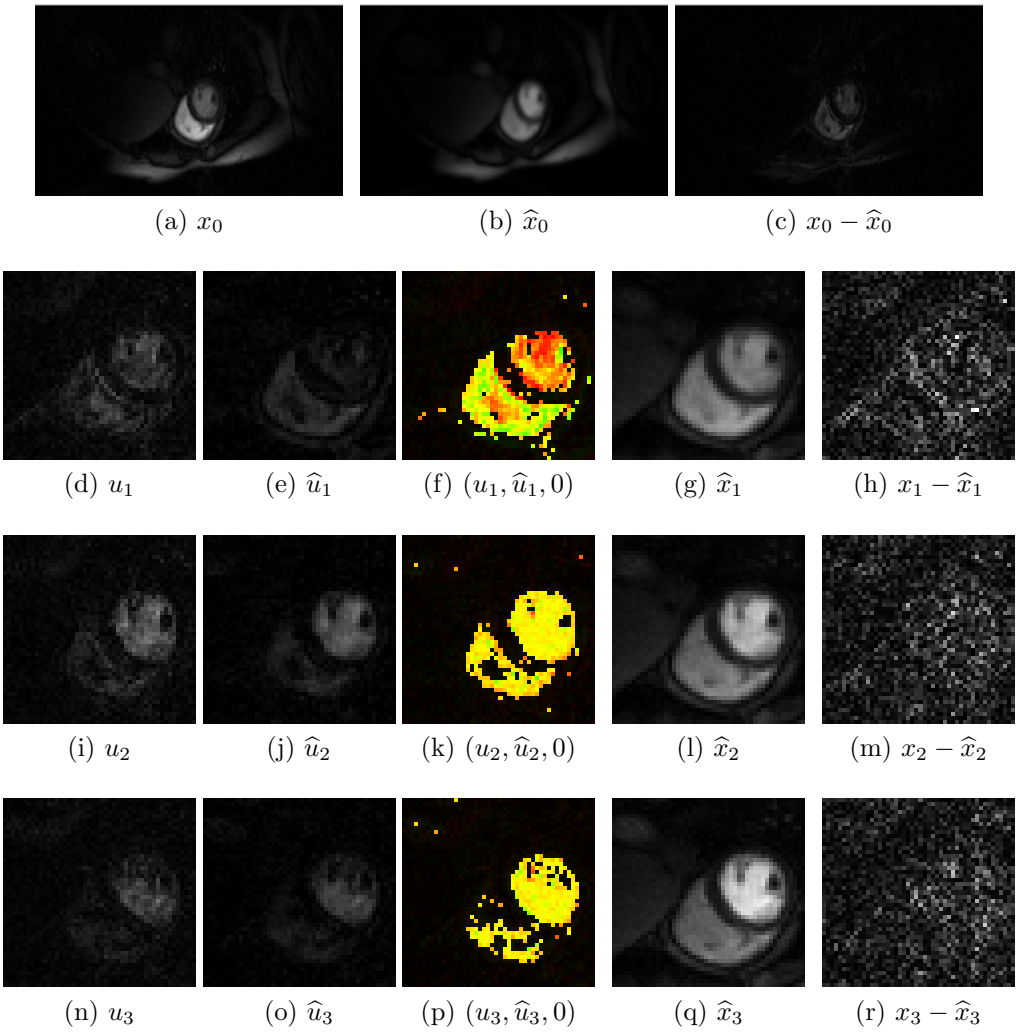

(a) x_0 (b) $\widehat{x}_0$ (c) $x_0 - \widehat{x}_0$

(d) u_1 (e) $\widehat{u}_1$ (f) $(u_1, \widehat{u}_1, 0)$ (g) $\widehat{x}_1$ (h) $x_1 - \widehat{x}_1$

(i) u_2 (j) $\widehat{u}_2$ (k) $(u_2, \widehat{u}_2, 0)$ (l) $\widehat{x}_2$ (m) $x_2 - \widehat{x}_2$

(n) u_3 (o) $\widehat{u}_3$ (p) $(u_3, \widehat{u}_3, 0)$ (q) $\widehat{x}_3$ (r) $x_3 - \widehat{x}_3$

Figure 5.3: Image recovery using the proposed linear dynamical system model based method for radial under-sampling at an acceleration factor of $R = 4$. (a), (b) Oracle and true initial state estimate for time-frame #16 and their difference magnitude shown in (c). (d), (i) & (n) true innovation for time-frames #17, #18 and #19, respectively. (e), (j) & (o) recovered innovations, (f), (k) & (p) visual qualification of recovered innovations (yellow: correctly detected, red: missed, green:spurious detections). (g), (l) & (q) recovered images and, (h), (m) & (r) error images.

(k in (5.4a)) is used. The initial state ($\widehat{x}_1 6$ in fig. 5.3b) is estimated using the sliding window technique which combines the under-sampled data from all four time-points to yield a smooth estimate. Figures 5.3a and 5.3c show the oracle initial state and the error of the initial state estimation, respectively. Figures 5.3d-5.3h show the zoomed true innovation, recovered innovation, innovation-match rgb image, recovered image and error image for the time-frame #17. Similar images are shown for time-frames #18 in figs. 5.3i-5.3m and #19 in figs. 5.3n-5.3r. Error images are scaled from zero to 10% of the maximum image intensity in the time-series. The innovation-match image is generated by assigning to the red- and green-channel of an rgb-image as the true and recovered innovation images divided by their mean image, respectively. Thus, the innovation-match image shows strong yellow for exactly recovered voxels, red for missed voxels and green for spuriously detected voxels. Note, in the proposed approach the innovation signal is recovered ($\widehat{u}_{1-3}$)'s and is added to the previously estimated image ($\widehat{x}_{0-2}$) to obtain the new image estimate ($\widehat{x}_{1-3}$). Since, the initial estimate is different from true initialization the innovation-match image in fig. 5.3f shows large regions of red and green voxels. However, within few sliding-window steps as the image recovery improves the fidelity (reduced red and green voxels) of innovation-match image improves too. The improvement in the fidelity can also been seen in the error images (figs 5.3h, 5.3m and 5.3r).

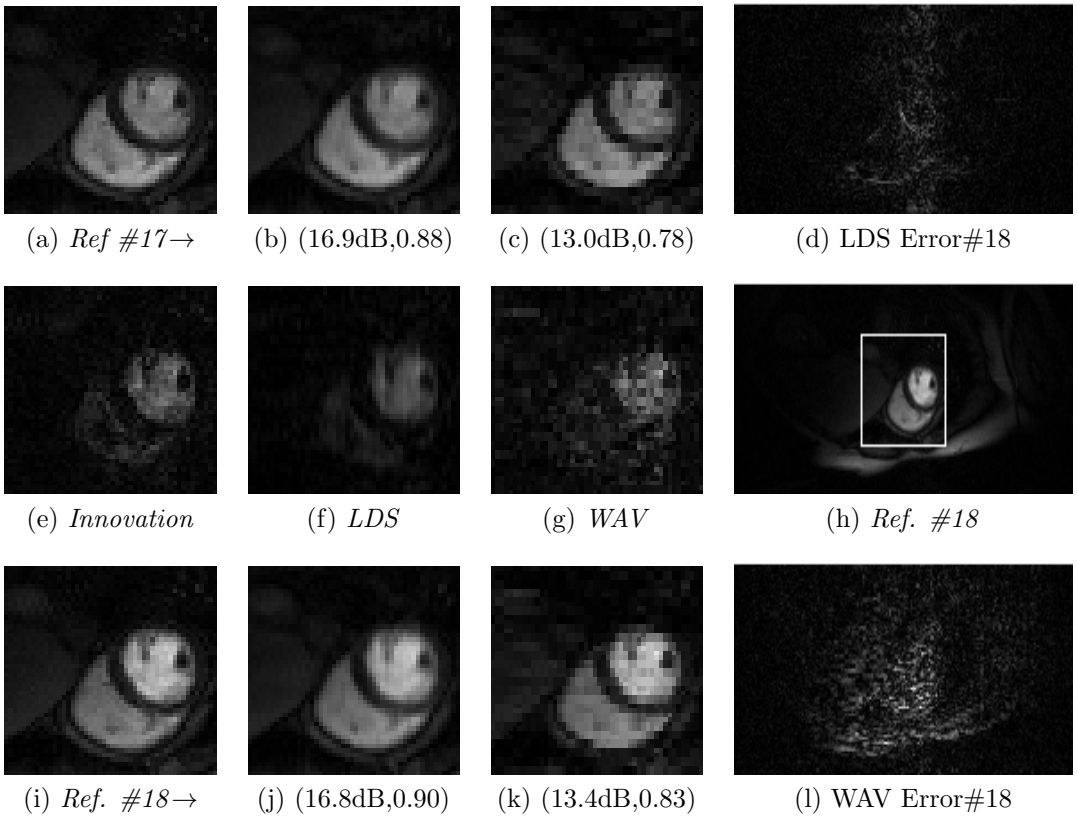

(a) *Ref #17→* (b) (16.9dB,0.88) (c) (13.0dB,0.78) (d) LDS Error#18

(e) *Innovation* (f) *LDS* (g) *WAV* (h) *Ref. #18*

(i) *Ref. #18→* (j) (16.8dB,0.90) (k) (13.4dB,0.83) (l) WAV Error#18

Figure 5.4: Comparison of image recovery using the proposed method and a Wavelet-sparsity based CS technique at an acceleration factor of $R = 4$. (a) shows the zoomed-in region from the reference image (f) of time-point#17. (i) shows the reference zoomed region from time-point#18. (e) shows the difference between (a) and (i) which corresponds to the *innovation* in the linear dynamical system model. The second and third column show the recovered images and innovations for proposed LDS and the WAV technique, respectively. Performance for each technique is reported as pairs (SNR, SSIM) below the corresponding recovered images. (d) and (l) show the error images for the LDS (time-point#17) and WAV (time-point#18) technique, respectively.

5.3.1.2 Comparison with Spatial-only CS Recovery

Figure 5.4 shows the results for a retrospective variable density 2DFT under-sampling experiment at an acceleration factor of $R = 4$. Image recovery results are also shown for the standard Wavelet sparsity based CS technique [87]. For reasons of convenience the experimental results for the proposed technique will be referred to as LDS and for the Wavelet sparsity based CS technique as WAV. For the LDS method, a sliding window of 4-samples (k in (5.4a)) is used and the initial state estimate $\widehat{x}_0$ is obtained by combining data from all time-points in the first sliding window and a taking a Fourier transform of it. Recovered images for two consecutive time-points (17 and 18) and the true and recovered innovation signal (u_{17} in (5.2a)) are shown for both the LDS and WAV techniques. The LDS technique estimates the innovation signal in fig. 5.4f using composite under-sampled data from 4-time-points and uses it to estimate fig. 5.4j from fig. 5.4b. The WAV technique treats each time-point independently and the innovation shown in 5.4g is calculated post-image-recovery. The LDS technique outperforms the WAV technique qualitatively and quantitatively as it inherently accounts for the temporal correlations which are not exploited in the WAV technique. The LDS technique shows much reduced under-sampling artifacts than the WAV technique, this can be observed in the error images of figs. 5.4d and 5.4h. Again, this can be attributed to sharing of k-space information through the used time-evolution model which is absent in the WAV technique.

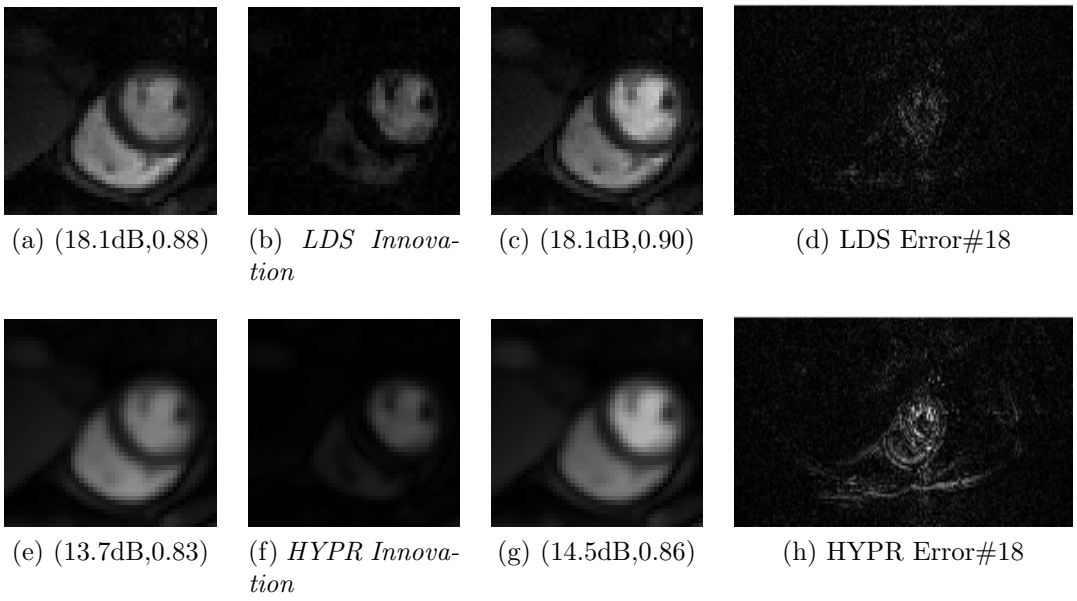

(a) (18.1dB,0.88) (b) *LDS Innovation* (c) (18.1dB,0.90) (d) LDS Error#18

(e) (13.7dB,0.83) (f) *HYPR Innovation* (g) (14.5dB,0.86) (h) HYPR Error#18

Figure 5.5: Comparison of image recovery using the proposed method and the HYPR at an acceleration factor of $R = 4$. (a) and (e) show a zoomed-in region from recovered images for time-point #17 for the LDS and the HYPR technique, respectively. Similarly, (c) and (g) show the region from recovered images for time-point #18. Corresponding innovations are shown in (b) and (f). Performance for each technique is reported as pairs (SNR, SSIM) below the corresponding recovered images. (d) and (h) show the error images for the time-point#18 for the LDS and HYPR technique, respectively.

5.3.1.3 Comparison with Temporal Redundancy based Recovery Technique

Figure 5.5 shows the results for the radial under-sampling experiments at an acceleration factor of $R = 4$ for the LDS and the HYPR [94] techniques are shown. To reduce redundancy, only the recovered images, innovation and error images are shown. However, results are presented for the same time-points (# 17 and 18) as shown in figs. 5.3 and 5.4. Similar to the 2DFT

experiments, the LDS method uses a sliding window of 4-samples and uses the image recovered using the HYPR technique as the initial state estimate $\widehat{x}_0$. In fig. 5.5, for both techniques no visible radial streaking artifacts are observed as they both use raw-data from multiple time-points to estimate each image. The HYPR technique recovers a composite image for the sliding window using filtered back-projection and multiplies it with a different weight image for each time-point to recover the corresponding image. The weight image is determined separately for each time-point using unfiltered back-projection reconstruction of the composite image data and the under-sampled time-point data. The composite HYPR image results in smoothing of details and edges as seen in figs. 5.5e, 5.5f and 5.5g. This loss at edges is results in high errors at edges in fig. 5.5h. On the contrary, the proposed LDS technique uses combined data to estimate the innovation signal with sparsity constraint which does not adversely effects the image details. The LDS error image in fig. 5.5d shows discrepancies which are not localized to edges.

All the results presented in figs. 5.4 and 5.5 use a sliding window of size $k = 4$. However, in (5.7), a different k (usually higher) can be selected at the expense of the increased dimensionality of the inverse problem. This increase in problem-size is also accompanied with a corresponding increase in the amount of sampled data available ($\widetilde{y}$). Thus, no significant change in recovery performance should occur if the sparsity of innovations (in (5.7)) was constant across time. However, this is not true for physiological functions and therefore increasing the sliding window size k should result in changes in

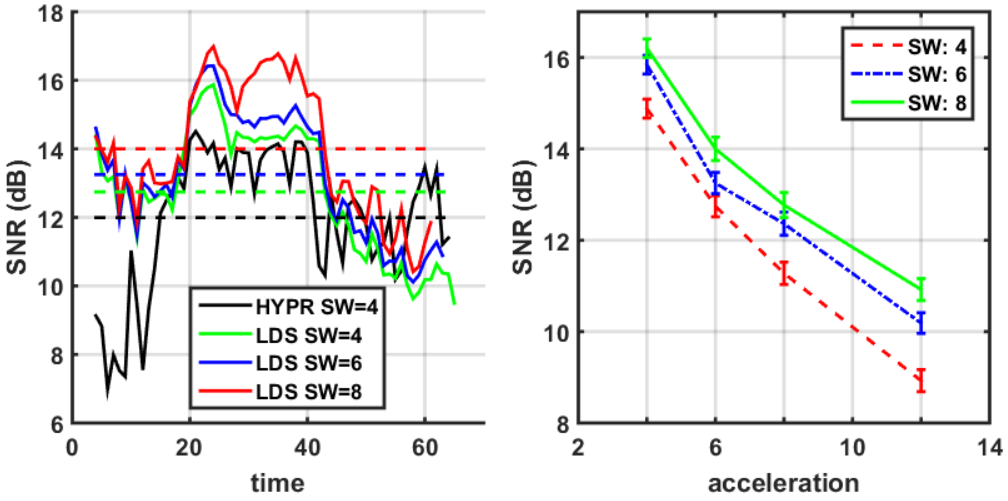

(a) (b)

Figure 5.6: Performance characterization of the LDS technique for varying sliding window sizes on the In vivo myocardial perfusion data set. (a) SNR versus time curve for the LDS recovery at an acceleration of R = 6. (b) SNR ($\mu \pm \sigma$) versus acceleration curves for three different window sizes.

performance metrics. Figure 5.6 shows the results obtained for radial undersampling experiments on the in vivo myocardial perfusion data for varying sliding window sizes. Figure 5.6a plots the SNR versus time curve for the proposed LDS technique for sliding window (SW) sizes: 4, 6 and 8 and the HYPR technique (SW= 4)at an acceleration factor of $R = 6$ with dotted-lines showing the corresponding mean SNR values. For this data set, the recovery performance increases as the sliding window size is increased at $R = 6$. Figure 5.6b plots the (mean±std. deviation) SNR values for three different sliding window sizes at varying acceleration factors. For this data set a recovery performance boost of 1dB is observed as sliding window size is increased from 4 to 8.

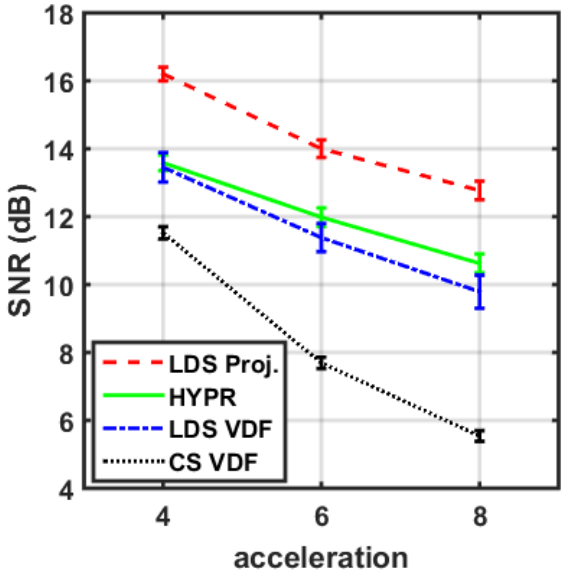

Figure 5.7: ($\mu \pm \sigma$) SNR (in dB) versus acceleration (R) curve for the proposed LDS, the HYPR and the WAV techniques on the in-vivo myocardial perfusion data set.

Figure 5.7 characterizes the performance of the LDS (radial and 2DFT under-sampling), the HYPR and the WAV techniques over the complete data set as a function of acceleration (R) in terms of the SNR. Based on fig. 5.7, following observations can be made: 1) radial under-sampling experiments perform better the VDF acquisitions for the proposed LDS technique, this can be attributed to relatively higher energy in the central k-space for the given data set which is sampled relatively more densely for the radial under-sampling, 2) LDS technique recovers dynamic images with higher SNR than both the HYPR and the WAV technique. These observations are simple extension of the results previously seen in figs. 5.4 and 5.5.

First-pass myocardial perfusion MRI is used to detect and evaluate

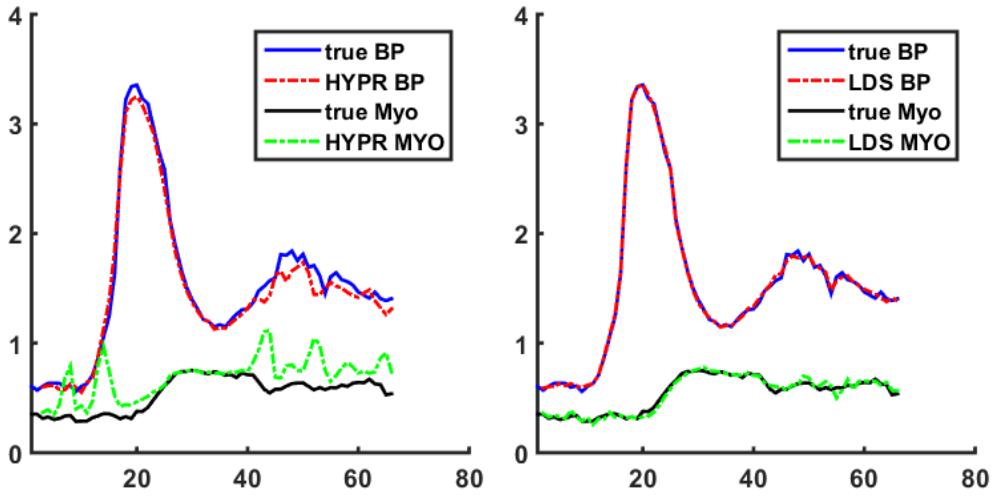

(a) *HYPR* (b) *LDS*

Figure 5.8: Time-series plot of averaged signal intensity for recovered (at R = 6) and reference images for the in-vivo myocardial perfusion dataset.

ischemic heart disease [42]. Regional perfusion defects can be detected by analyzing the signal variability in an image time-series. A high temporal and spatial resolution is required to accurately localize the defected tissue [42]. Thus, to assess the applicability of a fast technique for myocardial perfusion imaging, time series plots of averaged signal intensity in selected blood pool and myocardium regions are critically evaluated. Figures 5.8a and 5.8b compare the time-series plots of averaged signal intensity in selected blood pool and myocardium regions in reference images with that of the recovered images at acceleration $R = 6$ using the *LDS* and the *HYPR* techniques, respectively. The selected blood pool (in red) and myocardium (in green) regions are shown in Figs. 5.4a. As expected, the time series curve for recovered images using the *LDS* scheme follows the reference curve more closely than the curve for

the *HYPR* sampling scheme.

5.3.1.4 Comparison with Spatio-Temporal Techniques

As stated earlier, there have been many techniques for improving the dynamic MRI speeds based on exploiting the redundancy in the spatio-temporal k-space data. Thus, to fully evaluate the efficacy of the LDS technique, its performance should be compared with that of the others. However, given the large number of techniques, a one-to-one comparison with all of them is impossible. In this paper, the LDS technique is compared with four techniques which are very distinctive from the LDS technique and also from one another. The four techniques are: 1) Kalman filtering, 2) k-t Sparse, 3) k-t FOCUSS and 4) Low-rank plus sparse matrix. A brief description of these techniques is provided below.

Kalman filter: In [118, 120], the traditional Kalman filter (Eq. (2.21)) is used to continuously update the current image using the evolution model A_k and the sampled data. The Kalman filter updates require matrix inversion which for nominal sized images can be computationally intensive. To make the Kalman solution tractable, incorrect physical assumptions: 1) independence among voxels in the innovations u_k in Eq. (5.2) and, 2) kroncekar-delta function for power spectral density of non-Cartesian acquisitions are made in [118, 120]. In [39], the approach of [118, 120] is extended to Cartesian acquisitions, however it retains the unrealistic assumptions of [118, 120] for a tractable solution.

k-t Sparse: In [41, 90] sparsity in the wavelet transform domain and the temporal Fourier domain is used in the spatial and the temporal dimension, respectively. The temporal Fourier is ideal to sparsify periodic functions.

k-tFOCUSS: In [66, 67] encodes the redundancy in the temporal dimension using prediction schemes and in a subsequent step, uses the sparsity of the residual time-series to recover images. In the prediction step, the near-static image locations image locations are approximated either as temporal average over the acquired time-series or merely as the closest image patch from fully sampled reference images.

Low-Rank plus Sparse Matrix: In [102] it is argued that the time-frames in dynamic MRI can be separated into two components when the individual time-points are arranged as columns of a large matrix. A low-rank component which corresponds to the information which is correlated in time and the second sparse component which captures the fast temporal dynamics and can be represented sparsely in a select domain. For example, in cardiac CINE studies, the motion in the images can be sparsified in the temporal Fourier domain due to its periodic nature. Using these constraints the signal can be recovered from its under-sampled observations. Few studies have also used only the rank-deficiency [85, 143], however they have been shown to be outperformed by the low-rank plus sparse matrix based recovery techniques.

Figure 5.9 and 5.10 show the image recovery on the in-vivo myocardial perfusion data using five different techniques: 1) Kalman filter (KF) [39, 118, 120], 2) k-t Sparse [41], 3) k-t FOCUSS [66], 3) Low-rank plus sparse matrix

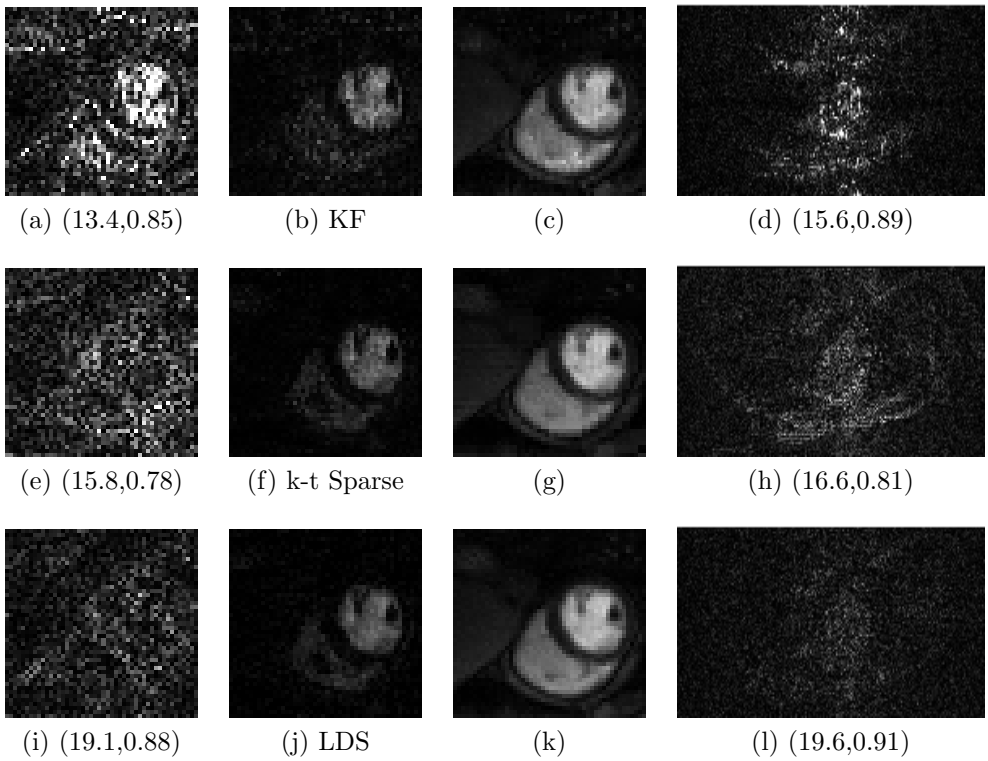

(a) (13.4,0.85) (b) KF (c) (d) (15.6,0.89)

(e) (15.8,0.78) (f) k-t Sparse (g) (h) (16.6,0.81)

(i) (19.1,0.88) (j) LDS (k) (l) (19.6,0.91)

Figure 5.9: Comparison of image recovery using five different spatio-temporal fast dynamic MRI techniques at an acceleration of $R = 4$ (1 of 2). Each row shows results for a technique which is mentioned in the second column. **First col.**: Zoomed-in error images for time-point #17, **Second col.**: Zoomed-in innovation signal, **Third col.**: Zoomed-in recovered images for time-point #18 and, **Fourth col.**: Error images for time-point #18. Image recovery performance metrics are mentioned as (SNR (dB), SSIM) pairs below the error images.

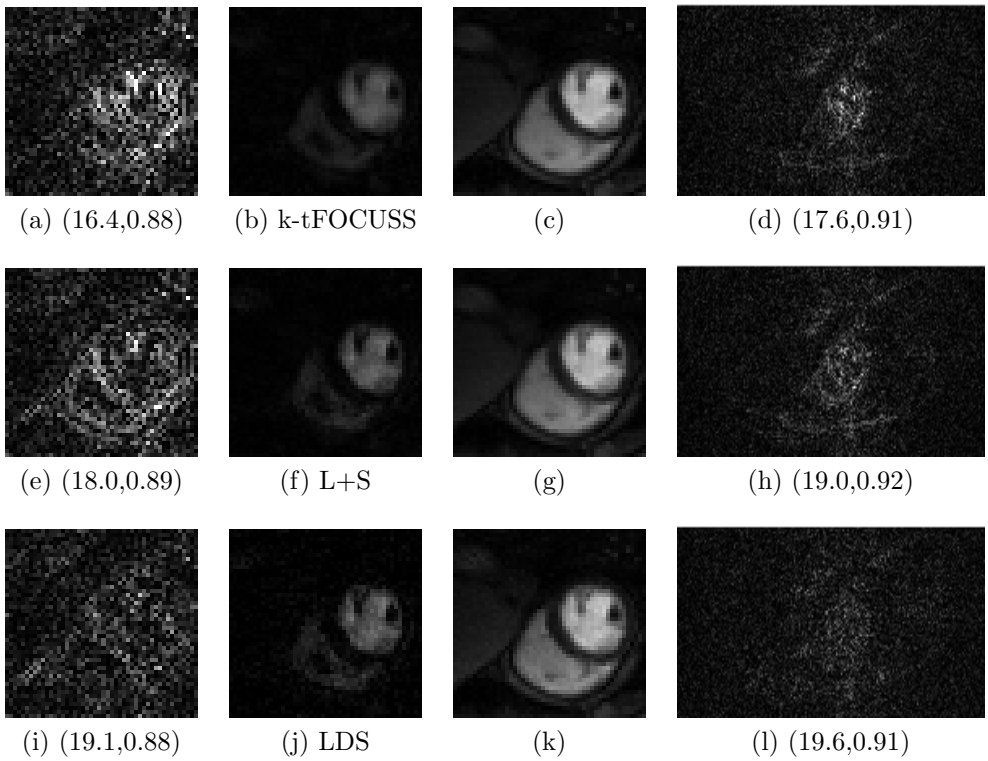

(a) (16.4,0.88) (b) k-tFOCUSS (c) (d) (17.6,0.91)

(e) (18.0,0.89) (f) L+S (g) (h) (19.0,0.92)

(i) (19.1,0.88) (j) LDS (k) (l) (19.6,0.91)

Figure 5.10: Comparison of image recovery using five different spatio-temporal fast dynamic MRI techniques at an acceleration of $R = 4$ (2 of 2). Each row shows results for a technique which is mentioned in the second column. **First col.**: Zoomed-in error images for time-point #17, **Second col.**: Zoomed-in innovation signal, **Third col.**: Zoomed-in recovered images for time-point #18 and, **Fourth col.**: Error images for time-point #18. Image recovery performance metrics are mentioned as (SNR (dB), SSIM) pairs below the error images.

(L+S) [102] and, 5) the proposed LDS technique. For all techniques, the reference data is under-sampled retrospectively using the radial scheme. For the k-t FOCUS, (L+S) and, LDS technique a sliding window of eight samples is used. For the KF and LDS technique the initial states are reconstructed from the union of k-space data from first four time-points. Similar to previous experiments, results are presented for the time-points #17 and #18. The error images are threshold-ed at 10% of maximum image intensity.

Figures 5.9a-5.9d show the results for the KF technique. As stated earlier, the KF technique assumes the innovations to be Gaussian distributed. With this it is assumed that the physiological functions produce some extremely large variations between consecutive time-points which is unrealistic. This assumption can result in signal spike errors as seen in figs 5.9c & 5.9d where isolated white voxels appear in the ventricle.

Figures 5.9e-5.9h show the results for the k-t Sparse technique. In the k-t Sparse technique use of additional sparsity constraint in the temporal Fourier dimension improves upon the recovery using spatial-sparsity alone. The results for spatial-sparsity-only (WAV) were presented in fig. 5.4. A one-to-one comparison cannot be made between the error images of figs 5.4l and 5.9h as they come from different time-points and also the under-sampling is different. However, in the k-t Sparse errors the aliasing artifacts are reduced compared to the errors in the WAV technique.

Figures 5.10a-5.10d show the results for the k-t FOCUSS technique and figs 5.10i-5.10l show those for the LDS technique. These two techniques

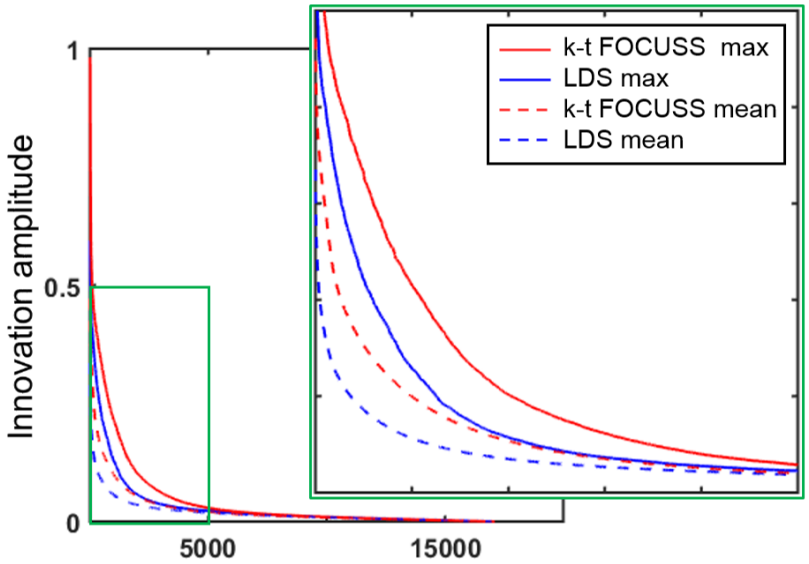

Figure 5.11: Comparison of compressibility of system innovations between the LDS technique (blue) and the k-t FOCUSS technique (red) in the myocardial perfusion data. The rate-of-decay of pixel values is used as a measure of image compressibility. Solid-line: least compressible time-point, dashed-line: mean of rate-of-decay curves over all time-points.

are comparable, in the sense that in both the techniques, for each time-point k a sparse difference image is recovered. In k-t FOCUSS technique this difference image is with respect to a temporally averaged image whereas in the LDS technique its with respect to the image recovered at time-point $k-1$. Thus, the difference image is expected to be relatively more compressible for the LDS technique as compared to that for the k-t FOCUSS technique. Figure 5.11 plots the rate of decay curves for difference images of the myocardial data set for the LDS (blue) and the k-t FOCUSS (red) techniques. Two rate of decay curves are plotted for each technique: solid-line for the least sparse time-point and, dashed-line for the mean of rate-of-decay curves for all time-points. Clearly, the difference images for the LDS technique are more compressible than those for the k-t FOCUSS technique. This improved compressibility of difference image is reflected in the improved signal recovery for the LDS technique over that of the k-t FOCUSS technique. In general, for the selected time-points the order among the four techniques for increasing recovery performance is: KF, k-t Sparse, k-t FOCUSS and LDS.

Figures 5.10e-5.10h show the results for the low-rank plus sparse (L+S) recovery technique. At the selected acceleration of R= 4 the proposed LDS method performs marginally better than the (L+S) technique. For the results shown more pronounced errors are seen for the (L+S) technique in figs. 5.10e and 5.10h.

To quantify the statistical relevance of the results presented in figs. 5.9 and 5.10, figure 5.12 plots the mean signal-to-noise (in dB) versus acceleration

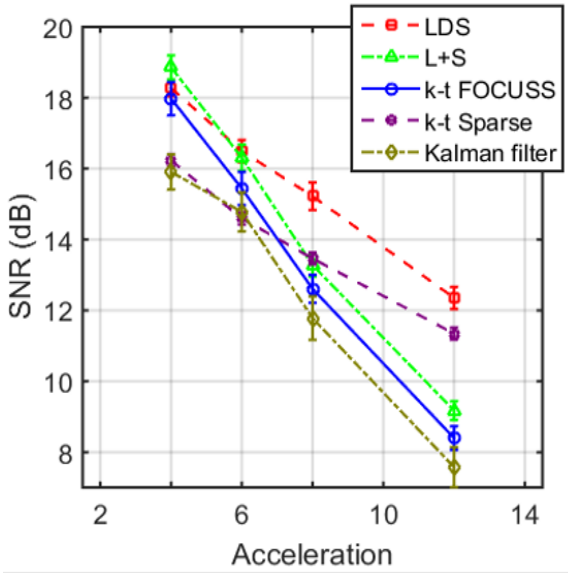

Figure 5.12: ($\mu \pm \sigma$) SNR (in dB) versus acceleration (R) curve for the five different spatio-temporal fast MRI techniques on the in-vivo myocardial perfusion data set.

curves for the five techniques over the complete myocardial perfusion data set. Error bars reflect the standard deviation of the observed values. The proposed LDS technique outperforms the other four techniques at all accelerations except the (L+S) technique at low-acceleration. This can be attributed to the high-density of k-space in the central regions.

5.3.2 Cardiac CINE Imaging

This section presents image recovery results using the proposed fast MRI technique on an in-vivo cardiac cine data set (complex raw data) [66]. The cine data was acquired from 1.5T Philips scanner with a k-t measurement size of 256x256x25 . The field of view (FOV) was 345mm x 270mm and the

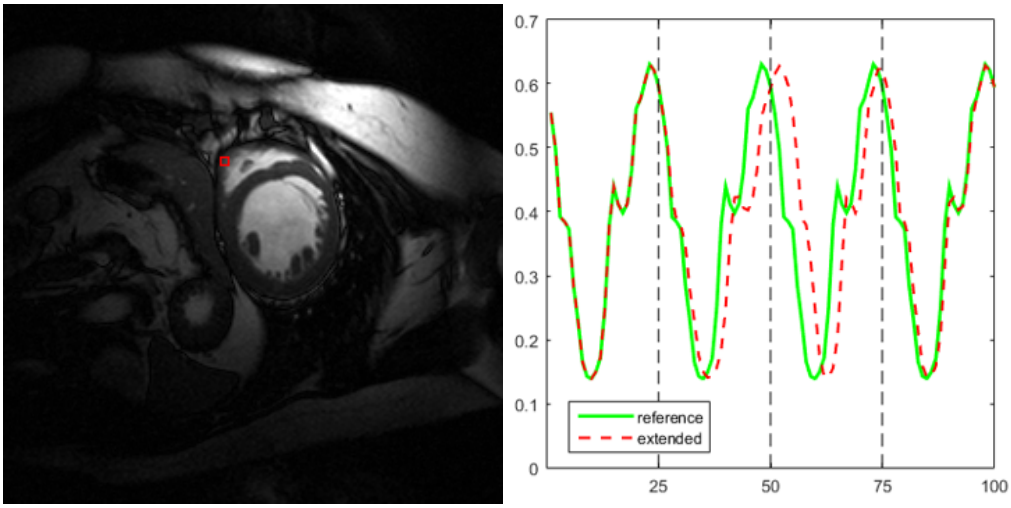

(a) (b)

Figure 5.13: Cardiac CINE data set. (a) A sample time-frame from the data set (b) A voxel (shown in red in (a)) time-series from the modified data set where green-solid represents the original time-series and red-dashed represents the modified pseudo-periodic data.

slice thickness was 10 mm. The acquisition sequence was steady-state free precession (SSFP) with a flip angle of 50 degree and TR= 3.45 msec. The heart frequency was 66 bpm and the retrospective cardiac gating was used.

To demonstrate the generalizability of the proposed linear dynamical system model based fMRI technique image recovery results are presented for few different evolution functions. In order to learn the state-transition matrices $\mathbf{A}_k$'s for the additional evolution functions the original complex data set is modified to yield additional time-points. Specifically, 3D cubic interpolation is used to add 3-cardiac cycles resulting in a total of 100 time-frames. Figure 5.13a shows a sample image from the original data set. A time-series from the modified data is shown in fig. 5.13b for the voxel marked in red in fig. 5.13a.

In addition, to the time-series from modified data set the original time-series (replicated 4 times) is also shown. The modified data adds a slow, fast and faster phases.

5.3.2.1 Evolution Functions and Innovation Sparsity

For cardiac CINE data set, three evolution functions are evaluated for the proposed linear dynamical system model based fast MRI formulation. The three evolution functions are:

- **Temporal difference**: Assumes that the changes between consecutive time-samples are sparse in the spatial space, i.e., $\mathbf{A}_k$'s are identity matrices.

- **Temporal AR2**: Assumes that each voxel is independent of all other voxels and its time-series is periodic can be modeled using a second-order auto-regressive model, i.e., $x_k = \mathbf{A}_1 x_{k-1} + \mathbf{A}_2 x_{k-2}$, where A_1 and A_2 are diagonal matrices.

- **Spatio-temporal AR2**: Assumes that each nxn voxel neighborhood is coupled and can be modeled using an AR2 model with no assumption on the underlying structure of $\mathbf{A}$ matrices. In this chapter, all results are presented for n=3.

To learn the matrices $\mathbf{A}_{1,2}$'s for the temporal AR2 and spatio-temporal AR2 functions, first 50 samples from the modified data set were chosen as

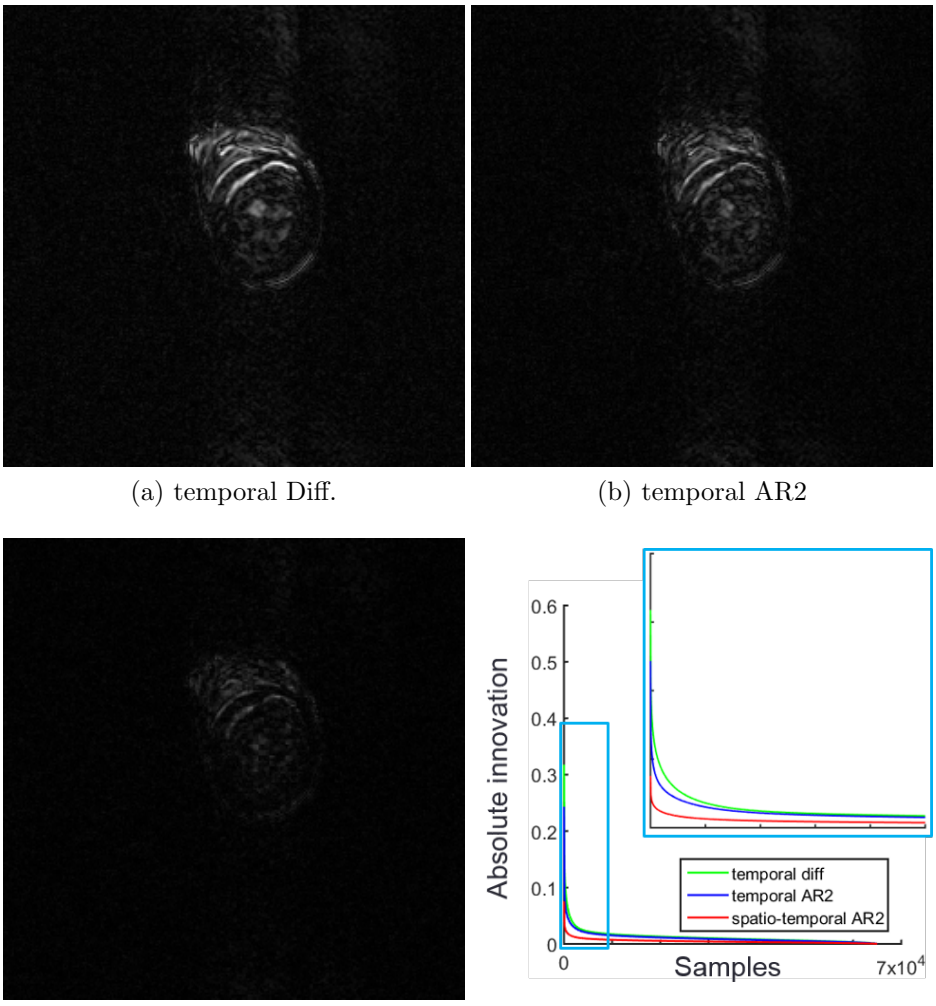

(a) temporal Diff. (b) temporal AR2

(c) spatio-temporal AR2 (d) Innovation sparsity

Figure 5.14: Comparison of compressibility of system innovations for various time-evolution functions for the cardiac CINE data set.

the training samples and a least-squares estimation algorithm was used [115]. Based on the estimated matrices true innovation signals are calculated for the two AR2 evolution functions. Figure 5.14 shows the innovation signals for the three evolution functions and a comparison of their compressibility using the power-law decay curves. In fig. 5.14d decay curves are plotted for signals close to mean compressibility over the complete data set. The spatio-temporal AR2 results in highest mean-compressibility of innovation signal followed by temporal AR2 and then temporal difference evolution function. This order of mean compressibility can be also be observed in the innovation images shown for time-point #55.

Figure 5.15 plots the (mean $\pm$ std. deviation) SNR versus acceleration curves for the image recovery performance on the last 50 test samples of the cardiac data set using the three evolution schemes. In these experiments the initial state estimates are obtained from the true data set. Results are presented for the oracle based initialization, as for sliding window based initial state estimates, the currently used non-linear conjugate gradient descent algorithm with backtracking line-search algorithm shows error-propagation for the spatio-temporal AR2 evolution function. A new algorithm capable of handling sliding window based initial estimates for spatio-temporal AR2 evolution function will be developed as future work. As expected the recovery performance degrades in the following order: spatio-temporal AR2, temporal AR2 and temporal difference.

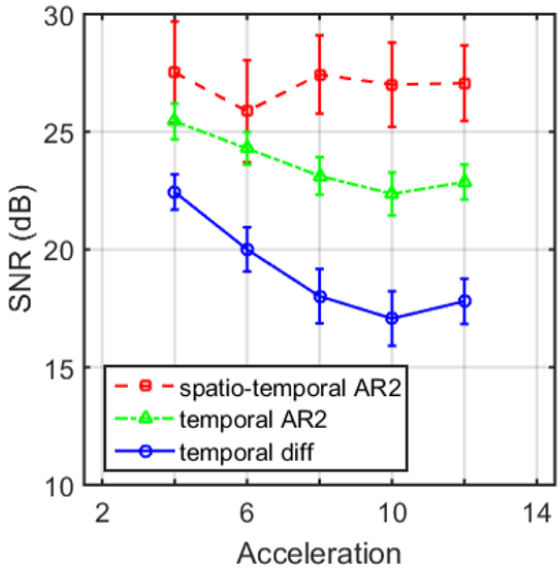

Figure 5.15: Characterization of recovery performance for different evolution-functions based LDS method on the cardiac CINE data set. Oracle initialization are used.

5.3.2.2 Comparison with Spatio-Temporal Techniques

Similar to results presented in section 5.3.1.4, the recovery performance for the temporal AR2 and temporal difference evolution functions is compared with previous spatio-temporal techniques. In these experiments, for the LDS based recovery methods, initial estimates are obtained using the sliding window recovery technique. Based on results from sec. 5.3.1.4, the low-rank plus sparse matrix (L+S) completion and k-t FOCUSS technique are chosen for comparison as they performed the best for the in-vivo data set. Figures 5.16a plots the (mean $\pm$ std. deviation) SNR versus acceleration for the four techniques on the last 50 test samples of the modified data set. Similarly, fig. 5.16b plots the (mean $\pm$ std. deviation) SSIM versus acceleration curves. The

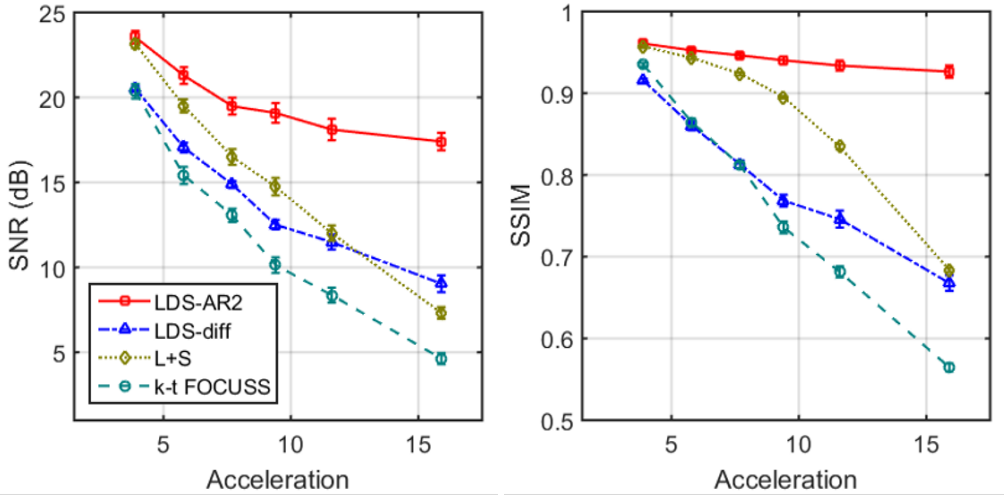

(a) SNR vs. R

(b) SSIM vs. R

Figure 5.16: Image recovery performance characterization for various spatio-temporal fast MRI techniques on the cardiac CINE data set. (mean ± std. deviation) over the complete data set are plotted.

(L+S) technique uses temporal-Fourier transform to sparsify the signal in the S matrix. For this data set the (L+S) technique outperforms the temporal-difference based LDS technique as the sparse decomposition captures the periodic cardiac motion well. However, the proposed LDS method with temporal AR2 outperforms all other techniques at all acceleration factors.

5.4 Conclusions

This chapter presents a novel dynamic MR imaging model which combines the linear dynamic system formulation and sparse representations. Specifically, the proposed model assumes a prior knowledge of a time-evolution model for the underlying physiological imaging function and enforces the model er-

rors (innovations) to be sparse. Further, the dynamic imaging problem is rearranged as the tractable basis pursuit denoising problem. Preliminary results for dynamic MRI recovery experiments on in-vivo myocardial perfusion and cardiac CINE data sets are better than the previously established fast dynamic MRI methods based on variable density k-space sampling.

Chapter 6

Conclusions

This thesis focuses on implementing sparse recovery methods and modifications to the underlying MR signal encoding formulations to achieve high speed MRI . Throughout the thesis I have presented results on dynamic MR applications where there is an imminent need to improve the imaging speeds. Below is a summary of my contributions.

In my first contribution I proposed a modification of the MR signal encoding formulation for compressed sensing MRI methods. The novel signal encoding formulation modulated the spatial magnetization prior to acquisitions using SPAMM tagging radio-frequency pulses. Improvements of $\sim$3dB are observed for the tagging based signal encoding over that of the variable density 2D under-sampling scheme on a T2-weighted brain data set for the total variation norm sparsity prior. Further I combined this formulation with an image-details redundancy encoding scheme. A dictionary learned for sparse representation of image-patches was used to encode the redundancy in high frequency details. The combined sparse recovery method yielded a boost of $\sim$5dB over that of the seminal CS MRI technique based on Wavelet sparsity and variable density 2D under-sampling.

In my second contribution I proposed using dual echo spiral variants for high resolution functional magnetic resonance imaging of human superior colliculus (SC). High resolution imaging of SC is limited by low SNR and low functional CNR. Spiral trajectories are fast due to their efficient use of gradient systems. Therefore acquiring two echoes using fast spiral trajectories reduces noise in high resolution imaging. Dual echo variants: in-in, in-out and out-out were evaluated. All sequences were compared relative to a single-echo spiral-out as the reference trajectory. In SC, the dual-echo out-out outperformed the reference trajectory by 55% in CNR, while other trajectories had performance similar to the reference. The sequences were also compared in early visual cortex. Here, both dual-echo spiral out-out and in-out outperformed the reference by $\sim$25%. Thus, dual-echo spiral variants offer improved CNR performance for high-resolution imaging for both SC and cortex.

In my third contribution I proposed a linear dynamical system based fast dynamic MRI formulation. The new formulation combined the spatio-temporal evolution models for physiological functions with sparse recovery techniques. Specifically, the evolution model errors were assumed to be sparse and recovered from under-sampled data. The evolution model allowed for inherent coupling of spatio-temporal redundancies in the dynamic MR function resulting in higher compressibility of the innovation signal as opposed to spatial- or temporal-only redundancy methods. The proposed formulation resulted in performance improvement of $>\sim$2dB in SNR over that of a temporal data sharing method HYPR on a dynamic myocardial data set.

Future Work

Tuning of acquisition sequences: In my second contribution I tuned sequence trajectories to find the optimal echo time at which the sequence yielded the maximum functional CNR. The tuning process involved fitting of parabola curves to empirical function CNR values for various echo times on a single subject. This tuning process is time consuming, subject dependent, trajectory specific and expensive. A theoretical model for functional CNR based on individual contrast and noise models will allow us to use any sequence at its peak functional sensitivity. Consequently, this should lead to optimal use of sequences across different functional imaging applications.

Adaption of time-evolution model: In my third contribution I have assumed that a prior known spatio-temporal time evolution model is available for the underlying physiological process being imaged. In reality, the physiological functions slowly vary over time and adapting the evolution model to the changes will ensure a high compressibility of system innovations. Thus, a suggestion to allow the evolution model to vary with time and update the model at every iteration.

Bibliography

[1] M. Aharon, M. Elad, and A. Bruckstein. K-SVD: An Algorithm for Designing Overcomplete Dictionaries for Sparse Representation. *Signal Processing, IEEE Transactions on*, 54(11):4311–4322, 2006.

[2] Anthony H. Aletras, Shujun Ding, Robert S. Balaban, and Han Wen. DENSE: displacement encoding with stimulated echoes in cardiac functional MRI. *Journal of magnetic resonance (San Diego, Calif. : 1997)*, 137(1):247–252, March 1999. PMID: 10053155 PMCID: PMC2887318.

[3] D. Angelosante, S.I. Roumeliotis, and G.B. Giannakis. Lasso-Kalman smoother for tracking sparse signals. In *2009 Conference Record of the Forty-Third Asilomar Conference on Signals, Systems and Computers*, pages 181–185, November 2009.

[4] L. Axel and L. Dougherty. MR imaging of motion with spatial modulation of magnetization. *Radiology*, 171(3):841–845, June 1989. PMID: 2717762.

[5] Emmanuel L Barbier, Laurent Lamalle, and Michel Dcorps. Methodology of brain perfusion imaging. *Journal of Magnetic Resonance Imaging*, 13(4):496–520, April 2001.

[6] Andrew V Barger, Walter F Block, Yuriy Toropov, Thomas M Grist, and Charles A Mistretta. Time-resolved contrast-enhanced imaging with isotropic resolution and broad coverage using an undersampled 3d projection trajectory. *Magnetic resonance in medicine*, 48(2):297–305, 2002.

[7] S. Becker, J. Bobin, and E. J. Cands. NESTA: a fast and accurate first-order method for sparse recovery. *SIAM Journal on Imaging Sciences*, 4(1):139, 2011.

[8] Matt A Bernstein, Kevin F King, and Xiaohong Joe Zhou. *Handbook of MRI pulse sequences*. Elsevier, 2004.

[9] Martin Blaimer, Felix Breuer, Matthias Mueller, Robin M Heidemann, Mark A Griswold, and Peter M Jakob. SMASH, SENSE, PILS, GRAPPA: how to choose the optimal method. *Topics in magnetic resonance imaging: TMRI*, 15(4):223–236, August 2004.

[10] Kai Tobias Block and Jens Frahm. Spiral imaging: A critical appraisal. *Journal of Magnetic Resonance Imaging*, 21(6):657–668, 2005.

[11] Bradley D. Bolster, Elliot R. McVeigh, and Elias A. Zerhouni. Myocardial tagging in polar coordinates with use of striped tags1. *Radiology*, 177(3):769–772, December 1990. PMID: 2243987 PMCID: PMC1995227.

[12] David H Brainard. The psychophysics toolbox. *Spatial vision*, 10:433–436, 1997.

[13] Peter Brnert, Bernd Aldefeld, and Holger Eggers. Reversed spiral MR imaging. *Magnetic Resonance in Medicine*, 44(3):479–484, September 2000.

[14] Richard B Buxton. *Introduction to functional magnetic resonance imaging: principles and techniques*. Cambridge university press, 2009.

[15] E.J. Candes, J. Romberg, and T. Tao. Robust uncertainty principles: exact signal reconstruction from highly incomplete frequency information. *Information Theory, IEEE Transactions on*, 52(2):489 – 509, February 2006.

[16] Emmanuel Candes and Justin Romberg. Sparsity and incoherence in compressive sampling. *Inverse Problems*, 23(3):969, 2007.

[17] Emmanuel J. Candes. The restricted isometry property and its implications for compressed sensing. *Comptes Rendus Mathematique*, 346(910):589–592, May 2008.

[18] Emmanuel J Candes and Terence Tao. Decoding by linear programming. *Information Theory, IEEE Transactions on*, 51(12):4203–4215, 2005.

[19] Emmanuel J. Cands, Justin K. Romberg, and Terence Tao. Stable signal recovery from incomplete and inaccurate measurements. *Communications on Pure and Applied Mathematics*, 59(8):1207–1223, 2006.

[20] Scott Shaobing Chen, David L. Donoho, and Michael A. Saunders. Atomic decomposition by basis pursuit. *SIAM JOURNAL ON SCIENTIFIC COMPUTING*, 20:33–61, 1998.

[21] Y. Chen, X. Ye, and F. Huang. A novel method and fast algorithm for MR image reconstruction with significantly under-sampled data. *Inverse Problems and Imaging*, 4(2):223 – 240, jan. 2010.

[22] Kang Cheng, R.Allen Waggoner, and Keiji Tanaka. Human ocular dominance columns as revealed by high-field functional magnetic resonance imaging. *Neuron*, 32(2):359 – 374, 2001.

[23] Blaine A Chronik and Brian K Rutt. A comparison between human magnetostimulation thresholds in whole-body and head/neck gradient coils. *Magnetic resonance in medicine*, 46(2):386–394, 2001.

[24] Anders M. Dale, Bruce Fischl, and Martin I. Sereno. Cortical surface-based analysis: I. segmentation and surface reconstruction. *NeuroImage*, 9(2):179 – 194, 1999.

[25] Bndicte M.A. Delattre, Robin M. Heidemann, Lindsey A. Crowe, Jean-Paul Valle, and Jean-Nol Hyacinthe. Spiral demystified. *Magnetic Resonance Imaging*, 28(6):862–881, July 2010.

[26] Anagha Deshmane, Vikas Gulani, Mark A Griswold, and Nicole Seiberlich. Parallel mr imaging. *Journal of Magnetic Resonance Imaging*, 36(1):55–72, 2012.

[27] Kevin DeSimone, Joseph D Viviano, and Keith A Schneider. Population receptive field estimation reveals new retinotopic maps in human subcortex. *The Journal of Neuroscience*, 35(27):9836–9847, 2015.

[28] D. L. Donoho and X. Huo. Uncertainty Principles and Ideal Atomic Decomposition. *IEEE Trans. Inf. Theor.*, 47(7):2845–2862, September 2006.

[29] David L Donoho. For most large underdetermined systems of linear equations the minimal ?1-norm solution is also the sparsest solution. *Communications on pure and applied mathematics*, 59(6):797–829, 2006.

[30] D.L. Donoho. Compressed sensing. *Information Theory, IEEE Transactions on*, 52(4):1289 –1306, April 2006.

[31] D.L. Donoho, M. Elad, and V.N. Temlyakov. Stable recovery of sparse overcomplete representations in the presence of noise. *Information Theory, IEEE Transactions on*, 52(1):6–18, Jan 2006.

[32] Bradley Efron. Bootstrap methods: another look at the jackknife. *The annals of Statistics*, pages 1–26, 1979.

[33] Bradley Efron and B Efron. *The jackknife, the bootstrap and other resampling plans*, volume 38. SIAM, 1982.

[34] Bradley Efron and Robert J Tibshirani. *An introduction to the bootstrap*. CRC press, 1994.

[35] L. El Ghaoui and G. Calafiore. Robust filtering for discrete-time systems with bounded noise and parametric uncertainty. *Automatic Control, IEEE Transactions on*, 46(7):1084–1089, Jul 2001.

[36] K. Engan, S.O. Aase, and J. Hakon Husoy. Method of optimal directions for frame design. In *Acoustics, Speech, and Signal Processing, 1999. Proceedings., 1999 IEEE International Conference on*, volume 5, pages 2443–2446 vol.5, 1999.

[37] David A Feinberg, Steen Moeller, Stephen M Smith, Edward Auerbach, Sudhir Ramanna, Matthias Gunther, Matt F Glasser, Karla L Miller, Kamil Ugurbil, and Essa Yacoub. Multiplexed echo planar imaging for sub-second whole brain fmri and fast diffusion imaging. *PloS one*, 5(12):e15710, 2010.

[38] David A. Feinberg and Essa Yacoub. The rapid development of high speed, resolution and precision in fMRI. *NeuroImage*, 62(2):720–725, August 2012.

[39] Xue Feng, Michael Salerno, Christopher M. Kramer, and Craig H. Meyer. Kalman filter techniques for accelerated Cartesian dynamic cardiac imaging. *Magnetic Resonance in Medicine*, 69(5):1346–1356, May 2013.

[40] S E Fischer, G C McKinnon, S E Maier, and P Boesiger. Improved myocardial tagging contrast. *Magnetic resonance in medicine: official journal of the Society of Magnetic Resonance in Medicine / Society of*

Magnetic Resonance in Medicine, 30(2):191–200, August 1993. PMID: 8366800.

[41] Urs Gamper, Peter Boesiger, and Sebastian Kozerke. Compressed sensing in dynamic MRI. *Magnetic Resonance in Medicine*, 59(2):365–373, February 2008.

[42] L. Ge, A. Kino, M. Griswold, C.A. Mistretta, J.C. Carr, and D. Li. Myocardial perfusion MRI with sliding-window conjugate-gradient HYPR. *Magnetic Resonance in Medicine*, 62(4):835–839, 2009.

[43] J.C. Geromel. Optimal linear filtering under parameter uncertainty. *Trans. Sig. Proc.*, 47(1):168–175, January 1999.

[44] Gary H. Glover. Simple analytic spiral k-space algorithm. *Magnetic Resonance in Medicine*, 42(2):412–415, 1999.

[45] Gary H. Glover. Spiral imaging in fMRI. *NeuroImage*, 62(2):706–712, August 2012.

[46] Gary H. Glover and Song Lai. Self-navigated spiral fMRI: Interleaved versus single-shot. *Magnetic Resonance in Medicine*, 39(3):361–368, 1998.

[47] Gary H. Glover and Christine S. Law. Spiral-in/out BOLD fMRI for increased SNR and reduced susceptibility artifacts. *Magnetic Resonance in Medicine*, 46(3):515–522, September 2001.

[48] Gary H. Glover and Moriah E. Thomason. Improved combination of spiral-in/out images for BOLD fMRI. *Magnetic Resonance in Medicine*, 51(4):863–868, 2004.

[49] GH Glover and JM Pauly. Projection reconstruction techniques for reduction of motion effects in mri. *Magnetic Resonance in Medicine*, 28(2):275–289, 1992.

[50] B.V. Gowreesunker and A.H. Tewfik. Learning Sparse Representation Using Iterative Subspace Identification. *Signal Processing, IEEE Transactions on*, 58(6):3055 –3065, june 2010.

[51] Clint A Greene, Serge O Dumoulin, Ben M Harvey, and David Ress. Measurement of population receptive fields in human early visual cortex using back-projection tomography. *Journal of vision*, 14(1):17, 2014.

[52] A. Greiser and M.V. Kienlin. Efficient k-space sampling by density-weighted phase-encoding. *Magnetic Resonance in Medicine*, 50(6):1266–1275, 2003.

[53] Mark A Griswold, Peter M Jakob, Robin M Heidemann, Mathias Nittka, Vladimir Jellus, Jianmin Wang, Berthold Kiefer, and Axel Haase. Generalized autocalibrating partially parallel acquisitions (GRAPPA). *Magnetic Resonance in Medicine*, 47(6):1202–1210, June 2002.

[54] Mark A. Griswold, Peter M. Jakob, Mathias Nittka, James W. Goldfarb, and Axel Haase. Partially parallel imaging with localized sensitivities

(PILS). *Magnetic Resonance in Medicine*, 44(4):602–609, October 2000.

[55] J.P. Haldar, D. Hernando, and Zhi-Pei Liang. Compressed-sensing MRI with random encoding. *Medical Imaging, IEEE Transactions on*, 30(4):893 –903, Apr 2011.

[56] Simon Haykin. *Kalman Filters*, pages 1–21. John Wiley & Sons, Inc., 2002.

[57] R D Hoge, R K Kwan, and G B Pike. Density compensation functions for spiral MRI. *Magnetic resonance in medicine: official journal of the Society of Magnetic Resonance in Medicine / Society of Magnetic Resonance in Medicine*, 38(1):117–128, July 1997.

[58] X. Hu and T. Parrish. Reduction of field of view for dynamic imaging. *Magnetic Resonance in Medicine*, 31(6):691–694, June 1994.

[59] Xiaoping Hu and Todd Parrish. Reduction of field of view for dynamic imaging. *Magnetic Resonance in Medicine*, 31(6):691–694, 1994.

[60] E. Ibrahim. Myocardial tagging by Cardiovascular Magnetic Resonance: evolution of techniquespulse sequences, analysis algorithms, and applications. *Journal of Cardiovascular Magnetic Resonance*, 13(1):1–40, 2011.

[61] P Irarrazabal, C H Meyer, D G Nishimura, and A Macovski. Inhomogeneity correction using an estimated linear field map. *Magnetic resonance in medicine: official journal of the Society of Magnetic Resonance*

in Medicine / Society of Magnetic Resonance in Medicine, 35(2):278–282, February 1996.

[62] John Jackson, Craig H Meyer, Dwight G Nishimura, Albert Macovski, et al. Selection of a convolution function for fourier inversion using gridding [computerised tomography application]. *Medical Imaging, IEEE Transactions on*, 10(3):473–478, 1991.

[63] Peter Jakob, Mark Grisowld, Robert Edelman, and Daniel Sodickson. AUTO-SMASH: A self-calibrating technique for SMASH imaging. *Magnetic Resonance Materials in Physics, Biology and Medicine*, 7(1):42–54, 1998.

[64] M. Jerosch-Herold, O. Muehling, and N. Wilke. MRI of Myocardial Perfusion. *Seminars in Ultrasound, CT, and MRI*, 27(1):2 – 10, 2006.

[65] M. Jerosch-Herold, R.T. Seethamraju, C.M. Swingen, N.M. Wilke, and A.E. Stillman. Analysis of myocardial perfusion MRI. *Journal of Magnetic Resonance Imaging*, 19(6):758–770, 2004.

[66] H. Jung, K. Sung, K.S. Nayak, E.Y. Kim, and J.C. Ye. k-t FOCUSS: A general compressed sensing framework for high resolution dynamic MRI. *Magnetic Resonance in Medicine*, 61(1):103–116, 2009.

[67] H. Jung, J.C. Ye, and E.Y. Kim. Improved k-t blast and k-t sense using focuss. *Phys Med Biol*, 52:3201–3226, 2007.

[68] Rudolph Emil Kalman. A new approach to linear filtering and prediction problems. *Journal of Fluids Engineering*, 82(1):35–45, 1960.

[69] Sucharit Katyal, Clint A Greene, and David Ress. High-resolution functional magnetic resonance imaging methods for human midbrain. *J. Vis. Exp*, 63:e3746, 2012.

[70] Sucharit Katyal and David Ress. Attentional base response in intermediate layers of human superior colliculus measured using high-resolution fmri. *Journal of Vision*, 13(9):224, 2013.

[71] Sucharit Katyal, Samir Zughni, Clint Greene, and David Ress. Topography of covert visual attention in human superior colliculus. *Journal of Neurophysiology*, 104(6):3074–3083, 2010.

[72] Stephen F Keevil. Spatial localization in nuclear magnetic resonance spectroscopy. *Physics in medicine and biology*, 51(16):R579, 2006.

[73] Rez Khan, Qin Zhang, Shayan Darayan, Sankari Dhandapani, Sucharit Katyal, Clint Greene, Chandra Bajaj, and David Ress. Surface-based analysis methods for high-resolution functional magnetic resonance imaging. *Graphical Models*, 73(6):313 – 322, 2011. Computational Modeling in Imaging Sciences.

[74] K. F. King, T. K. Foo, and C. R. Crawford. Optimized gradient waveforms for spiral scanning. *Magnetic Resonance in Medicine: Official*

Journal of the Society of Magnetic Resonance in Medicine / Society of Magnetic Resonance in Medicine, 34(2):156–160, August 1995.

[75] David A Koff and Harry Shulman. An overview of digital compression of medical images: can we use lossy image compression in radiology? *Canadian association of radiologists journal*, 57(4):211, 2006.

[76] Gunnar Kruger and Gary H. Glover. Physiological noise in oxygenation-sensitive magnetic resonance imaging. *Magnetic Resonance in Medicine*, 46(4):631–637, 2001.

[77] Anil Kumar, Dieter Welti, and Richard R Ernst. Nmr fourier zeugmatography. *Journal of magnetic resonance*, 213(2):495–509, 2011.

[78] Song Lai and Gary H. Glover. Three-dimensional spiral fMRI technique: A comparison with 2d spiral acquisition. *Magnetic Resonance in Medicine*, 39(1):68–78, 1998.

[79] David J Larkman, Joseph V Hajnal, Amy H Herlihy, Glyn A Coutts, Ian R Young, and Gösta Ehnholm. Use of multicoil arrays for separation of signal from multiple slices simultaneously excited. *Journal of Magnetic Resonance Imaging*, 13(2):313–317, 2001.

[80] David J Larkman and Rita G Nunes. Parallel magnetic resonance imaging. *Physics in Medicine and Biology*, 52(7):R15–R55, April 2007.

[81] Paul C Lauterbur et al. Image formation by induced local interactions: examples employing nuclear magnetic resonance. *Nature*, 242(5394):190–191, 1973.

[82] Tie-Qiang Li, Atsushi Takahashi, Yang Wang, Vincent Mathews, and Gary H. Glover. Dual-echo spiral in/in acquisition method for reducing magnetic susceptibility artifacts in blood-oxygen-level-dependent functional magnetic resonance imaging. *Magnetic Resonance in Medicine*, 55(2):325–334, 2006.

[83] Dong Liang, Edward V. R. DiBella, Rong-Rong Chen, and Leslie Ying. k-t ISD: Dynamic cardiac MR imaging using compressed sensing with iterative support detection. *Magnetic Resonance in Medicine*, 68(1):41–53, July 2012.

[84] Z. Liang and P.C. Lauterbur. *Principles of Magnetic Resonance Imaging: A Signal Processing Perspective*. Wiley-IEEE Press, Oct. 1999.

[85] S.G. Lingala, Yue Hu, E. DiBella, and M. Jacob. Accelerated Dynamic MRI Exploiting Sparsity and Low-Rank Structure: k-t SLR. *Medical Imaging, IEEE Transactions on*, 30(5):1042–1054, May 2011.

[86] Stig Ljunggren. A simple graphical representation of fourier-based imaging methods. *Journal of Magnetic Resonance (1969)*, 54(2):338–343, 1983.

[87] M. Lustig, D. Donoho, and J.M. Pauly. Sparse MRI: The application of compressed sensing for rapid MR imaging. *Magnetic Resonance in Medicine*, 58:1182–1195, 2007.

[88] M. Lustig, D.L. Donoho, J.M. Santos, and J.M. Pauly. Compressed Sensing MRI. *Signal Processing Magazine, IEEE*, 25(2):72 –82, March 2008.

[89] Michael Lustig. *Sparse MRI.* ProQuest, 2008.

[90] Michael Lustig, Juan M Santos, David L Donoho, and John M Pauly. kt sparse: High frame rate dynamic mri exploiting spatio-temporal sparsity. In *Proceedings of the 13th Annual Meeting of ISMRM, Seattle*, volume 2420, 2006.

[91] B. Madore, G.H. Glover, and N.J. Pelc. Unaliasing by Fourier-encoding the overlaps using the temporal dimension (UNFOLD), applied to cardiac imaging and fMRI. *Magnetic Resonance in Medicine*, 42(5):813–828, 1999.

[92] G. McGibney, M. R. Smith, S. T. Nichols, and A. Crawley. Quantitative evaluation of several partial fourier reconstruction algorithms used in MRI. *Magnetic Resonance in Medicine*, 30(1):51–59, 1993.

[93] Craig H Meyer, Bob S Hu, Dwight G Nishimura, and Albert Macovski. Fast spiral coronary artery imaging. *Magnetic Resonance in Medicine*, 28(2):202–213, 1992.

[94] C. A. Mistretta, O. Wieben, J. Velikina, W. Block, J. Perry, Y. Wu, K. Johnson, and Y. Wu. Highly constrained backprojection for time-resolved MRI. *Magnetic Resonance in Medicine*, 55(1):30–40, 2006.

[95] C.A. Mistretta. Undersampled radial MR acquisition and highly constrained back projection (HYPR) reconstruction: Potential medical imaging applications in the post-Nyquist era. *Journal of Magnetic Resonance Imaging*, 29(3):501–516, 2009.

[96] Steen Moeller, Essa Yacoub, Cheryl A. Olman, Edward Auerbach, John Strupp, Noam Harel, and Kamil Ugurbil. Multiband multislice GE-EPI at 7 tesla, with 16-fold acceleration using partial parallel imaging with application to high spatial and temporal whole-brain FMRI. *Magnetic resonance in medicine : official journal of the Society of Magnetic Resonance in Medicine / Society of Magnetic Resonance in Medicine*, 63(5):1144–1153, May 2010.

[97] M. Moon, D. Cornfeld, and J. Weinreb. Dynamic Contrast-Enhanced Breast MR Imaging. *Magnetic Resonance Imaging Clinics of North America*, 17(2):351 – 362, 2009.

[98] Oscar Nestares and David J. Heeger. Robust multiresolution alignment of mri brain volumes. *Magnetic Resonance in Medicine*, 43(5):705–715, 2000.

[99] D. Nishimura. *Principles of Magnetic Resonance Imaging*. www.lulu.com, Feb. 2010.

[100] Cheryl A. Olman, Noam Harel, David A. Feinberg, Sheng He, Peng Zhang, Kamil Ugurbil, and Essa Yacoub. Layer-specific fmri reflects different neuronal computations at different depths in human v1. *PLoS ONE*, 7(3):e32536, 03 2012.

[101] N F Osman, S Sampath, E Atalar, and J L Prince. Imaging longitudinal cardiac strain on short-axis images using strain-encoded MRI. *Magnetic resonance in medicine: official journal of the Society of Magnetic Resonance in Medicine / Society of Magnetic Resonance in Medicine*, 46(2):324–334, August 2001. PMID: 11477637.

[102] Ricardo Otazo, Emmanuel Candes, and Daniel K. Sodickson. Low-rank plus sparse matrix decomposition for accelerated dynamic MRI with separation of background and dynamic components. *Magnetic Resonance in Medicine*, pages n/a–n/a, April 2014.

[103] Mohammed Oumsis, Quoc-Cuong Pham, Abdelaziz D. Sdigui, Bruno Neyran, and Isabelle E. Magnin. Modeling and Tracking of the Cardiac Left Ventricular Motion by a State Space Harmonic Model in MRI Sequence. In *Functional Imaging and Modeling of the Heart*, number 2674 in Lecture Notes in Computer Science, pages 184–193. Springer Berlin Heidelberg, jun 2003.

[104] D.C. Peters, F.R. Korosec, G.M. Thomas, W.F. Block, J.E. Holden, K.K. Vigen, and C.A. Mistretta. Undersampled projection reconstruction

applied to MR angiography. *Magnetic Resonance in Medicine*, 43:91–101, 2000.

[105] Alison R Preston, Moriah E Thomason, Kevin N Ochsner, Jeffrey C Cooper, and Gary H Glover. Comparison of spiral-in/out and spiral-out BOLD fMRI at 1.5 and 3 t. *NeuroImage*, 21(1):291–301, January 2004.

[106] Klaas P. Pruessmann. Encoding and reconstruction in parallel MRI. *NMR in Biomedicine*, 19(3):288–299, May 2006.

[107] Klaas P. Pruessmann, Markus Weiger, Markus B. Scheidegger, and Peter Boesiger. Sense: Sensitivity encoding for fast mri. *Magn Reson Med*, 42:952–962, 1999.

[108] G. Puy, J.P. Marques, R. Gruetter, J. Thiran, D. Van De Ville, P. Vandergheynst, and Y. Wiaux. Spread Spectrum Magnetic Resonance Imaging. *Medical Imaging, IEEE Transactions on*, 31(3):586 –598, March 2012.

[109] S. Ravishankar and Y. Bresler. MR image reconstruction from highly undersampled k-space data by dictionary learning. *IEEE Transactions on Medical Imaging*, 30(5):1028–1041, May 2011.

[110] D. Ress, G.H. Glover, J. Liu, and B. Wandell. Laminar profiles of functional activity in the human brain. *NeuroImage*, 34(1):74 – 84, 2007.

[111] David Ress, Gary H. Glover, Junjie Liu, and Brian Wandell. Laminar profiles of functional activity in the human brain. *NeuroImage*, 34(1):74 – 84, 2007.

[112] R. Rubinstein, A.M. Bruckstein, and M. Elad. Dictionaries for Sparse Representation Modeling. *Proceedings of the IEEE*, 98(6):1045–1057, June 2010.

[113] Klaus Scheffler and Jürgen Hennig. Reduced circular field-of-view imaging. *Magnetic Resonance in Medicine*, 40(3):474–480, 1998.

[114] Keith A Schneider and Sabine Kastner. Effects of sustained spatial attention in the human lateral geniculate nucleus and superior colliculus. *The Journal of Neuroscience*, 29(6):1784–1795, 2009.

[115] Tapio Schneider and Arnold Neumaier. Algorithm 808: Arfita matlab package for the estimation of parameters and eigenmodes of multivariate autoregressive models. *ACM Transactions on Mathematical Software (TOMS)*, 27(1):58–65, 2001.

[116] Kang G Shin and Neil D McKay. Minimum-time control of robotic manipulators with geometric path constraints. *Automatic Control, IEEE Transactions on*, 30(6):531–541, 1985.

[117] V. Singh and A.H. Tewfik. Redundancy Encoding in Dynamic MR Imaging using Structured Sparsity. In *MICCAI Wshp. Sparsity Techniques in Medical Imaging*, pages 1–8, 2012.

[118] Uygar Smbl, Juan M. Santos, and John M. Pauly. A Practical Acceleration Algorithm for Real-Time Imaging. *IEEE transactions on medical imaging*, 28(12):2042–2051, December 2009.

[119] D. K. Sodickson and W. J. Manning. Simultaneous acquisition of spatial harmonics (SMASH): fast imaging with radiofrequency coil arrays. *Magnetic resonance in medicine*, 38(4):591–603, October 1997.

[120] U. Sumbul, J.M. Santos, and J.M. Pauly. Improved Time Series Reconstruction for Dynamic Magnetic Resonance Imaging. *IEEE Transactions on Medical Imaging*, 28(7):1093–1104, July 2009.

[121] B Sundermann, D Herr, W Schwindt, and B Pfleiderer. Multivariate classification of blood oxygen level–dependent fmri data with diagnostic intention: A clinical perspective. *American Journal of Neuroradiology*, 35(5):848–855, 2014.

[122] DS Taubman and MW Marcellin. Image compression fundamentals, standards and practice: Jpeg2000, 2002.

[123] C.M. Tsai and D.G. Nishimura. Reduced aliasing artifacts using variable-density k-space sampling trajectories. *Magnetic Resonance in Medicine*, 43:452–458, 2000.

[124] J. Tsao, B. Behnia, and A.G. Webb. Unifying linear prior-information-driven methods for accelerated image acquisition. *Magnetic Resonance in Medicine*, 46(4):652–660, 2001.

[125] J. Tsao, P. Boesiger, and K.P. Pruessmann. k-t BLAST and k-t SENSE: Dynamic MRI with high frame rate exploiting spatio-temporal correlations. *Magnetic Resonance in Medicine*, 50(5):1031–1042, 2003.

[126] Donald B Twieg. The k-trajectory formulation of the nmr imaging process with applications in analysis and synthesis of imaging methods. *Medical Physics*, 10(5):610–621, 1983.

[127] N. Vaswani. Kalman filtered Compressed Sensing. In *15th IEEE International Conference on Image Processing, 2008. ICIP 2008*, pages 893–896, October 2008.

[128] N. Vaswani. LS-CS-Residual (LS-CS): Compressive Sensing on Least Squares Residual. *IEEE Transactions on Signal Processing*, 58(8):4108–4120, August 2010.

[129] E.A. Wan and R. Van Der Merwe. The unscented kalman filter for nonlinear estimation. In *Adaptive Systems for Signal Processing, Communications, and Control Symposium 2000. AS-SPCC. The IEEE 2000*, pages 153–158, 2000.

[130] Hui Wang and A.A. Amini. Cardiac Motion and Deformation Recovery From MRI: A Review. *IEEE Transactions on Medical Imaging*, 31(2):487 –503, February 2012.

[131] Z. Wang, A.C. Bovik, H.R. Sheikh, and E.P. Simoncelli. Image quality

assessment: from error visibility to structural similarity. *Image Processing, IEEE Transactions on*, 13(4):600 –612, april 2004.

[132] Ze Wang, Sandhitsu R. Das, Sharon X. Xie, Steven E. Arnold, John A. Detre, and David A. Wolk. Arterial spin labeled {MRI} in prodromal Alzheimer's disease: A multi-site study . *NeuroImage: Clinical*, 2:630–636, 2013.

[133] N Parker Willis and Yoram Bresler. Lattice-theoretic analysis of time-sequential sampling of spatiotemporal signals. i. *Information Theory, IEEE Transactions on*, 43(1):190–207, 1997.

[134] N Parker Willis and Yoram Bresler. Lattice-theoretic analysis of time-sequential sampling of spatiotemporal signals. i. *Information Theory, IEEE Transactions on*, 43(1):190–207, 1997.

[135] G.A. Wright. Magnetic resonance imaging. *Signal Processing Magazine, IEEE*, 14(1):56 –66, January 1997.

[136] Robert H Wurtz and Joanne E Albano. Visual-motor function of the primate superior colliculus. *Annual review of neuroscience*, 3(1):189–226, 1980.

[137] Guoliang Xu, Qing Pan, and Chandrajit L. Bajaj. Discrete surface modelling using partial differential equations. *Computer Aided Geometric Design*, 23(2):125 – 145, 2006.

[138] Essa Yacoub, Amir Shmuel, Nikos Logothetis, and Kâmil Uğurbil. Robust detection of ocular dominance columns in humans using hahn spin echo bold functional mri at 7 tesla. *Neuroimage*, 37(4):1161–1177, 2007.

[139] M. Yaghoobi, T. Blumensath, and M.E. Davies. Dictionary Learning for Sparse Approximations With the Majorization Method. *Signal Processing, IEEE Transactions on*, 57(6):2178–2191, June 2009.

[140] J.C. Ye, S. Tak, Y. Han, and H.W. Park. Projection reconstruction MR imaging using FOCUSS. *Magnetic Resonance in Medicine*, 57(4):764–775, 2007.

[141] S.G. Yuen, P.M. Novotny, and R.D. Howe. Quasiperiodic predictive filtering for robot-assisted beating heart surgery. In *IEEE International Conference on Robotics and Automation, 2008. ICRA 2008*, pages 3875–3880, may 2008.

[142] Paul A. Yushkevich, Joseph Piven, Heather Cody Hazlett, Rachel Gimpel Smith, Sean Ho, James C. Gee, and Guido Gerig. User-guided 3d active contour segmentation of anatomical structures: Significantly improved efficiency and reliability. *NeuroImage*, 31(3):1116 – 1128, 2006.

[143] Bo Zhao, Justin P Haldar, Cornelius Brinegar, and Zhi-Pei Liang. Low rank matrix recovery for real-time cardiac mri. In *Biomedical Imaging: From Nano to Macro, 2010 IEEE International Symposium on*, pages 996–999. IEEE, 2010.